

e. Copy of one or two specific publications/research papers of the applicant, relevant to the research work on which the award is claimed.

1. S-Adenosylmethionine-responsive cystathionine b-synthase modulates sulfur metabolism and redox balance in *Mycobacterium tuberculosis*. Bandyopadhyay P, Pramanick I, Biswas R, Sabarinath PS, Sreedharan S, Singh S, Rajmani R, Laxman S, Dutta S and **Singh A**. *Sci Adv*. 2022. 8: eabo0097
2. Mishra R, Kohli S, Malhotra N, Bandhyopadhyay P, Mehta M, Munshi M, Adiga V, Ahuja VK, Shandil RK, Rajmani RS, Seshasayee ASN and **Singh A**. Targeting redox heterogeneity to counteract drug tolerance in replicating *Mycobacterium tuberculosis*. *Sci Transl Med*. 2019. 11 (518)

TUBERCULOSIS

Targeting redox heterogeneity to counteract drug tolerance in replicating *Mycobacterium tuberculosis*

Richa Mishra^{1,2}, Sakshi Kohli^{1,2}, Nitish Malhotra³, Parijat Bandyopadhyay^{1,2}, Mansi Mehta^{1,2}, MohamedHusen Munshi^{1,2}, Vasista Adiga², Vijay Kamal Ahuja⁴, Radha K. Shandil⁴, Raju S. Rajmani², Aswin Sai Narain Seshasayee³, Amit Singh^{1*}

The capacity of *Mycobacterium tuberculosis* (*Mtb*) to tolerate multiple antibiotics represents a major problem in tuberculosis (TB) management. Heterogeneity in *Mtb* populations is one of the factors that drives antibiotic tolerance during infection. However, the mechanisms underpinning this variation in bacterial population remain poorly understood. Here, we show that phagosomal acidification alters the redox physiology of *Mtb* to generate a population of replicating bacteria that display drug tolerance during infection. RNA sequencing of this redox-altered population revealed the involvement of iron-sulfur (Fe-S) cluster biogenesis, hydrogen sulfide (H₂S) gas, and drug efflux pumps in antibiotic tolerance. The fraction of the pH- and redox-dependent tolerant population increased when *Mtb* infected macrophages with actively replicating HIV-1, suggesting that redox heterogeneity could contribute to high rates of TB therapy failure during HIV-TB coinfection. Pharmacological inhibition of phagosomal acidification by the antimalarial drug chloroquine (CQ) eradicated drug-tolerant *Mtb*, ameliorated lung pathology, and reduced post-chemotherapeutic relapse in in vivo models. The pharmacological profile of CQ (C_{max} and AUC_{last}) exhibited no major drug-drug interaction when coadministered with first line anti-TB drugs in mice. Our data establish a link between phagosomal pH, redox metabolism, and drug tolerance in replicating *Mtb* and suggest repositioning of CQ to shorten TB therapy and achieve a relapse-free cure.

INTRODUCTION

An unusually long-term (6 months) therapy involving multiple anti-biotics is required to cure tuberculosis (TB) in humans. This protracted treatment is necessary to prevent relapses due to genetically drug-sensitive bacteria that become transiently resistant inside host cells and tissues, a phenomenon called phenotypic drug tolerance. Thus, the mechanistic basis of phenotypic drug tolerance needs to be studied to develop new drugs with treatment-shortening properties. Recent studies indicate that heterogeneity in both the host environment and the bacterial population can promote phenotypic drug tolerance. For example, variability in the activation status of macrophages distinctly modulates drug tolerance in *Mycobacterium tuberculosis* (*Mtb*) (1). Immune activation of macrophages leads to release of antibacterial effectors such as reactive nitrogen species and reactive oxygen species (ROS) (2, 3), leading to a quiescent drug-tolerant state of *Mtb* (4). In support of this theme, drug tolerance is diminished in mice and macrophages deficient in producing nitric oxide (NO) (1). Moreover, extracellular *Mtb* present in the cavity caseum derived from *Mtb*-infected rabbits show slow replication and extreme tolerance to several first- and second-line anti-TB drugs (5). Single-cell measurements have revealed that stress conditions (for example, starvation) in vitro and host immune pressures (interferon- γ , a cytokine critical for anti-TB host immunity) in vivo create phenotypic heterogeneity within the *Mtb* population, which allows for the selection of nongrowing metabolically active bacteria responsible for postchemotherapeutic relapse (4).

However, recent studies suggest that adoption of a nongrowing state is not a prerequisite for drug tolerance (6–10). A fraction of both replicating and nonreplicating bacteria shows regrowth after drug withdrawal (4, 7), emphasizing that growth-arrested bacteria do not solely mediate tolerance. Alternate mechanisms—such as induction of drug efflux pumps, asymmetric cell division, and increased mistranslation rates—can contribute to substantial drug tolerance in actively multiplying cells (6, 8, 9, 11). Induction of efflux pumps is, so far, the only mechanism known to confer drug tolerance in replicating *Mtb* inside macrophages (6). Despite their importance, we lack understanding of macrophage-specific cue(s) and associated changes in the physiology of replicating *Mtb* that drive drug tolerance. Filling this knowledge gap will help in developing strategies to target both bacterial and host determinants crucial for mobilizing a drug-tolerant phenotype in vivo. A detailed summary of our current understanding of phenotypic drug tolerance in *Mtb* is described in fig. S1.

Using a ratiometric fluorescence biosensor (Mrx1-roGFP2) of the major mycobacterial antioxidant mycothiol (MSH), we previously showed that the environment inside macrophages rapidly generates heterogeneity in the MSH redox potential (E_{MSH}) of the *Mtb* population (12). Confocal and flow cytometry measurements categorized infected macrophages into two distinct populations, one predominantly harboring E_{MSH} -reduced bacteria (300 ± 6 mV) and the other predominantly harboring E_{MSH} -basal bacteria (275 ± 5 mV) (12). In addition, a minor fraction of infected macrophages was enriched for *Mtb* in the E_{MSH} -oxidized state (242 ± 6 mV) (12). These results are consistent with the heterogeneous and dynamic nature of both host and pathogen (13–15), suggesting that their interaction is likely to result in bacterial populations with diverse phenotypes. The E_{MSH} -reduced population was found to be refractory to anti-TB drugs compared to other populations (E_{MSH} -oxidized and E_{MSH} -basal) (12). Therefore, understanding the basis of redox

¹Department of Microbiology and Cell Biology, Indian Institute of Science, Bangalore 560012, India. ²Centre for Infectious Disease Research, Indian Institute of Science, Bangalore 560012, India. ³National Centre for Biological Sciences (NCBS), Tata Institute of Fundamental Research (TIFR), Bangalore 560065, India. ⁴Foundation for Neglected Disease Research, Bangalore 560065, India. *Corresponding author. Email: asingh@iisc.ac.in

heterogeneity could inform strategies that result in better targeting of drug-tolerant *Mtb*. In this study, we performed RNA sequencing (RNA-seq) of redox-altered intraphagosomal *Mtb* populations and identified bacterial factors and host cues associated with drug tolerance.

RESULTS

Transcriptional profiling of redox-diverse populations identifies determinants of drug tolerance

We followed our previously developed flow cytometry protocol that averages median fluorescence ratio (405 nm/488 nm) of the Mrx1-roGFP2 biosensor expressed by intraphagosomal *Mtb* to gate macrophages into fractions enriched with either *E* MSH-reduced ($EMSH = 300 \pm 6$ mV) or *EMSH*-basal ($EMSH = 275 \pm 5$ mV) bacteria (fig. S2) (12). Using this gating strategy, we sorted THP-1 macrophages infected with *Mtb*/Mrx1-roGFP2 at 24 hours postinfection (p.i.), treated them with isoniazid [Inh; threefold the in vitro minimal inhibitory concentration (MIC)] for 48 hours, and confirmed that the *EMSH*-reduced fraction is more tolerant to Inh than *EMSH*-basal fraction (fig. S3). As reduced susceptibility to Inh originated from a population of intraphagosomal *Mtb*, our findings align with a recent consensus statement defining tolerance as the general ability of a population to survive longer antibiotic exposure (16). To investigate the physiological basis of the differential tolerance of redox-altered *Mtb*, we performed global transcriptional profiling by RNA-seq of *EMSH*-reduced and *EMSH*-basal populations derived from THP-1 macrophages flow-sorted 24 hours after infection with *Mtb*/Mrx1-roGFP2 (Fig. 1).

We isolated total bacterial RNA, performed RNA-seq, and analyzed data using DESeq2 (Fig. 1A). Control RNA was isolated from logarithmically grown *Mtb* resuspended in complete RPMI for 24 hours (in vitro control). We compared the transcription profiles of macrophage-derived populations to in vitro control and to one another to identify responses that were induced in both populations and responses that were significantly induced in *EMSH*-reduced bacteria [false discovery rate (FDR), 0.05]. Principal components analysis and clustering of heat map plots showed that the three samples clustered by their biological replicates (fig. S4 and tables S1, A to C). As compared to the in vitro control, the expression of 560 and 617 genes was affected in the *EMSH*-reduced and *EMSH*-basal populations, respectively (FDR, 0.05; fold change, 1.5) (table S1, B and C). Of 295 genes showing overlap, 151 were more induced in the drug-tolerant *EMSH*-reduced population (Fig. 1B and table S1D). The transcriptome of both populations considerably overlapped with that of a previously reported transcriptional signature of intraphagosomal *Mtb* ($P < 0.05$, Fisher's exact test; Fig. 1C) (17). Consistent with studies showing phagosomal acidification as the earliest cue that alters the transcriptome of *Mtb* inside unstimulated macrophages (18, 19), RNA-seq data of the *EMSH*-reduced fraction overlapped significantly with the transcriptome of *Mtb* grown in 7H9 broth at pH 5.5 ($P = 1.05 \times 10^{-2}$) and pH 4.5 ($P = 1.5 \times 10^{-15}$) (Fig. 1C) (17, 20). The *EMSH*-basal transcriptome showed little similarity to the genes down-regulated at pH 5.5 (Fig. 1C) (17).

Using *Mtb*/Mrx1-roGFP2 conjugated with pHrodo dye, which emits fluorescence only in acidic pH (21), we infected THP-1 macrophages and confirmed phagosomal pH to be 6.25 ± 0.14 , as previously reported for unstimulated macrophages (fig. S5) (22). Likewise, we examined the pH of flow-sorted macrophages enriched with

EMSH-basal or *EMSH*-reduced bacteria. Macrophages enriched in *EMSH*-reduced bacteria are more acidic ($pH 5.79 \pm 0.2$) than *EMSH*-basal bacteria ($pH 6.67 \pm 0.08$) (fig. S5D), indicating that subtle variations in phagosomal pH underlie heterogeneity in *EMSH* of *Mtb* during infection. We also compared the transcriptional profiles of *EMSH*-altered *Mtb* and a mutant of the redox-sensitive transcription factor WhiB3 (*MtbDwhiB3*), which has been linked to *Mtb*'s transcriptional response to low pH (20). We isolated RNA from wild-type (WT) *Mtb*, *MtbDwhiB3*, and *whiB3*-complement (*whiB3*-Comp) cultured in 7H9 broth at neutral pH (6.6) and acidic pH (4.5) and performed RNA-seq. The WhiB3-specific, low pH-induced gene set showed comparable expression in the *EMSH*-reduced population. In contrast, only a fraction of the WhiB3 regulon coincided with the transcriptome of *EMSH*-basal bacteria, with lesser induction of the regulon than that seen in the case of the *EMSH*-reduced *Mtb* (fig. S6 and table S2D). These findings link the transcriptome of *EMSH*-reduced bacteria with *Mtb*'s response to low pH.

Low pH increases the solubility of transition metals including iron and copper (23), thereby allowing these metals to cross biological membranes and participate in metal-catalyzed ROS generation via the Fenton reaction (24). Consistent with this phenomenon, transcriptional sensors of metal toxicity (*furA*, *csaR*, and *cmtR*), exporters of toxic metals (*ctpV* and *ctpG*), redox sensors (*whiB*s and *sufR*), and antioxidant systems (*rubA/B*, *ahpC*, and *trxB2*) were induced in the *EMSH*-reduced fraction (Fig. 1D and table S3). Because ROS damages DNA, proteins, and lipids, we observed that several genes implicated in DNA repair, protein quality control, and envelope stress were induced in *EMSH*-reduced fraction (Fig. 1D and table S3). A previous study linked the stochastic expression of catalase (*katG*) in mediating Inh tolerance (7). However, *katG* expression was not differentially regulated in the *EMSH*-reduced fraction, indicating that redox-mediated Inh tolerance is unrelated to *katG* expression. Genes coordinating glyoxylate and methyl citrate cycles (*icl1* and *prpD*) and alternate respiration (*cydAB*) were up-regulated in the *EMSH*-reduced fraction (Fig. 1D and table S3); both *icl1* and *cydAB* are vital for mitigating oxidative stress and promoting multidrug tolerance in *Mtb* (25–27). The overlap between acidic pH and oxidative stress responses has been reported in several bacteria (28–30), indicating a link between pH- and oxidative stress-driven adaptations.

A reductive shift in the *EMSH* of *Mtb* indicates an increase in the cytoplasmic pool of reduced MSH. Supporting this, genes associated with the biogenesis of cysteine (CySH), a component of MSH (31), were up-regulated in the *EMSH*-reduced fraction. For example, *lat*, *metA*, and *metC* involved in methionine (Met) biogenesis (32), and *metB* encoding a bifunctional enzyme (cystathionine-γ-lyase/ cystathionine-γ-synthase) that incorporates sulfur from Met to CySH (reverse transsulfuration pathway) (33) were induced in the *EMSH*-reduced fraction (Fig. 1D). The enzyme MetB generates H₂S gas as a by-product (33), which protects several bacterial species from antibiotics and oxidative stress (34–36). We detected that *Mtb* cultured in 7H9 broth at pH 6.2 and pH 4.5 generated more H₂S than at neutral pH (fig. S7), indicating a link between H₂S biogenesis, acid stress, and reductive shift in *EMSH*. CySH also serves as a source of sulfide for the biogenesis of Fe-S clusters, which modulate bacterial response to antibiotics (37). Accordingly, genes involved in Fe-S cluster biogenesis [Rv1460 (*sufR*) and Rv1461 (*sufB*)] (38, 39) were up-regulated in the *EMSH*-reduced fraction (Fig. 1D and table S3). Other transcriptional changes in *EMSH*-reduced cells involving genes that are known to promote drug refractoriness include genes

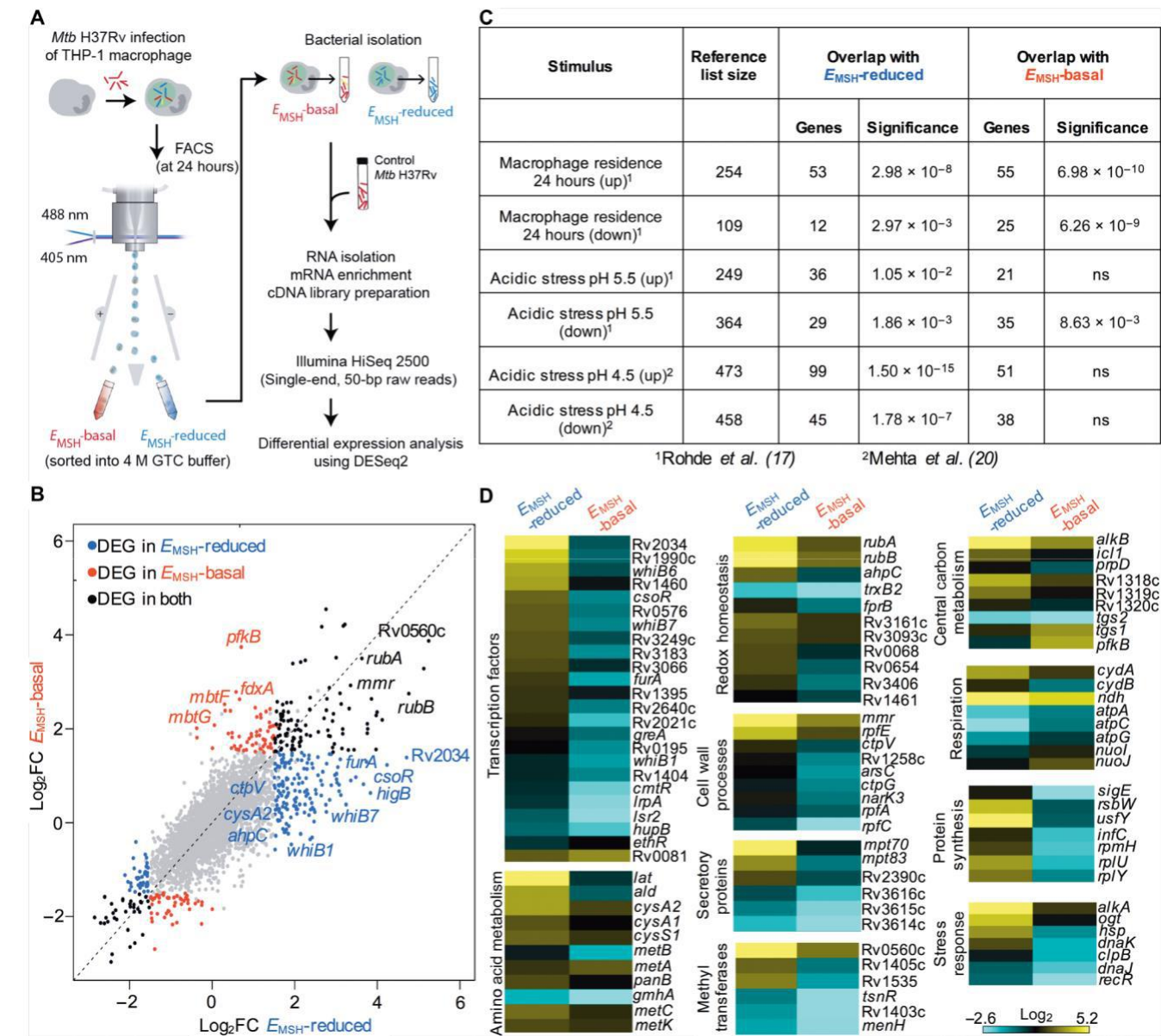


Fig. 1. RNA-seq of intraphagosomal *Mtb* derived from *E_{MSH}*-reduced and *E_{MSH}*-basal fractions. (A) Schematic depiction of flow sorting–coupled RNA-seq of intraphagosomal bacteria present in *E_{MSH}*-basal and *E_{MSH}*-reduced fractions of THP-1 macrophages infected with *Mtb*/Mrx1-roGFP2. *Mtb* cells (optical density at 600 nm, 0.4) harvested and resuspended in RPMI for 24 hours were used as an in vitro control. FACS, fluorescence-activated cell sorting; GTC, guanidinium thiocyanate. (B) Scatter plot indicates relative distribution of differentially expressed genes (DEGs) from the *E_{MSH}*-reduced and *E_{MSH}*-basal fractions on the basis of log₂ fold changes (FC) (blue, DEGs specific to *E_{MSH}*-reduced; red, DEGs unique to *E_{MSH}*-basal; black, DEGs common to both; gray, nonsignificant genes). (C) The table summarizes the transcriptional overlap between this study and the response of *Mtb* under intramacrophage and pH stress conditions. Fisher's exact test with $P < 0.05$ as a cutoff for significance. ns, no significant difference. (D) Heat maps indicate log₂ fold changes of DEGs belonging to various functional categories (obtained from Mycobrowser, École polytechnique fédérale de Lausanne) in *E_{MSH}*-reduced and *E_{MSH}*-basal fractions. Genes were considered differentially expressed on the basis of the false discovery rate (FDR) of 0.05 and absolute fold change of 1.5 (tables S1 and S3).

associated with S-adenosyl methionine (SAM) biosynthesis (*metK*) (32), methyl transferases (*menH*, Rv0560c, Rv1403c, and Rv1405c) (40–42), and drug efflux pumps (*mmr*, Rv1258c, and Rv1250) (6, 43, 44) (Fig. 1D and table S3). In conclusion, the RNA-seq data suggest a major role of host acidification and bacterial mechanisms involved in alleviating metal toxicity, ROS remediation, and re-alignment of sulfur metabolism in the emergence of drug-tolerant *E_{MSH}*-reduced population during infection.

CySH-disposal pathways coordinate redox-mediated drug tolerance in *Mtb*

CySH-dependent pathways such as biogenesis of H₂S, low molecular-weight thiols, and Fe-S clusters protect bacteria against antibiotics and oxidative stress (37, 45). In *Mtb*, supplementation with H₂S donor [sodium hydrosulfide NaHS] restored the imbalance in the *E_{MSH}* of MSH recycling mutants (46), and Fe-S cluster-dependent regulators (for example, WhiB3 and WhiB7) mediate a reductive shift in *E_{MSH}*

of *Mtb* in response to acidic pH and antibiotics (20, 47). On this basis, we reasoned that the induction of *metB* (H₂S biogenesis) and *sufR* (regulator of Fe-S cluster biogenesis) could contribute to the emergence of a drug-tolerant *EMSH*-reduced population (Fig. 2A). To test this idea, we independently disrupted *metB* (*MtbDmetB*) and *sufR* (*MtbDsufR*) in *Mtb* H37Rv (fig. S8, A to E). As expected, *MtbDmetB* displayed a reduced capability to produce H₂S compared to WT *Mtb*

(fig. S8F). Similarly, disruption of *sufR* abrogated the induction of the *suf* operon (Rv1461 to Rv1466) involved in Fe-S cluster biogenesis (fig. S8G). Because *WhiB3* promotes the emergence of *EMSH*-reduced population inside macrophages (20), we used the *MtbDwhiB3* strain as a control. THP-1 macrophages infected with *MtbDmetB* or *MtbDsufR* expressing Mrx1-roGFP2 showed a significant decrease in the reductive-*EMSH* fraction compared to WT *Mtb* ($P < 0.01$)

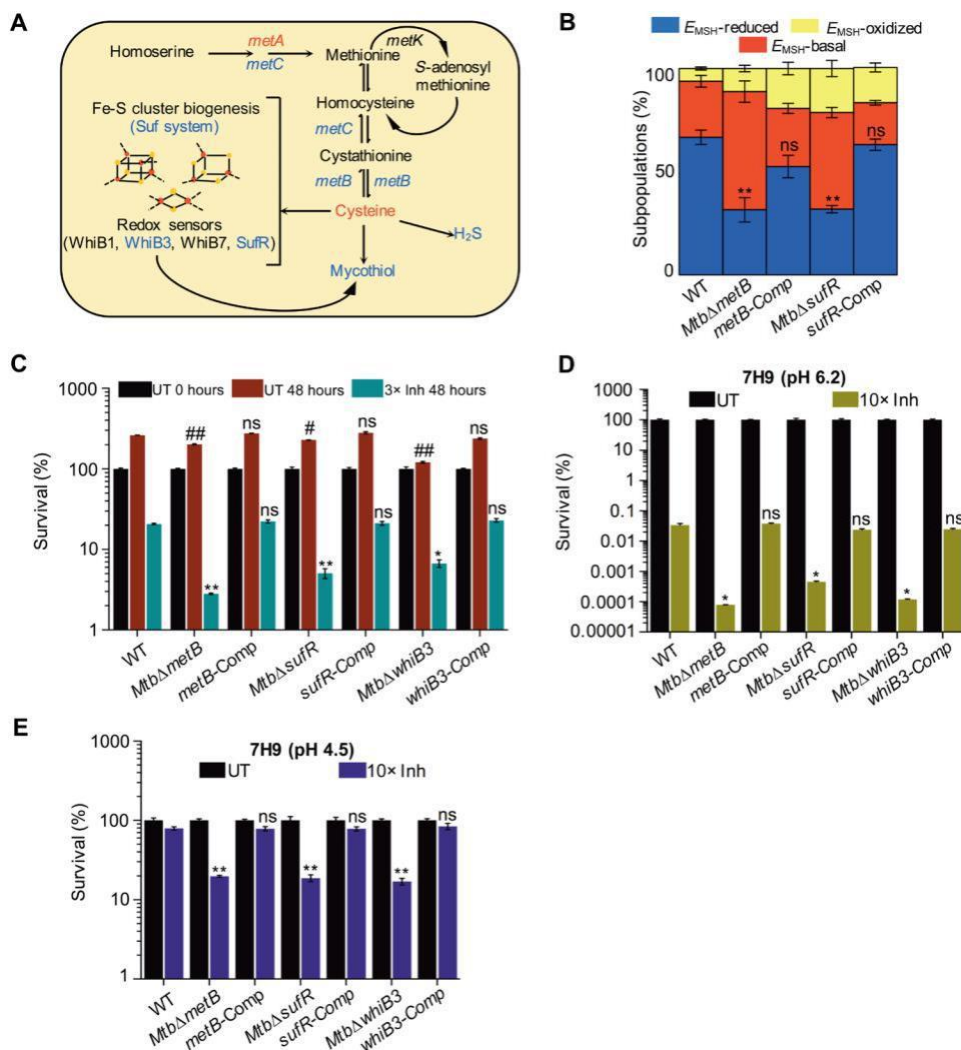


Fig. 2. Cysteine utilization pathways promote redox heterogeneity and drug tolerance in *Mtb*. (A) Various cysteine (CySH) utilization pathways in *Mtb*. Expression of genes (blue) coordinating CySH flux into pathways for mycothiol (MSH), Fe-S cluster, and H₂S biogenesis is induced in the *EMSH*-reduced fraction. (B) THP-1 macrophages were infected for 24 hours with the indicated strains of *Mtb* expressing Mrx1-roGFP2, and the percent distribution of redox-diverse fractions was measured at 24 hours p.i. and depicted as a stacked bar plot. ** $P < 0.01$, by Mann-Whitney test compares *EMSH*-reduced fraction in various strains of *Mtb* with WT *Mtb*. (C) THP-1 macrophages infected for 24 hours with the indicated strains of *Mtb* were exposed for an additional 48 hours to Inh (2.18 mM, 3 of in vitro MIC) or left untreated. Bacillary load was determined by CFU enumeration, and percent survival was quantified by normalizing the CFU in Inh-treated samples at 48 hours against untreated samples (UT) at 0 hours. * $P < 0.05$, ** $P < 0.01$, # $P < 0.05$, and ## $P < 0.01$, by Mann-Whitney test. Number signs (#) and asterisks (*) compare survival between WT *Mtb* and other strains under UT and Inh-treated conditions, respectively. (D and E) Indicated strains of *Mtb* grown in 7H9-tyloxapol broth acidified to pH 6.2 or pH 4.5 were exposed to Inh (7.25 mM, 10 of in vitro MIC) or kept unexposed. Bacterial load was quantified after 5 days of treatment by CFU enumeration, and percent survival was quantified strain-wise by normalizing the bacterial load in Inh-treated samples at day 5 against untreated samples. * $P < 0.05$, ** $P < 0.001$, by Mann-Whitney test. Asterisks compare survival between WT *Mtb* and other strains after 5 days of Inh treatment. Data shown in each panel are the results of three independent experiments performed in triplicate (means \pm SD). ns, no significant difference ($P > 0.05$).

Phagosomal acidification is required for the redox-dependent multidrug tolerance of *Mtb*

To clarify the link between phagosomal pH, redox heterogeneity, and drug tolerance during infection, we pretreated THP-1 macrophages with nontoxic doses of well-established inhibitors of phagosomal acidification [bafilomycin A1 (BafA1), ammonium chloride (NH_4Cl), and chloroquine (CQ)], infected them with *Mtb*/Mrx1-roGFP2, and measured E_{MSH} (12, 20, 49–51). Pretreatment with BafA1/ NH_4Cl /CQ uniformly diminished the fraction of *Mtb* displaying reductive E_{MSH} at 24 hours p.i. (Fig. 3A). Next, we examined whether phagosomal pH enhanced drug tolerance during infection. THP-1 macrophages with or without BafA1 pretreatment were infected with *Mtb* for 24 hours and exposed to 3 MIC of Inh for an additional 48 hours before lysis and enumeration of viable counts. The addition of BafA1 further increased Inh-mediated killing of *Mtb* by fivefold (Fig. 3B). A similar increase in killing was observed upon substitution of Inh with rifampicin (Rif) or BafA1 with CQ (Fig. 3, B and C). We noted that although CQ and BafA1 uniformly increased killing efficacy of Inh and Rif, the effect was more pronounced in the case of Inh (Fig. 3, B and C). Consistent with findings in THP-1 cells, infection of peritoneal macrophages from BALB/c mice also led to a pH-dependent increase in the E_{MSH} -reduced fraction and Inh tolerance in *Mtb* (fig. S10, A and B). These results suggest that phagosomal pH is a potent enhancer of multidrug tolerance in *Mtb*.

We next examined whether the drug tolerance and redox heterogeneity displayed by intraphagosomal *Mtb* were a reversible phenotypic change or a stable genetic variation. We flow-sorted THP-1 macrophages infected with *Mtb*/Mrx1-roGFP2 for 24 hours into E_{MSH} -reduced and E_{MSH} -basal fractions, lysed the macrophages in 7H9 broth, and measured E_{MSH} of the released *Mtb*. Incubation in 7H9 broth resulted in the loss of redox heterogeneity within 2 hours, indicating that the macrophage environment supports the emergence of drug-tolerant E_{MSH} -reduced population (Fig. 3D). When these redox-homogeneous bacteria were used to reinfect THP-1 macrophages with or without CQ pretreatment, both the heterogeneity in E_{MSH} and tolerance to Inh returned in untreated macrophages but not in CQ-treated macrophages (Fig. 3, D and E). Last, the bacteria that survived Inh treatment inside THP-1 macrophages showed an MIC comparable to the parental strain in 7H9 broth (fig. S10C). We conclude that pH- and redox-dependent tolerance of *Mtb* inside macrophages was due to reversible phenotypic changes rather than stable genetic mutations.

Phagosomal pH and redox heterogeneity drive drug tolerance during HIV-TB coinfection

Limited acidification is one of the hallmarks of *Mtb*-containing alveolar macrophages derived from HIV-TB-coinfected patients (52). We reasoned that pH- and redox-driven tolerance to anti-TB drugs could contribute to the lower TB treatment success rates commonly observed in HIV-TB-coinfected patients (53). To test this idea, we used the U1 monocytic cell line model of HIV-TB coinfection (54). U1 cells are derived from U937 monocytes wherein two copies of the HIV-1 genome are integrated and viral replication can be induced by phorbol 12-myristate 13-acetate (PMA) and tumor necrosis factor- α (55, 56). We confirmed viral replication by monitoring the expression of the HIV-1 *gag* transcript by quantitative reverse transcription polymerase chain reaction (qRT-PCR). Treatment with PMA (5 ng/ml) induced HIV-1 replication in a time-dependent manner in U1 cells (Fig. 4A). Next, we infected PMA-treated U1

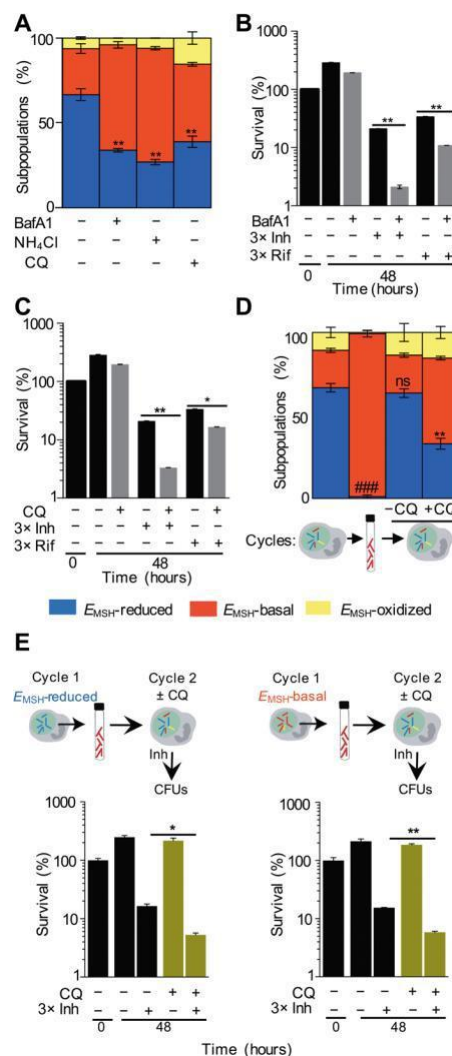


Fig. 3. Phagosomal pH is required for the redox-dependent multidrug tolerance of *Mtb*. (A) THP-1 macrophages—untreated or pretreated with 10 nM BafA1, 10 mM NH_4Cl , or 10 mM CQ—were infected with *Mtb*/Mrx1-roGFP2, and percent distribution of redox-diverse fractions was measured at 24 hours p.i. $^{**}P < 0.01$, by Mann-Whitney test to compare the E_{MSH} -reduced fraction with untreated sample. (B and C) THP-1 macrophages, untreated or pretreated with 10 nM BafA1 or 10 mM CQ, were infected with WT *Mtb* for 24 hours and exposed to Inh (2.18 mM) or Rif (1 mM) or left unexposed for an additional 48 hours. Percent survival was quantified by normalizing the CFU in drug-treated samples at 48 hours against untreated samples at 0 hours. $^{*}P < 0.05$, $^{**}P < 0.01$, by Mann-Whitney test. (D) THP-1 macrophages were infected with *Mtb*/Mrx1-roGFP2, and E_{MSH} was measured at 24 hours p.i. After this, intraphagosomal bacteria were released and incubated in 7H9-albumen-dextrose-sodium chloride for 2 hours, and E_{MSH} was determined. The 7H9-ADS-adapted *Mtb* was used to reinfect fresh THP-1 macrophages, with or without pretreatment with 10 mM CQ, and E_{MSH} was measured at 24 hours p.i. $^{**}P < 0.01$, $^{***}P < 0.001$, by Mann-Whitney test. Number signs (#) compare E_{MSH} -reduced fractions between intramacrophage and 7H9-ADS-adapted *Mtb*. Asterisks (*) compare E_{MSH} -reduced fractions between untreated and CQ-treated samples. (E) THP-1 macrophages harboring E_{MSH} -reduced and E_{MSH} -basal bacteria were flow-sorted at 24 hours p.i. (cycle 1 infection), and bacteria were released into 7H9-ADS. At 24-hour incubation, 7H9-ADS-adapted *Mtb* were used to infect THP-1 macrophages, with or without pretreatment with 10 mM CQ, for 24 hours (cycle 2 infection), and Inh tolerance was determined as mentioned earlier. $^{*}P < 0.05$, $^{**}P < 0.01$, by Mann-Whitney test. Data shown in each panel are the results of three independent experiments performed in triplicate (means \pm SD). ns, no significant difference ($P > 0.05$).

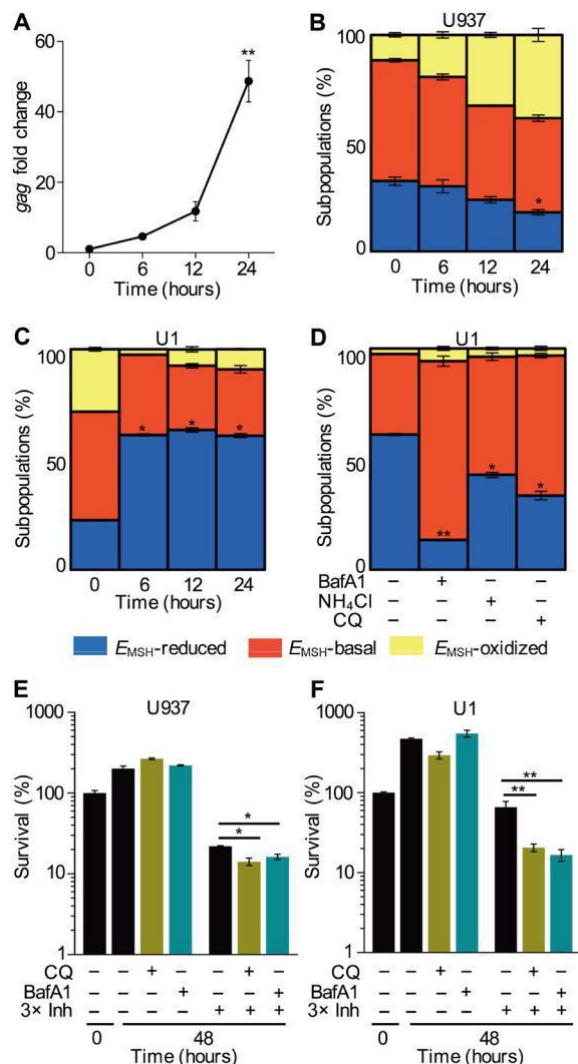


Fig. 4. Phagosomal pH and redox heterogeneity drive drug tolerance during HIV-TB coinfection. (A) The course of HIV-1 replication upon stimulation of the U1 promonocytic cell line with PMA (5 ng/ml). Viral load was monitored by *gag* qRT-PCR. ** $P < 0.01$, by Mann-Whitney test comparing *gag* expression with 0 hours. U937 (uninfected HIV-1 control) (B) and U1 macrophages (C) were stimulated with PMA and infected with *Mtb*/Mrx1-roGFP2, and percent distribution of redox-diverse fractions was measured over time. * $P < 0.05$, by Mann-Whitney test. Asterisks (*) compare *EMSH*-reduced fraction at various time points with 0 hours. (D) U1 macrophages—untreated or pretreated with 10 nM BafA1, 10 mM NH₄Cl, and 10 mM CQ—were infected with *Mtb*/Mrx1-roGFP2, and percent distribution of redox-diverse fractions was measured at 12 hours p.i. * $P < 0.05$, ** $P < 0.01$, by Mann-Whitney test. Asterisks (*) compare *EMSH*-reduced fractions between untreated and BafA1/NH₄Cl/CQ-treated samples. U937 (E) and U1 macrophages (F), untreated or pretreated with 10 mM CQ or 10 nM BafA1, were infected with WT *Mtb* for 12 hours and exposed to Inh (2.18 mM) or left unexposed for an additional 48 hours. Bacillary load was determined by CFU enumeration, and percent survival was quantified by normalizing the CFU in drug-treated samples at 48 hours against untreated samples at 0 hours. * $P < 0.05$, ** $P < 0.01$, by Mann-Whitney test. Data shown in each panel are the results of three independent experiments performed in triplicate (means \pm SD).

and U937 (uninfected HIV-1 control) with *Mtb*/Mrx1-roGFP2 and measured heterogeneity in *EMSH*. Both U1 and U937 macrophages showed the emergence of redox-diverse fractions upon infection. However, a marked increase in the *EMSH*-reduced fraction was clearly

evident in U1 compared to U937 macrophages (Fig. 4, B and C), indicating that HIV-1 replication is accompanied with the rise of *EMSH*-reduced population. Furthermore, treatment with BafA1, NH₄Cl, and CQ uniformly decreased the *EMSH*-reduced fraction in U1 (Fig. 4D), confirming the role of phagosomal pH in the emergence of redox heterogeneity. Last, we tested Inh tolerance in U1 and U937 cells, as described earlier. Consistent with the increased *EMSH*-reduced fraction, a significantly higher proportion of *Mtb* tolerates exposure to 3 MIC of Inh in U1 ($65.9 \pm 11.67\%$) versus U937 ($21.93 \pm 0.42\%$) ($P = 0.0015$) (Fig. 4, E and F). As expected, pretreatment with CQ/BafA1 increased Inh-mediated killing of *Mtb* in U1 and U937 (Fig. 4, E and F). These results suggest that the phagosomal acidification encountered by *Mtb* inside HIV-*Mtb*-coinfected macrophages facilitates the development of a redox-altered drug-tolerant population.

The drug-tolerant *EMSH*-reduced population is replicative inside macrophages

We next examined whether drug tolerance exhibited by the *EMSH*-reduced population is associated with slow replication as shown in several bacteria, including *Mtb* (1, 4, 57). We used an unstable replication clock plasmid, pBP10, which is uniformly lost from replicating but not from nonreplicating *Mtb* (58). Because the plasmid is resistant to kanamycin (Kan), its retention or loss can be easily estimated by determining colony-forming units (CFUs) on Kan-containing medium. We infected THP-1 macrophages with pBP10-containing *Mtb*/Mrx1-roGFP2. At 0, 24, and 72 hours p.i., 0.5×10^6 macrophages harboring an *EMSH*-reduced or *EMSH*-basal population were flow-sorted, after which, the bacteria were released and differences in replication were measured by enumerating Kan^r (Kan-resistant) and Kan^s (Kan-sensitive) colonies. Expression of the pBP10 plasmid in *Mtb*/Mrx1-roGFP2 did not influence redox heterogeneity during infection (fig. S11A). The pattern of pBP10 plasmid loss indicated that both populations were replicative; however, the plasmid loss was faster over time in the *EMSH*-reduced population than the *EMSH*-basal population (Fig. 5, B and C). For example, at 72 hours p.i., only $17.8 \pm 0.2\%$ of cells retained pBP10 in the *EMSH*-reduced population as opposed to $61.19 \pm 0.02\%$ in the *EMSH*-basal population (Fig. 5, B and C). The cumulative bacterial burden, which provides the total number of living, dead, or damaged *Mtb* based on a mathematical model established for the clock plasmid (58), also confirmed the comparatively higher replication rate in the *EMSH*-reduced population (Fig. 5, B and C).

We examined the health of *Mtb* in the *EMSH*-reduced and *EMSH*-basal fractions using a fluorogenic cell-permeable dye calcein violet-acetoxy-methyl ester (CV-AM), an established metabolically active (59, 60). THP-1 macrophages infected for 24 hours with *Mtb*/Mrx1-roGFP2 were flow-sorted, and then, bacteria were released from the *EMSH*-reduced and *EMSH*-basal fractions and stained with CV-AM. Bacilli in the *EMSH*-reduced ($91.5 \pm 0.07\%$) and *EMSH*-basal fractions ($99.1 \pm 0.14\%$) showed strong CV-AM fluorescence, indicating healthy metabolic activity (Fig. 5D). As expected, metabolically active *Mtb* cultured in 7H9 broth at 37°C showed $91.3 \pm 0.99\%$ CV-AM staining as compared to negligible staining in bacteriostatic cells incubated at 4°C (Fig. 5D). Treatment of *Mtb*/Mrx1-roGFP2 with 2 mM cell-permeable thiol-reductant dithiothreitol (DTT) induces a reductive shift in *EMSH* (320 mV) without any influence on metabolism and viability in vitro (20). Consistent with this, $83.9 \pm 2.97\%$ of DTT-treated *Mtb* cells scored positive for CV-AM staining (Fig. 5D). Together, these results suggest that the drug-tolerant

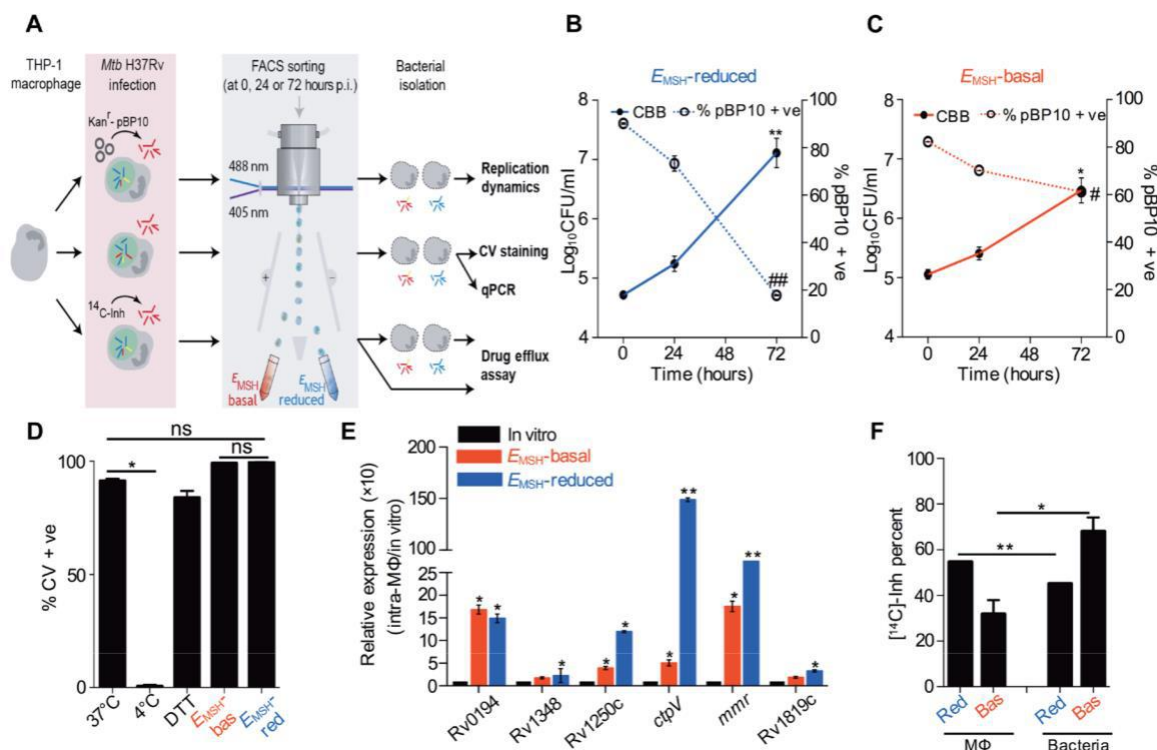


Fig. 5. The drug-tolerant *E*_{MSH}-reduced population is replicative and has high efflux pump activity. (A) Graphical depiction of Mrx1-roGFP2-coupled flow-sorting strategy to determine replication dynamics, metabolic state, and drug efflux activity in intramacrophage *E*_{MSH}-reduced and *E*_{MSH}-basal populations. (B and C) THP-1 macrophages were infected with pBP10-containing *Mtb*/Mrx1-roGFP2. At indicated time points, macrophages harboring *E*_{MSH}-reduced and *E*_{MSH}-basal bacteria were flow-sorted, and bacteria were released and plated in the presence or absence of kanamycin (Kan). The frequency of pBP10 loss and increase in cumulative bacterial burden (CBB) were calculated. **P* < 0.05, ***P* < 0.01, #*P* < 0.05, ##*P* < 0.01, by Kruskal-Wallis test with Dunn's correction over time p.i. Asterisks (*) and number signs (#) compare CFU per milliliter and percentage of pBP10 +ve bacteria over time p.i., respectively. (D) THP-1 macrophages were infected with *Mtb*/Mrx1-roGFP2, and at 24 hours p.i., the redox state of intraphagosomal *Mtb*/Mrx1-roGFP2 thiols was fixed using *N*-ethylmaleimide. Bacteria were released from macrophages and stained with calcein violet-AM (CV-AM). The CV-AM staining and *E*_{MSH} status of *Mtb* cells were determined using multiparameter flow cytometric analysis. As a control, we performed CV-AM staining of *Mtb* grown in 7H9 broth for 24 hours at 4° and 37°C. * *P* < 0.05, by Mann-Whitney test. (E) THP-1 macrophages harboring *E*_{MSH}-reduced and *E*_{MSH}-basal bacteria were flow-sorted at 24 hours p.i., bacterial RNA was isolated, and expression of efflux pumps was measured by qRT-PCR. Expression was compared with in vitro control *Mtb*, and fold change was quantified after normalizing by 16S ribosomal RNA. **P* < 0.05, ***P* < 0.01, by Mann-Whitney test for comparison with in vitro control *Mtb*. (F) THP-1 macrophages were infected with *Mtb*/Mrx1-roGFP2 bacteria preloaded with [14C]-Inh. At 24 hours p.i., macrophages harboring *E*_{MSH}-reduced (Red) and *E*_{MSH}-basal (Bas) bacteria were sorted and bacteria released. The relative distribution of radioactive [14C]-Inh was measured in bacterial and macrophage (MF) fractions. **P* < 0.05, ***P* < 0.01, by Mann-Whitney test. Data shown in each panel are the results of two independent experiments performed in triplicate (means ± SD). ns, no significant difference (*P* > 0.05).

*E*_{MSH}-reduced population is replicative and metabolically active inside macrophages.

Redox-diverse populations of *Mtb* show differential activation of efflux pumps

Induction of efflux pumps is associated with drug tolerance in replicating *Mtb* during infection (6). We investigated whether the drug-tolerant *E*_{MSH}-reduced population exhibited variation in efflux pump activity relative to the *E*_{MSH}-basal population. THP-1 macrophages infected for 24 hours with *Mtb*/Mrx1-roGFP2 were flow-sorted into *E*_{MSH}-reduced and *E*_{MSH}-basal populations, and bacterial RNA was isolated for qRT-PCR of efflux pump transcripts. As a control, we performed qRT-PCR of efflux pumps on *Mtb* grown in 7H9 broth. We selected efflux pumps (Rv0194, Rv1348, Rv1250, *ctpV*, *mmr*, and Rv1819c) that are induced in intraphagosomal *Mtb* upon exposure to anti-TB drugs (44, 61–64). The transcripts of *ctpV*, *mmr*, Rv1348, and Rv1250c were enriched in the *E*_{MSH}-reduced fraction (Fig. 5E). We tested pH- and redox-dependent expression of efflux pumps by examining transcripts in response to pH 6.2, pH 4.5, and 2 mM DTT

in vitro. Each of these conditions uniformly induces reductive shift in *E*_{MSH} of *Mtb* in vitro (12, 20). All of these treatments increased expression of the efflux pumps (fig. S11, B and C). As a control, we analyzed efflux pump expression in an *Mtb* strain lacking the anti-oxidant buffer MSH (*MtbDmsH*); this strain maintains oxidative *E*_{MSH} (> 240 mV) at both neutral and acidic pH (20, 65). The expression of pH-inducible efflux pumps was significantly down-regulated in *MtbDmsH* relative to WT *Mtb* (*P* < 0.05) (fig. S11D), suggesting redox-dependent regulation of efflux pump expression in *Mtb*.

To clarify the association between efflux pump activity and *E*_{MSH} of *Mtb*, we assessed the steady-state distribution of Inh in *E*_{MSH}-reduced and *E*_{MSH}-basal populations inside THP-1 macrophages using [14C]-labeled Inh. We infected THP-1 macrophages with *Mtb*/Mrx1-roGFP2 cells preloaded with [14C]-Inh (0.5 mCi/ml for 2 hours). At 24 hours p.i., equal numbers of macrophages harboring either *E*_{MSH}-reduced or *E*_{MSH}-basal populations were sorted using flow cytometry. We chose the 24-hour time point because bacterial load was comparable in both populations (10⁶ CFU/ml). Infected macrophages were lysed, the bacterial (pellet) and macrophage (supernatant)

fractions were separated, and [¹⁴C]-labeled Inh radioactivity was measured. The distribution of [¹⁴C]-Inh was different in macro-phages containing *EMSH*-reduced *Mtb* versus *EMSH*-basal *Mtb* and in the bacteria themselves. Whereas macrophages harboring *EMSH*-reduced *Mtb* showed high counts for [¹⁴C]-Inh and corresponding lower counts remained in the bacteria, the *EMSH*-basal population showed an inverse drug distribution. These data indicate higher efflux from the *EMSH*-reduced population into macrophages (Fig. 5F). Direct comparison of [¹⁴C]-Inh counts in *EMSH*-reduced and *EMSH*-basal bacterial pellets confirmed lower accumulation of the drug in the former (Fig. 5F). In summary, our data indicate that variations in efflux pump activity can be one of the factors managing drug tolerance in the *EMSH*-reduced population during infection.

CQ counteracts drug tolerance and relapse in vivo

Given our findings that acidic pH promotes redox heterogeneity and enhances drug tolerance in vitro, we sought to determine the impact of pharmacological inhibition of phagosomal acidification on drug tolerance in vivo. We used the antimalarial drug CQ, which deacidifies endosomes and lysosomes (66, 67), to test *Mtb*'s response to Inh in a chronic murine model of infection (Fig. 6A) (68).

We treated chronically infected BALB/c mice (4 weeks p.i.) with Inh (25 mg/kg body weight), CQ (10 mg/kg body weight), or Inh along with CQ. After 2 and 8 weeks of therapy, we harvested the lungs and quantified the recovered bacteria. As reported (68), Inh monotherapy reduced the bacterial load from 10⁶ to 10⁴ at 2 weeks (*P* = 0.00012) and 10³ per lung at 8 weeks (*P* = 0.0022) of treatment (Fig. 6B). CQ treatment alone showed no effect on bacterial viability over time (Fig. 6B). Relative to the control regimen (Inh alone), the addition of CQ did not alter lung CFUs after 2 weeks of treatment (Fig. 6B). However, 8 weeks of treatment with a combination of CQ with Inh (CQ plus Inh) completely sterilized the lungs of mice compared to 10³ CFUs in the animals treated with Inh alone (Fig. 6B). The gross and histopathological changes observed in the lungs after 8 weeks of therapy were proportionate with the bacillary load observed (Fig. 6, D and E, and fig. S12A). After 8 weeks of treatment, the extent of pulmonary tissue destruction was highest in the untreated (score, 4) and CQ-treated animals (score, 3), intermediate in the case of the Inh-treated animals (score, 2), and negligible in CQ plus Inh-treated animals (score, 1 or 0). We also examined whether adjunct therapy with CQ for 8 weeks increased the efficacy of Rif (10 mg/kg body weight). The addition of CQ substantially reduced the fraction of Rif-tolerant *Mtb* in animal lungs (*P* = 0.021 for Rif alone versus a combination of CQ with Rif) (Fig. 6, C to E, and fig. S12A). However, the influence of CQ in reducing tolerance was more notable in the case of Inh as compared to Rif.

Because the pathophysiology of human TB is more closely recapitulated in guinea pigs (69), we aerosol-infected outbred Hartley guinea pigs with *Mtb*, followed 4 weeks later by treatment with Inh, CQ, or CQ plus Inh for an additional 8 weeks, and then estimated the lung bacillary load. The bacterial burden in the lungs of guinea pigs was 10³ CFUs in Inh-treated animals and 10⁵ CFUs in CQ-treated animals, compared to 100 CFUs in CQ plus Inh-treated animals (Fig. 6F). The effectiveness of CQ plus Inh was also reflected in the lung histopathology of guinea pigs (Fig. 6G and fig. S12B). Studying relapse can be another predictor of therapeutic efficacy in TB. There-fore, we aerosol-infected mice with WT *Mtb*, followed 4 weeks later by treatment of infected animals with Inh or CQ plus Inh for 8 weeks. As shown earlier, 8 weeks of CQ plus Inh treatment completely sterilized

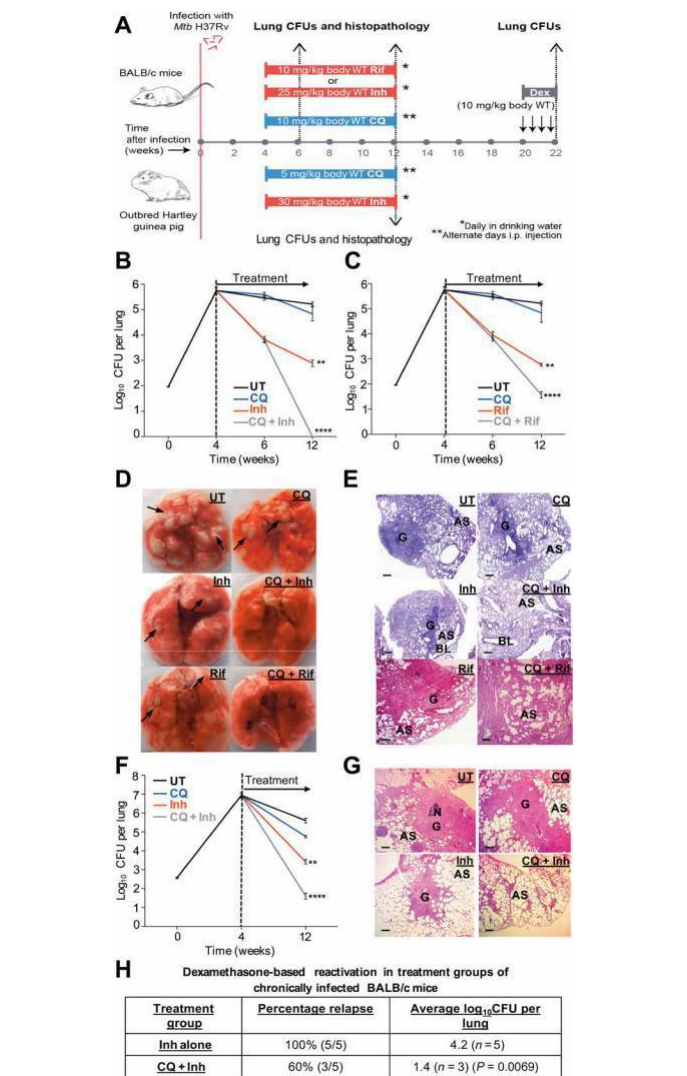


Fig. 6. CQ counteracts drug tolerance and reduces relapse in vivo. (A) Strategy to investigate the efficacy of CQ in reducing tolerance against Inh and Rif and post-therapeutic relapse in vivo. BALB/c mice (*n* = 6) were given an aerosol challenge with WT *Mtb*. From 4 weeks p.i. onward, groups of mice were left untreated or treated with anti- TB drugs (Inh/Rif) alone or in combination with CQ (CQ + Inh/ CQ + Rif). (B and C) Bacterial CFUs were measured in the lungs at the indicated time points. ***P* < 0.01, *****P* < 0.0001, by Kruskal-Wallis test with Dunn's correction across experi-mental groups at 12 weeks p.i. (D) Gross pathology of the lungs of WT *Mtb*-infected mice at 8 weeks of treatment across experimental groups. (E) Hematoxylin and eosin–stained lung sections (8 weeks of treatment) from mice infected with WT *Mtb* across experimental groups. The pathology sections show granuloma (G), alveolar space (AS), and bronchiole lumen (BL). All images were taken at 40 magnification. Scale bars, 200 mm. (F) Outbred Hartley guinea pigs (*n* = 6) were given aerosol challenge with WT *Mtb*, and efficacy of CQ in reducing Inh tolerance was assessed as described in (B) and (C). ***P* < 0.01, *****P* < 0.0001, by Kruskal-Wallis test with Dunn's correction across experimental groups at 12 weeks p.i. (G) Hematoxylin and eosin–stained lung sections (8 weeks of treatment) from guinea pigs infected with WT *Mtb* across experimental groups. The pathology sections show granuloma (G), alveolar space (AS), and necrotic core (N). All images were taken at 40 magnification. Scale bars, 200 mm. (H) Dexamethasone-induced reactivation of *Mtb* from the lungs of BALB/c mice (*n* = 5) after treatment with Inh alone or a combination of CQ plus Inh. Mann-Whitney test was used to compare the relapse frequency (Inh alone versus CQ + Inh combination) for effectiveness of CQ therapy (*P* = 0.0069). Data shown in each panel are the results of two independent experiments (means ± SD). ns, no significant difference (*P* > 0.05).

mouse lungs. At 20 weeks p.i., which was 8 weeks after completion of therapy, mice received immunosuppressant dexamethasone (10 mg/kg body weight) for 2 weeks, and the lung bacillary load was determined at 22 weeks p.i. Relapse of disease was observed in five of five Inh-treated mice with bacterial loads of 2×10^4 CFUs in the lungs. Only three of five CQ plus Inh-treated mice relapsed, with only 30 CFUs in the lungs ($P = 0.0069$) (Fig. 6H).

Although in vitro studies indicate that CQ mainly exerts its influence on intracellular *Mtb* by raising the vacuolar pH (70), CQ can interfere with other cellular processes such as DNA synthesis, generation of ROS, and necrosis (71, 72). Therefore, we questioned whether the effect of CQ in reducing tolerance was associated with pH alkalinization in vivo. Using Magic Red cathepsin B substrate that fluoresces only upon cleavage by cathepsin B protease inside acidic lysosomes (73), we confirmed that 6 weeks of CQ treatment raised the vacuolar pH of macrophages isolated from the lungs of mice chronically infected with *Mtb* (fig. S13, A and B). Other antibacterial mechanisms such as ROS production and necrosis were not stimulated in macrophages derived from the lungs of mice chronically infected with *Mtb* after 6 weeks of treatment with CQ plus Inh as compared to Inh or CQ alone (fig. S13, A, C, and D). Together, these results confirm that adjunct therapy with CQ counteracts drug tolerance and reduces disease relapse.

CQ exhibits no adverse interaction with anti-TB drugs Excellent oral bioavailability, oral human pharmacokinetics (half-life of 10 to 15 days), high tissue penetration, and years of clinical use in humans (74) make CQ a good candidate for developing new therapeutic combinations for the treatment of TB. We investigated the pharmacological compatibility of CQ by measuring its potential drug-drug interactions with first-line anti-TB drugs (Inh or H, Rif

or R, Emb or E, and Pza or Z) given as a combination. A single-dose pharmacokinetic interaction test was performed by administering anti-TB drugs with and without CQ [10 mg/kg body weight, intra-peritoneally (i.p.)] in mice. Another group of mice was dosed with CQ (10 mg/kg body weight, i.p.) to compare the pharmacokinetic behavior of CQ in the presence of combination therapy (Fig. 7A). Plasma samples were analyzed for individual drugs using liquid chromatography–mass spectrometry, and key pharmacokinetic parameters such as maximum plasma concentration (C_{max}) and area under the plasma concentration-time curve (AUC_{last}) were calculated as a ratio for combination versus single-treatment groups. Pharmacokinetic profiles revealed no adverse drug-drug interactions when CQ was coadministered with HREZ (Fig. 7, B and G). C_{max} and AUC_{last} for CQ alone was 228.5 ng/ml and 1358.0 ng-hour/ml and 297.2 ng/ml and 1358.0 ng-hour/ml for HREZ, respectively (Fig. 7, B and G).

The plasma pharmacokinetic profiles of anti-TB drugs remained largely unchanged in the presence of CQ. We observed no major interaction for Rif, Emb, or Pza in the presence or absence of CQ (Fig. 7, D to G) because C_{max} and AUC_{last} were within 80 to 125% criteria for equivalence (Fig. 7G) (75). Comparative ratios of C_{max} and AUC_{last} for Rif, Emb, and Pza, with and without CQ, were close to one except for Inh, which showed a minor interaction (C_{max} ratio, 0.685), although AUC_{last} was not affected (Fig. 7, C and G). This minor influence of CQ on the pharmacokinetics of Inh may be due to the effect of CQ in reducing Inh influx in the intestines (76). Overall, the pharmacokinetic results suggested no adverse drug-drug interactions between the HREZ combination regimen versus CQ and vice versa. In summary, our study shows an effect of CQ on drug susceptibility, no major drug-drug interaction with HREZ, and enhanced in vivo efficacy of CQ-based combinations. With years of safe clinical history for CQ, these findings suggest

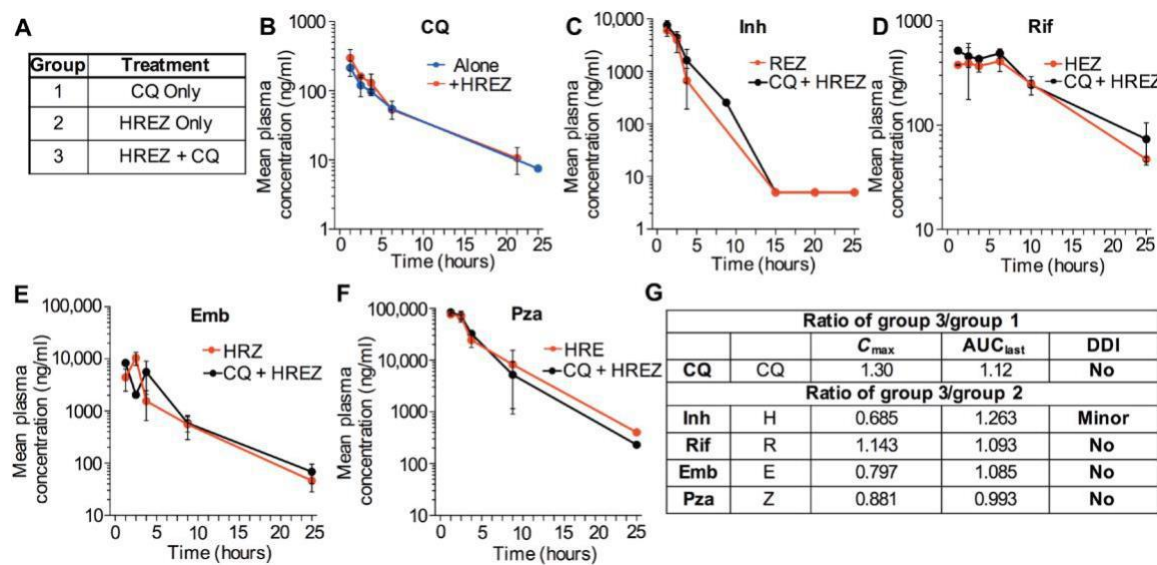


Fig. 7. CQ exhibits no adverse interactions with anti-TB drugs. (A) The table indicates three groups of treatment in BALB/c mice used in the pharmacokinetic study: CQ alone, front line anti-TB combination therapy (HREZ), and combination (CQ + HREZ). (B to F) Line plots indicate pharmacokinetic profiles of CQ and individual drugs of the anti-TB therapy regimen analyzed individually and in the presence of each other in plasma of animals over 24 hours. No significant difference was observed between groups at each time point indicated in each panel by Mann-Whitney test ($P > 0.05$). (G) The table depicts ratios of C_{max} and AUC_{last} of individual drugs alone or in combination to analyze drug-drug interaction. Doses used are the following: CQ, 10 mg/kg body weight, i.p.; Inh/H, 25 mg/kg body weight, p.o.; Rif/R, 10 mg/kg body weight, p.o.; Emb/E, 200 mg/kg body weight, p.o.; Pza/Z, 150 mg/kg body weight, p.o. p.o., per os consumption; BDL, below detection limit. All data are means \pm SD of concentrations at each time point of samples in triplicates ($n = 3$ animals per group).

that CQ could be repurposed for developing new curative combinations for TB.

DISCUSSION

Generation of phenotypic heterogeneity and metabolic quiescence in response to stresses induced by immune activation is the most commonly invoked mechanism of antibiotic tolerance in *Mtb* (1, 4). However, clinical evidence in humans indicates that tolerance can also be associated with growing bacterial populations (77, 78). Consistent with this idea, early tolerance was documented in actively multiplying *Mycobacterium marinum* and *Mtb* in zebrafish larvae and in macrophages, respectively (6). In the present study, we showed a dominant role of phagosomal acidification in facilitating heterogeneity in the redox physiology of *Mtb* to generate an actively replicating, drug-tolerant population exhibiting higher antioxidant capacity (*EMSH*-reduced) during infection. Our study constitutes an important foundation linking the macrophage environment with the core redox physiology of *Mtb* to promote drug tolerance in replicating *Mtb*, a population not typically associated with tolerance.

Host-induced oxidative stress is a major environmental stress encountered by *Mtb* during infection and is further exacerbated by anti-TB drugs (12, 79). Because a modest decrease in vacuolar pH is the earliest cue *Mtb* encounters (18), a pH-dependent reductive shift in *EMSH* might offer cross-protection to oxidative stress generated by immune activation and drugs. This is supported by the identification of a small molecule (AC2P36) that interferes with thiol homeostasis at acidic pH and increases vulnerability to antibiotics in vitro (80). We also found that the expression of drug efflux pumps and consequent accumulation of antibiotics in *Mtb* populations are also dependent on the pH-induced remodeling of intramycobacterial *EMSH*. Because efflux pumps have recently been shown to export oxidatively damaged proteins in *Mtb* (81), the pH-responsive induction of efflux pumps may be an elegant adaptation strategy to maintain redox homeostasis and tolerance in the face of antibiotics and host immune pressures. Consistent with this idea, the *Mtb* Rv1258c efflux pump is required for both survival and drug efflux during infection (6).

Because acidic pH encountered inside macrophages does not perturb intramycobacterial pH homeostasis (82), it is more likely that the phagosomal pH-dependent selection of an *EMSH*-reduced population is part of a bacterial adaptation program during infection. In support of this notion, we have recently found that a redox-sensitive transcription factor, WhiB3, is required to generate an *EMSH*-reduced population in response to phagosomal acidification (20). As a consequence, a WhiB3-deficient strain showed a growth defect in macrophages and guinea pigs (34) and also exhibited increased susceptibility to Inh. Acidic pH-mediated changes in gene expression and redox potential of *Mtb* were also reported to be dependent on the PhoPR two-component system (83), indicating overlapping roles of WhiB3/PhoPR in modulating *Mtb* adaptation to pH stress. Data from our transcriptional profiling also align with the adaptation model wherein the drug-tolerant population (*EMSH*-reduced) showed enhanced expression of stress-responsive regulons relative to the drug-sensitive fraction (*EMSH*-basal) inside macrophages. However, although heterogeneity in *Mtb* populations has been reported during infection (4, 78), it was unclear whether there were variations in the expression of stress regulons or virulence factors in *Mtb* populations as seen with other pathogens including *Salmonella typhimurium* and *Yersinia pseudotuberculosis*

(84, 85). Our data demonstrate heterogeneity in the expression of several regulators involved in sensing toxic metals and oxidative stress in redox-altered populations. We also observed a major realignment of sulfur metabolism and proposed that the flux of reduced sulfur metabolites such as CySH into Fe-S cluster assembly, reverse transsulfuration, SAM biosynthesis, and MSH biosynthesis is likely to coordinate *Mtb*'s defense against antibiotics. Deviations in CySH flux contribute to potentiation of the mycobactericidal efficacy of anti-TB drugs (86). Furthermore, increased expression of SAM-dependent methyl transferases in *EMSH*-reduced bacteria can promote drug tolerance by *N*-methylation of antibiotics (40). These transcriptional changes—along with the reduced tolerance shown by *MtbDmetB*, *MtbDsufr*, and *MtbDwhiB3*—led us to propose a model of how phagosomal acidification and bacterial pathways integrate to reset *Mtb*'s redox physiology for successfully counteracting anti-TB drugs (fig. S14).

Our data also suggest that redox-dependent drug tolerance in replicating *Mtb* is multifactorial. Although the deletion of single redox-responsive pathways (WhiB3, SufR, and MetB) exhibited substantial influence on drug tolerance, complete clearance of *Mtb* was not achieved. Similar to our findings, drug tolerance in the growth-arrested *Mtb* population possibly requires activation of multiple stress regulons and toxin-antitoxin modules (DosR, PhoP, MprA, and MazEF) (1). These studies imply that targeting few bacterial genes or pathways is unlikely to severely affect the ability of *Mtb* to mobilize drug tolerance in response to host-induced pressures. Conversely, targeting host cues that alter the physiology of *Mtb* could be an effective mechanism to diminish phenotypic heterogeneity-driven drug tolerance. Our animal data showing the nearly sterilizing effect of CQ in combination with anti-TB drugs provide a compelling argument for targeting vacuolar pH to subvert early emergence of drug tolerance in vivo. Although CQ reinstates redox homogeneity and drug susceptibility mainly by increasing phagosomal pH, other immunomodulatory properties of CQ such as iron depletion (70), blocking phagosomal maturation and autophagy (66), and reversing inflammation-dependent efflux pumps (51) could also contribute to the effect of CQ on multidrug tolerance in vivo. It has been recently shown that CQ potentiates the antimycobacterial activity of Inh and Pza in immune-activated macrophages (51). Because shortening TB chemotherapy requires rapid sterilization of *Mtb*, our study provides empirical evidence that targeting phagosomal acidification by small molecules has the potential to provide relapse-free control by subverting redox heterogeneity. Because CQ is clinically used, stable, cost effective, and highly tolerable with few side effects, it can be conveniently repurposed to formulate new combinations with the current anti-TB regimen to reduce therapy duration. CQ also reduced redox heterogeneity and Inh tolerance in a HIV-TB coinfection background. Along with clinical evidence showing anti-HIV properties of CQ (87), this raises the possibility of potentiating current anti-TB and anti-HIV therapies by CQ. Last, redox-mediated multidrug tolerance may be relevant to other chronic pathogens. For example, heightened antioxidant capacity is linked to the acquisition of phenotypic antibiotic resistance in the human pathogen *Pseudomonas aeruginosa* (88). Thus, our findings may have broad relevance to several human pathogens where a sterilizing cure is therapeutically challenging.

Although CQ therapy reduced drug tolerance in vivo, several issues remain to be addressed before it can be combined with the standard anti-TB therapy. First, it needs to be investigated whether

a combination of CQ with current therapeutic regimens reduces therapy duration and facilitates the development of immunological memory to prevent relapse. Second, the efficacy of CQ in shortening regimens for drug-resistant *Mtb* infections remains to be evaluated. Third, despite treatment with anti-TB drugs, *Mtb* cells persist in animal tissues and the sputum of patients with TB in a metabolically altered state and remain undetectable by viable counts (89, 90). It will be interesting to investigate the impact of CQ on these heterogeneous subpopulations of *Mtb* that are difficult to detect and retain persister phenotypes in animal models. All these issues require further experimentation using animal models and prospective clinical trials to properly test the efficacy of CQ as adjunct anti-TB therapy.

MATERIALS AND METHODS

Study design

The overall objective of this study was to evaluate host and bacterial mechanisms underlying the emergence of redox heterogeneity and drug tolerance in *Mtb* during infection. First, we characterized the transcriptome of redox-diverse *Mtb* fractions (*EMSH*-reduced and *EMSH*-basal), which led to the identification of CySH metabolism of *Mtb* and phagosomal acidification as important factors coordinating redox-mediated drug tolerance inside macrophages. Next, we performed detailed mechanistic studies on the role of phagosomal acidification in generating drug-tolerant *EMSH*-reduced bacteria in macrophages infected with *Mtb* alone or coinfecting with HIV-1. We applied multiple approaches to studying replication dynamics, metabolic status, and efflux pump activity in *EMSH*-reduced and *EMSH*-basal *Mtb* inside macrophages. We then evaluated the licensed antimalarial drug CQ, which deacidifies phagosomes, in reducing tolerance to standard anti-TB drugs and relapse in animal models of *Mtb* infection. We assessed the pharmacological compatibility of CQ with first-line anti-TB drugs in mice. Animals were randomly allocated into groups and were identifiable with respect to their treatment. All studies were carried out as per guidelines pre-scribed by the Committee for the Purpose of Control and Supervision of Experiments on Animals, Government of India, with approval from the Institutional Animal Ethical Committee. Drug treatment and euthanasia were carried out in humane ways to minimize suffering for animals. All experiments were carried out in a bio-safety level 3 containment facility and approved by the Institutional Biosafety Committee.

In vivo experiments

For the chronic model of infection (68), 4- to 6-week-old female BALB/c mice ($n = 6$ per group) were infected by the aerosol route with 100 *Mtb* H37Rv bacilli using a Madison chamber aerosol generation instrument, housed for 4 weeks for progression of infection, and then left untreated or started under various treatment conditions: (i) 10 mg/kg body weight intraperitoneal doses of CQ on alternate days, (ii) 25 mg/kg body weight of Inh in drinking water daily, (iii) 10 mg/kg body weight of Rif in drinking water daily, (iv) a combination of CQ and Inh (CQ plus Inh) at earlier mentioned doses, and (v) a combination of CQ and Rif (CQ plus Rif) at the mentioned doses (68). At indicated time points of treatment, mice were euthanized, and the lungs were harvested for bacterial burden, gross pathology, and tissue histopathology analysis. The upper right lobe of the lungs of animals from each group was fixed in 10% neutral-buffered formalin. Fixed tissues were prepared as 5-mm-thick sec-

tions, embedded in paraffin, and stained with hematoxylin and eosin. Tissue sections were coded, and coded sections were analyzed by a certified pathologist to assess for granuloma formation and lung damage (91). Remaining tissue samples were homogenized in 2 ml of sterile 1 phosphate-buffered saline (PBS), serially diluted, and plated on 7H11-OADC agar plates supplemented with lyophilized BBL MGIT PANTA antibiotic mixture (polymyxin B, amphotericin B, nalidixic acid, trimethoprim, and azlocillin, as supplied by BD). Plates were incubated at 37°C for 3 weeks before colonies were enumerated.

For mice receiving treatment with Inh alone or a combination of CQ and Inh, all treatments were stopped at 12 weeks p.i. (when animals were found to be culture negative for *Mtb*) for remaining animals ($n = 5$ per group). Animals were further housed for 8 weeks without treatment, after which four intraperitoneal doses of dexamethasone at 10 mg/kg body weight were administered over 2 weeks for pan-immunosuppression. In the 22nd week p.i., animals in both groups were euthanized, and lung burden of reactivated *Mtb* was determined by plating lung homogenates for CFUs, as mentioned earlier.

Outbred Hartley guinea pigs ($n = 5$ per group) were given an aerosol challenge of 100 *Mtb* H37Rv (92) using a Madison chamber aerosol generation instrument, housed for 4 weeks for progression of infection, and then left untreated or started on treatment in one of three groups: (i) 5 mg/kg body weight intraperitoneal doses of CQ on alternate days, (ii) 30 mg/kg body weight of Inh in drinking water daily, and (iii) a combination of CQ and Inh (CQ plus Inh) at earlier mentioned doses. At 8 weeks after commencement of treatment, guinea pigs were euthanized, and lung burden of *Mtb* was determined by homogenizing organs in 5 ml of sterile 1 PBS, serial dilution, and plating on 7H11-OADC agar plates supplemented with PANTA. Upper right lobes of the lungs from different treatment groups were fixed in neutral-buffered formalin and prepared, as mentioned earlier, for histopathological analysis (91).

Statistical analysis

All statistical analyses were performed using GraphPad Prism software (version 6.0). All data indicated are means \pm SD except figs. S12 and S13, where median \pm interquartile range was plotted for animal groups. The Mann-Whitney rank sum test was used for comparison of nonparametric data between two experimental groups. Nonparametric multiple group comparisons were analyzed using the Kruskal-Wallis test with Dunn's post hoc correction. For overlap analysis of differentially expressed (DE) genes with other microarray studies, the significance of gene number overlap was determined by Fisher's exact test on a two-by-two contingency table (93). Differences with $P < 0.05$ were considered significant.

SUPPLEMENTARY MATERIALS

stm.sciencemag.org/cgi/content/full/11/518/eaaw6635/DC1

Materials and Methods

Fig. S1. Phenotypic drug tolerance in *Mtb* during infection.

Fig. S2. Flow cytometry-based quantification of redox heterogeneity in *Mtb* using Mrx1-roGFP2.

Fig. S3. *EMSH*-reduced population is tolerant to Inh.

Fig. S4. Transcriptome of *Mtb* from *EMSH*-reduced and *EMSH*-basal fractions.

Fig. S5. Measuring phagosomal pH of THP-1 macrophages infected with *Mtb*/Mrx1-roGFP2.

Fig. S6. The transcriptome of *Mtb* from the *EMSH*-reduced fraction overlaps with low pH-specific WhiB3 regulon.

Fig. S7. WT *Mtb* generates H₂S gas in a pH-dependent manner.

Fig. S8. Generation and characterization of *Mtb metB* and *Mtb sufR*.

Fig. S9. Deletion of *metB* and *sufR* does not impair growth and metabolism of *Mtb*.

Fig. S10. Phagosomal acidification is required for the redox-dependent multidrug tolerance of *Mtb*.

Fig. S11. Drug-tolerant *EMSH*-reduced population is replicative and has high efflux pump activity. Fig. S12. CQ counteracts drug tolerance in vivo to reduce lung tissue damage in chronic model of *Mtb* infection.

Fig. S13. Long-term CQ treatment of chronically infected BALB/c mice deacidifies macrophage pH without affecting oxidative stress and necrosis.

Fig. S14. Model depicting various mechanisms underlying redox-mediated drug tolerance in replicating *Mtb*.

Table S1. List of differentially expressed genes from DESeq2 for *EMSH*-reduced, *EMSH*-basal, and in vitro control samples.

Table S2. List of differentially expressed genes from DESeq2 for WT *Mtb*, *Mtb whiB3*, and *whiB3*-Comp strains at pH 6.6 and pH 4.5 used to specify the low pH-inducible *WhiB3* regulon. Table S3. List of *EMSH*-reduced and *EMSH*-basal differentially expressed genes used to generate custom heat maps.

Table S4. List of strains and primers used in this study.

References (94–112)

[View/request a protocol for this paper from Bio-protocol.](#)

REFERENCES AND NOTES

- Y. Liu, S. Tan, L. Huang, R. B. Abramovitch, K. H. Rohde, M. D. Zimmerman, C. Chen, V. Dartois, B. C. VanderVen, D. G. Russell, Immune activation of the host cell induces drug tolerance in *Mycobacterium tuberculosis* both in vitro and in vivo. *J. Exp. Med.* **213**, 809–825 (2016).
- J. MacMicking, Q.-w. Xie, C. Nathan, Nitric oxide and macrophage function. *Annu. Rev. Immunol.* **15**, 323–350 (1997).
- J. D. MacMicking, R. J. North, R. LaCourse, J. S. Mudgett, S. K. Shah, C. F. Nathan, Identification of nitric oxide synthase as a protective locus against tuberculosis. *Proc. Natl. Acad. Sci. U.S.A.* **94**, 5243–5248 (1997).
- G. Manina, N. Dhar, J. D. McKinney, Stress and host immunity amplify *Mycobacterium tuberculosis* phenotypic heterogeneity and induce nongrowing metabolically active forms. *Cell Host Microbe* **17**, 32–46 (2015).
- J. P. Sarathy, L. E. Via, D. Weiner, L. Blanc, H. Boshoff, E. A. Eugenini, C. E. Barry III, V. A. Dartois, Extreme drug tolerance of *Mycobacterium tuberculosis* in caseum. *Antimicrob. Agents Chemother.* **62**, e02266-17 (2018).
- K. N. Adams, K. Takaki, L. E. Connolly, H. Wiedenhoft, K. Wingless, O. Humbert, P. H. Edelstein, C. L. Cosma, L. Ramakrishnan, Drug tolerance in replicating mycobacteria mediated by a macrophage-induced efflux mechanism. *Cell* **145**, 39–53 (2011).
- Y. Wakamoto, N. Dhar, R. Chait, K. Schneider, F. Signorino-Gelo, S. Leibler, J. D. McKinney, Dynamic persistence of antibiotic-stressed mycobacteria. *Science* **339**, 91–95 (2013).
- B. B. Aldridge, M. Fernandez-Suarez, D. Heller, V. Ambraveswaran, D. Irimia, M. Toner, S. M. Fortune, Asymmetry and aging of mycobacterial cells lead to variable growth and antibiotic susceptibility. *Science* **335**, 100–104 (2012).
- E. H. Rego, R. E. Audette, E. J. Rubin, Deletion of a mycobacterial divisome factor collapses single-cell phenotypic heterogeneity. *Nature* **546**, 153–157 (2017).
- A. Sakatos, G. H. Babunovic, M. R. Chase, A. Dills, J. Leszyk, T. Rosebrock, B. Bryson, S. M. Fortune, Posttranslational modification of a histone-like protein regulates phenotypic resistance to isoniazid in mycobacteria. *Sci. Adv.* **4**, eaao1478 (2018).
- B. Javid, F. Sorrentino, M. Toosky, W. Zheng, J. T. Pinkham, N. Jain, M. Pan, P. Deighan, E. J. Rubin, Mycobacterial mistranslation is necessary and sufficient for rifampicin phenotypic resistance. *Proc. Natl. Acad. Sci. U.S.A.* **111**, 1132–1137 (2014).
- A. Bhaskar, M. Chawla, M. Mehta, P. Parikh, P. Chandra, D. Bhawe, D. Kumar, K. S. Carroll, A. Singh, Reengineering redox sensitive GFP to measure mycothiol redox potential of *Mycobacterium tuberculosis* during infection. *PLOS Pathog.* **10**, e1003902 (2014).
- M. J. Marakalala, F. O. Martinez, A. Plüddemann, S. Gordon, Macrophage heterogeneity in the immunopathogenesis of tuberculosis. *Front. Microbiol.* **9**, 1028 (2018).
- S. Helaine, J. A. Thompson, K. G. Watson, M. Liu, C. Boyle, D. W. Holden, Dynamics of intracellular bacterial replication at the single cell level. *Proc. Natl. Acad. Sci. U.S.A.* **107**, 3746–3751 (2010).
- S. Helaine, A. M. Cheverton, K. G. Watson, L. M. Faure, S. A. Matthews, D. W. Holden, Internalization of *Salmonella* by macrophages induces formation of nonreplicating persisters. *Science* **343**, 204–208 (2014).
- N. Q. Balaban, S. Helaine, K. Lewis, M. Ackermann, B. Aldridge, D. I. Andersson, M. P. Brynildsen, D. Bumann, A. Camilli, J. J. Collins, C. Dehio, S. Fortune, J.-M. Ghigo, W. D. Hardt, A. Harms, M. Heinemann, D. T. Hung, U. Jenal, B. R. Levin, J. Michiels, G. Storz, M.-W. Tan, T. Tenson, L. Van Melderen, A. Zinkernagel, Definitions and guidelines for research on antibiotic persistence. *Nat. Rev. Microbiol.* **17**, 441–448 (2019).
- K. H. Rohde, R. B. Abramovitch, D. G. Russell, *Mycobacterium tuberculosis* invasion of macrophages: Linking bacterial gene expression to environmental cues. *Cell Host Microbe* **2**, 352–364 (2007).
- J. A. Armstrong, P. D. Hart, Response of cultured macrophages to *Mycobacterium tuberculosis*, with observations on fusion of lysosomes with phagosomes. *J. Exp. Med.* **134**, 713–740 (1971).
- D. Wong, W. Li, J. D. Chao, P. Zhou, G. Narula, C. Tsui, M. Ko, J. Xie, C. Martinez-Frailes, Y. Av-Gay, Protein tyrosine kinase, PtkA, is required for *Mycobacterium tuberculosis* growth in macrophages. *Sci. Rep.* **8**, 155 (2018).
- M. Mehta, R. S. Rajmani, A. Singh, *Mycobacterium tuberculosis* *WhiB3* responds to vacuolar pH-induced changes in mycothiol redox potential to modulate phagosomal maturation and virulence. *J. Biol. Chem.* **291**, 2888–2903 (2016).
- D. Wong, H. Bach, J. Sun, Z. Hmama, Y. Av-Gay, *Mycobacterium tuberculosis* protein tyrosine phosphatase (PtpA) excludes host vacuolar-H⁺-ATPase to inhibit phagosome acidification. *Proc. Natl. Acad. Sci. U.S.A.* **108**, 19371–19376 (2011).
- C. J. Queval, O.-R. Song, J.-P. Carralot, J.-M. Saliou, A. Bongiovanni, G. Deloison, N. Deboosère, S. Jouny, R. Iantomasi, V. Delorme, A.-S. Debie, S.-J. Park, J. C. Gouveia, S. Tomaso, R. Brosch, A. Yoshimura, E. Yeramian, P. Brodin, *Mycobacterium tuberculosis* controls phagosomal acidification by targeting CISH-mediated signaling. *Cell Rep.* **20**, 3188–3198 (2017).
- T. M. Cunningham, J. L. Koehl, J. S. Summers, S. E. Haydel, pH-dependent metal ion toxicity influences the antibacterial activity of two natural mineral mixtures. *PLOS ONE* **5**, e9456 (2010).
- S. J. Stohs, D. Bagchi, Oxidative mechanisms in the toxicity of metal ions. *Free Radic. Biol. Med.* **18**, 321–336 (1995).
- M. Nandakumar, C. Nathan, K. Y. Rhee, Isocitrate lyase mediates broad antibiotic tolerance in *Mycobacterium tuberculosis*. *Nat. Commun.* **5**, 4306 (2014).
- E. Forte, V. B. Borisov, A. Davletshin, D. Mastronicola, P. Sarti, A. Giuffrè, Cytochrome *bd* oxidase and hydrogen peroxide resistance in *Mycobacterium tuberculosis*. *mBio* **4**, e01006-13 (2013).
- P. Lu, M. H. Heineke, A. Koul, K. Andries, G. M. Cook, H. Lill, R. van Spanning, D. Bald, The cytochrome *bd*-type quinol oxidase is important for survival of *Mycobacterium smegmatis* under peroxide and antibiotic-induced stress. *Sci. Rep.* **5**, 10333 (2015).
- J. C. Wilks, R. D. Kitko, S. H. Cleeton, G. E. Lee, C. S. Ugwu, B. D. Jones, S. S. BonDurant, J. L. Slonczewski, Acid and base stress and transcriptomic responses in *Bacillus subtilis*. *Appl. Environ. Microbiol.* **75**, 981–990 (2009).
- L. M. Maurer, E. Yohannes, S. S. BonDurant, M. Radmacher, J. L. Slonczewski, pH regulates genes for flagellar motility, catabolism, and oxidative stress in *Escherichia coli* K-12. *J. Bacteriol.* **187**, 304–319 (2004).
- O. H. Vandal, J. A. Roberts, T. Odaira, D. Schnappinger, C. F. Nathan, S. Ehrh, Acid-susceptible mutants of *Mycobacterium tuberculosis* share hypersusceptibility to cell wall and oxidative stress and to the host environment. *J. Bacteriol.* **191**, 625–631 (2009).
- G. L. Newton, N. Buchmeier, R. C. Fahey, Biosynthesis and functions of mycothiol, the unique protective thiol of *Actinobacteria*. *Microbiol. Mol. Biol. Rev.* **72**, 471–494 (2008).
- M. Berney, L. Berney-Meyer, K.-W. Wong, B. Chen, M. Chen, J. Kim, J. Wang, D. Harris, J. Parkhill, J. Chan, F. Wang, W. R. Jacobs Jr., Essential roles of methionine and S-adenosylmethionine in the autarkic lifestyle of *Mycobacterium tuberculosis*. *Proc. Natl. Acad. Sci. U.S.A.* **112**, 10008–10013 (2015).
- P. R. Wheeler, N. G. Coldham, L. Keating, S. V. Gordon, E. E. Wooff, T. Parish, R. G. Hewinson, Functional demonstration of reverse transsulfuration in the *Mycobacterium tuberculosis* complex reveals that methionine is the preferred sulfur source for pathogenic Mycobacteria. *J. Biol. Chem.* **280**, 8069–8078 (2005).
- K. Shatalin, E. Shatalina, A. Mironov, E. Nudler, H₂S: A universal defense against antibiotics in bacteria. *Science* **334**, 986–990 (2011).
- P. Shukla, V. S. Khodade, M. SharathChandra, P. Chauhan, S. Mishra, S. Siddaramappa, B. E. Pradeep, A. Singh, H. Chakrapani, "On demand" redox buffering by H₂S contributes to antibiotic resistance revealed by a bacteria-specific H₂S donor. *Chem. Sci.* **8**, 4967–4972 (2017).
- V. K. Pal, P. Bandyopadhyay, A. Singh, Hydrogen sulfide in physiology and pathogenesis of bacteria and viruses. *IUBMB Life* **70**, 393–410 (2018).
- M. A. Kohanski, D. J. Dwyer, B. Hayete, C. A. Lawrence, J. J. Collins, A common mechanism of cellular death induced by bactericidal antibiotics. *Cell* **130**, 797–810 (2007).
- D. Willemse, B. Weber, L. Masino, R. M. Warren, S. Adinolfi, A. Pastore, M. J. Williams, Rv1460, a SufR homologue, is a repressor of the suf operon in *Mycobacterium tuberculosis*. *PLOS ONE* **13**, e0200145 (2018).
- G. Huet, M. Daffé, I. Saves, Identification of the *Mycobacterium tuberculosis* Suf machinery as the exclusive mycobacterial system of [Fe-S] cluster assembly: Evidence for its implication in the pathogen's survival. *J. Bacteriol.* **187**, 6137–6146 (2005).
- T. Warrior, K. Kapilashrami, A. Argyrou, T. R. Ioeberger, D. Little, K. C. Murphy, M. Nandakumar, S. Park, B. Gold, J. Mi, T. Zhang, E. Meiler, M. Rees, S. Somersan-Karakaya, E. P. DeFrancisco, M. Martinez-Hoyos, K. Burns-Huang, J. Roberts, Y. Ling, K. Y. Rhee, A. Mendoza-Losana, M. Luo, C. F. Nathan, N-methylation of a bactericidal compound as a resistance mechanism in *Mycobacterium tuberculosis*. *Proc. Natl. Acad. Sci. U.S.A.* **113**, E4523–E4530 (2016).

41. P. Sukheja, P. Kumar, N. Mittal, S.-G. Li, E. Singleton, R. Russo, A. L. Perryman, R. Shrestha, D. Awasthi, S. Husain, P. Soteropoulos, R. Brukh, N. Connell, J. S. Freundlich, D. Alland, A novel small-molecule inhibitor of the *Mycobacterium tuberculosis* demethylmenaquinone methyltransferase MenG is bactericidal to both growing and nutritionally deprived persister cells. *MBio* **8**, e02022-16 (2017).
42. P. Golby, J. Nunez, P. J. Cockle, K. Ewer, K. Logan, P. Hogarth, H. M. Vordermeier, J. Hinds, R. G. Hewinson, S. V. Gordon, Characterization of two *in vivo*-expressed methyltransferases of the *Mycobacterium tuberculosis* complex: Antigenicity and genetic regulation. *Microbiology* **154**, 1059–1067 (2008).
43. L. Rodrigues, C. Vilellas, R. Bailo, M. Viveiros, J. A. Ainsa, Role of the Mmr efflux pump in drug resistance in *Mycobacterium tuberculosis*. *Antimicrob. Agents Chemother.* **57**, 751–757 (2013).
44. G. Li, J. Zhang, Q. Guo, Y. Jiang, J. Wei, L. Zhao, X. Zhao, J. Lu, K. Wan, Efflux pump gene expression in multidrug-resistant *Mycobacterium tuberculosis* clinical isolates. *PLOS ONE* **10**, e0119013 (2015).
45. B. Ezraty, A. Vergnes, M. Banzhaf, Y. Duverger, A. Huguenot, A. R. Brochado, S.-Y. Su, L. Espinosa, L. Loiseau, B. Py, A. Typas, F. Barras, Fe-S cluster biosynthesis controls uptake of aminoglycosides in a ROS-less death pathway. *Science* **340**, 1583–1587 (2013).
46. S. Nambi, J. E. Long, B. B. Mishra, R. Baker, K. C. Murphy, A. J. Olive, H. P. Nguyen, S. A. Shaffer, C. M. Sasseti, The oxidative stress network of *Mycobacterium tuberculosis* reveals coordination between radical detoxification systems. *Cell Host Microbe* **17**, 829–837 (2015).
47. J. Burian, S. Ramón-García, G. Sweet, A. Gomez-Velasco, Y. Av-Gay, C. J. Thompson, The mycobacterial transcriptional regulator *whiB7* gene links redox homeostasis and intrinsic antibiotic resistance. *J. Biol. Chem.* **287**, 299–310 (2012).
48. J. Zhang, Q. Zhang, Using Seahorse machine to measure OCR and ECAR in cancer cells. *Methods Mol. Biol.* **1928**, 353–363 (2019).
49. P. D. Hart, M. R. Young, Ammonium chloride, an inhibitor of phagosome-lysosome fusion in macrophages, concurrently induces phagosome-endosome fusion, and opens a novel pathway: Studies of a pathogenic mycobacterium and a nonpathogenic yeast. *J. Exp. Med.* **174**, 881–889 (1991).
50. M. G. Rittig, M.-T. Alvarez-Martinez, F. Porte, J.-P. Liautard, B. Rouot, Intracellular survival of *Brucella* spp. in human monocytes involves conventional uptake but special phagosomes. *Infect. Immun.* **69**, 3995–4006 (2001).
51. U. Matt, P. Selchow, M. Dal Molin, S. Strommer, O. Sharif, K. Schilcher, F. Andreoni, A. Stenzinger, A. S. Zinkernagel, M. Zeitlinger, P. Sander, J. Nemeth, Chloroquine enhances the antimycobacterial activity of isoniazid and pyrazinamide by reversing inflammation-induced macrophage efflux. *Int. J. Antimicrob. Agents* **50**, 55–62 (2017).
52. H. C. Mwandumba, D. G. Russell, M. H. Nyirenda, J. Anderson, S. A. White, M. E. Molyneux, S. B. Squire, *Mycobacterium tuberculosis* resides in nonacidified vacuoles in endocytically competent alveolar macrophages from patients with tuberculosis and HIV infection. *J. Immunol.* **172**, 4592–4598 (2004).
53. S. A. Ali, T. R. Mavundla, R. Fantu, T. Awoke, Outcomes of TB treatment in HIV co-infected TB patients in Ethiopia: A cross-sectional analytic study. *BMC Infect. Dis.* **16**, 640 (2016).
54. A. Bhaskar, M. H. Munshi, S. Z. Khan, S. Fatima, R. Arya, S. Jameel, A. Singh, Measuring glutathione redox potential of HIV-1-infected macrophages. *J. Biol. Chem.* **290**, 1020–1038 (2015).
55. T. M. Folks, J. Justement, A. Kinter, C. A. Dinarello, A. S. Fauci, Cytokine-induced expression of HIV-1 in a chronically infected promonocyte cell line. *Science* **238**, 800–802 (1987).
56. G. Poli, A. Kinter, J. S. Justement, J. H. Kehrl, P. Bressler, S. Stanley, A. S. Fauci, Tumor necrosis factor alpha functions in an autocrine manner in the induction of human immunodeficiency virus expression. *Proc. Natl. Acad. Sci. U.S.A.* **87**, 782–785 (1990).
57. N. R. Cohen, M. A. Lobritz, J. J. Collins, Microbial persistence and the road to drug resistance. *Cell Host Microbe* **13**, 632–642 (2013).
58. W. P. Gill, N. S. Harik, M. R. Whiddon, R. P. Liao, J. E. Mittler, D. R. Sherman, A replication clock for *Mycobacterium tuberculosis*. *Nat. Med.* **15**, 211–214 (2009).
59. C. E. Kramer, A. Singh, S. Helfrich, A. Grunberger, W. Wiechert, K. Noh, D. Kohlheyer, Non-invasive microbial metabolic activity sensing at single cell level by perfusion of calcein acetoxymethyl ester. *PLOS ONE* **10**, e0141768 (2015).
60. J. E. M. de Steenwinkel, G. J. deKnegt, M. T. Ten Kate, A. van Belkum, H. A. Verbrugh, K. Kremer, D. van Soolingen, I. A. J. M. Bakker-Woudenberg, Time-kill kinetics of anti-tuberculosis drugs, and emergence of resistance, in relation to metabolic activity of *Mycobacterium tuberculosis*. *J. Antimicrob. Chemother.* **65**, 2582–2589 (2010).
61. O. Danilchanka, C. Mailaender, M. Niederweis, Identification of a novel multidrug efflux pump of *Mycobacterium tuberculosis*. *Antimicrob. Agents Chemother.* **52**, 2503–2511 (2008).
62. A. Farhana, S. Kumar, S. S. Rathore, P. C. Ghosh, N. Z. Ehtesham, A. K. Tyagi, S. E. Hasnain, Mechanistic insights into a novel exporter-importer system of *Mycobacterium tuberculosis* unravel its role in trafficking of iron. *PLOS ONE* **3**, e2087 (2008).
63. E. De Rossi, M. Branzoni, R. Cantoni, A. Milano, G. Riccardi, O. Ciferri, *mmr*, a *Mycobacterium tuberculosis* gene conferring resistance to small cationic dyes and inhibitors. *J. Bacteriol.* **180**, 6068–6071 (1998).
64. F. A. Wolschendorf, D. Ackart, T. B. Shrestha, L. Hascall-Dove, S. Nolan, G. Lamichhane, Y. Wang, S. H. Bossmann, R. J. Basaraba, M. Niederweis, Copper resistance is essential for virulence in *Mycobacterium tuberculosis*. *Proc. Natl. Acad. Sci. U.S.A.* **108**, 1621–1626 (2011).
65. M. Chawla, S. Mishra, K. Anand, P. Parikh, M. Mehta, M. Vij, T. Verma, P. Singh, K. Jakkala, H. N. Verma, P. Ajitkumar, M. Ganguli, A. S. N. Seshasayee, A. Singh, Redox-dependent condensation of the mycobacterial nucleoid by WhiB4. *Redox Biol.* **19**, 116–133 (2018).
66. P. D. Hart, M. R. Young, A. H. Gordon, K. H. Sullivan, Inhibition of phagosome-lysosome fusion in macrophages by certain mycobacteria can be explained by inhibition of lysosomal movements observed after phagocytosis. *J. Exp. Med.* **166**, 933–946 (1987).
67. B. Poole, S. Ohkuma, Effect of weak bases on the intralysosomal pH in mouse peritoneal macrophages. *J. Cell Biol.* **90**, 665–669 (1981).
68. N. Dhar, J. D. McKinney, *Mycobacterium tuberculosis* persistence mutants identified by screening in isoniazid-treated mice. *Proc. Natl. Acad. Sci. U.S.A.* **107**, 12275–12280 (2010).
69. L. E. Via, P. L. Lin, S. M. Ray, J. Carrillo, S. S. Allen, S. Y. Eum, K. Taylor, E. Klein, U. Manjunatha, J. Gonzales, E. G. Lee, S. K. Park, J. A. Raleigh, S. N. Cho, D. N. McMurray, J. L. Flynn, C. E. Barry III, Tuberculous granulomas are hypoxic in guinea pigs, rabbits, and nonhuman primates. *Infect. Immun.* **76**, 2333–2340 (2008).
70. A. J. Crowle, M. H. May, Inhibition of tubercle bacilli in cultured human macrophages by chloroquine used alone and in combination with streptomycin, isoniazid, pyrazinamide, and two metabolites of vitamin D3. *Antimicrob. Agents Chemother.* **34**, 2217–2222 (1990).
71. A. Ganguli, D. Choudhury, S. Datta, S. Bhattacharya, G. Chakrabarti, Inhibition of autophagy by chloroquine potentiates synergistically anti-cancer property of artemisinin by promoting ROS dependent apoptosis. *Biochimie* **107 Pt B**, 338–349 (2014).
72. J. Lee, T. Repasy, K. Papavinasasundaram, C. Sasseti, H. Kornfeld, *Mycobacterium tuberculosis* induces an atypical cell death mode to escape from infected macrophages. *PLOS ONE* **6**, e18367 (2011).
73. S. Levitte, K. N. Adams, R. D. Berg, C. L. Cosma, K. B. Urdahl, L. Ramakrishnan, Mycobacterial acid tolerance enables phagolysosomal survival and establishment of tuberculous infection *in vivo*. *Cell Host Microbe* **20**, 250–258 (2016).
74. L. L. Gustafsson, O. Walker, G. Alvan, B. Beermann, F. Estevez, L. Gleisner, B. Lindstrom, F. Sjöqvist, Disposition of chloroquine in man after single intravenous and oral doses. *Br. J. Clin. Pharmacol.* **15**, 471–479 (1983).
75. S. C. Chow, Bioavailability and bioequivalence in drug development. *Wiley Interdiscip. Rev. Comput. Stat.* **6**, 304–312 (2014).
76. J. O. Nwankwo, M. A. Garba, C. E. Chinje, L. O. Mgbokikwe, G. O. Emerole, Possible chloroquine-induced modification of N-acetylation of isoniazid and sulphadimidine in the rat. *Biochem. Pharmacol.* **40**, 654–659 (1990).
77. M. Akira, M. Sakatani, H. Ishikawa, Transient radiographic progression during initial treatment of pulmonary tuberculosis: CT findings. *J. Comput. Assist. Tomogr.* **24**, 426–431 (2000).
78. A. Jindani, C. J. Dore, D. A. Mitchison, Bactericidal and sterilizing activities of antituberculosis drugs during the first 14 days. *Am. J. Respir. Crit. Care Med.* **167**, 1348–1354 (2003).
79. J. J. Kim, H. M. Lee, D. M. Shin, W. Kim, J. M. Yuk, H. S. Jin, S. H. Lee, G. H. Cha, J. M. Kim, Z. W. Lee, S. J. Shin, H. Yoo, Y. K. Park, J. B. Park, J. Chung, T. Yoshimori, E. K. Jo, Host cell autophagy activated by antibiotics is required for their effective antimycobacterial drug action. *Cell Host Microbe* **11**, 457–468 (2012).
80. G. B. Coulson, B. K. Johnson, H. Zheng, C. J. Colvin, R. Fillinger, E. R. Haiderer, N. D. Hammer, R. B. Abramovitch, Targeting *Mycobacterium tuberculosis* sensitivity to thiol stress at acidic pH kills the bacterium and potentiates antibiotics. *Cell Chem. Biol.* **24**, 993–1004.e4 (2017).
81. J. Vaubourgeix, G. Lin, N. Dhar, N. Chenouard, X. Jiang, H. Botella, T. Lupoli, O. Mariani, G. Yang, O. Ouerfelli, M. Unser, D. Schnappinger, J. D. McKinney, C. F. Nathan, Stressed mycobacteria use the chaperone ClpB to sequester irreversibly oxidized proteins asymmetrically within and between cells. *Cell Host Microbe* **17**, 178–190 (2015).
82. O. H. Vandal, L. M. Pierini, D. Schnappinger, C. F. Nathan, S. Ehrt, A membrane protein preserves intrabacterial pH in intraphagosomal *Mycobacterium tuberculosis*. *Nat. Med.* **14**, 849–854 (2008).
83. J. J. Baker, B. K. Johnson, R. B. Abramovitch, Slow growth of *Mycobacterium tuberculosis* at acidic pH is regulated by *phoPR* and host-associated carbon sources. *Mol. Microbiol.* **94**, 56–69 (2014).
84. N. A. Burton, N. Schurmann, O. Casse, A. K. Steeb, B. Claudi, J. Zankl, A. Schmidt, D. Burmann, Disparate impact of oxidative host defenses determines the fate of *Salmonella* during systemic infection in mice. *Cell Host Microbe* **15**, 72–83 (2014).
85. K. Avican, A. Fahlgren, M. Huss, A. K. Heroven, M. Beckstette, P. Dersch, M. Fallman, Reprogramming of *Yersinia* from virulent to persistent mode revealed by complex *in vivo* RNA-seq analysis. *PLOS Pathog.* **11**, e1004600 (2015).
86. C. Vilcheze, T. Hartman, B. Weinrick, P. Jain, T. R. Weisbrod, L. W. Leung, J. S. Freundlich, W. R. Jacobs Jr., Enhanced respiration prevents drug tolerance and drug resistance in *Mycobacterium tuberculosis*. *Proc. Natl. Acad. Sci. U.S.A.* **114**, 4495–4500 (2017).

87. W. P. Tsai, P. L. Nara, H. F. Kung, S. Oroszlan, Inhibition of human immunodeficiency virus infectivity by chloroquine. *AIDS Res. Hum. Retroviruses* **6**, 481–489 (1990).
88. D. Martins, G. McKay, G. Sampathkumar, M. Khakimova, A. M. English, D. Nguyen, Superoxide dismutase activity confers (p)ppGpp-mediated antibiotic tolerance to stationary-phase *Pseudomonas aeruginosa*. *Proc. Natl. Acad. Sci. U.S.A.* **115**, 9797–9802 (2018).
89. R. M. McCune Jr., R. Tompsett, Fate of *Mycobacterium tuberculosis* in mouse tissues as determined by the microbial enumeration technique. I. The persistence of drug-susceptible tubercle bacilli in the tissues despite prolonged antimicrobial therapy. *J. Exp. Med.* **104**, 737–762 (1956).
90. K. McAulay, K. Saito, T. Warrier, K. F. Walsh, L. D. Mathurin, G. Royal-Mardi, M. H. Lee, O. Ocheretina, J. W. Pape, D. W. Fitzgerald, C. F. Nathan, Differentially detectable *Mycobacterium tuberculosis* cells in sputum from treatment-naïve subjects in Haitian and their proportionate increase after initiation of treatment. *MBio* **9**, e02192-18 (2018).
91. R. Jain, B. Dey, N. Dhar, V. Rao, R. Singh, U. D. Gupta, V. M. Katoch, V. D. Ramanathan, A. K. Tyagi, Enhanced and enduring protection against tuberculosis by recombinant BCG-Ag85C and its association with modulation of cytokine profile in lung. *PLOS ONE* **3**, e3869 (2008).
92. Z. Ahmad, L. G. Klinkenberg, M. L. Pinn, M. M. Fraig, C. A. Peloquin, W. R. Bishai, E. L. Nuermberger, J. H. Grosset, P. C. Karakousis, Biphasic kill curve of isoniazid reveals the presence of drug-tolerant, not drug-resistant, *Mycobacterium tuberculosis* in the guinea pig. *J. Infect. Dis.* **200**, 1136–1143 (2009).
93. K. Glass, M. Girvan, Annotation enrichment analysis: An alternative method for evaluating the functional properties of gene sets. *Sci. Rep.* **4**, 4191 (2014).
94. D. S. Ghorpade, S. Holla, S. V. Kaveri, J. Bayry, S. A. Patil, K. N. Balaji, Sonic hedgehog-dependent induction of microRNA 31 and microRNA 150 regulates *Mycobacterium bovis* BCG-driven toll-like receptor 2 signaling. *Mol. Cell. Biol.* **33**, 543–556 (2013).
95. M. L. Arcila, M. D. Sánchez, B. Ortiz, L. F. Barrera, L. F. Garcia, M. Rojas, Activation of apoptosis, but not necrosis, during *Mycobacterium tuberculosis* infection correlated with decreased bacterial growth: Role of TNF- α , IL-10, caspases and phospholipase A2. *Cell. Immunol.* **249**, 80–93 (2007).
96. M. Chawla, P. Parikh, A. Saxena, M. H. Munshi, M. Mehta, D. Mai, A. K. Srivastava, K. V. Narasimulu, K. E. Redding, N. Vashi, D. Kumar, A. J. Steyn, A. Singh, *Mycobacterium tuberculosis* WhiB4 regulates oxidative stress response to modulate survival and dissemination in vivo. *Mol. Microbiol.* **85**, 1148–1165 (2012).
97. H. Li, R. Durbin, Fast and accurate short read alignment with Burrows-Wheeler transform. *Bioinformatics* **25**, 1754–1760 (2009).
98. H. Li, B. Handsaker, A. Wysoker, T. Fennell, J. Ruan, N. Homer, G. Marth, G. Abecasis, R. Durbin; 1000 Genome Project Data Processing Subgroup, The Sequence Alignment/Map format and SAMtools. *Bioinformatics* **25**, 2078–2079 (2009).
99. A. R. Quinlan, I. M. Hall, BEDTools: A flexible suite of utilities for comparing genomic features. *Bioinformatics* **26**, 841–842 (2010).
100. M. I. Love, W. Huber, S. Anders, Moderated estimation of fold change and dispersion for RNA-seq data with DESeq2. *Genome Biol.* **15**, 550 (2014).
101. R. Colangeli, D. Helb, S. Sridharan, J. Sun, M. Varma-Basil, M. H. Hazbon, R. Harbacheuski, N. J. Megjugorac, W. R. Jacobs Jr., A. Holzenburg, J. Sacchettini, D. Alland, The *Mycobacterium tuberculosis* *iniA* gene is essential for activity of an efflux pump that confers drug tolerance to both isoniazid and ethambutol. *Mol. Microbiol.* **55**, 1829–1840 (2005).
102. S. Andrews, FastQC: A quality control tool for highthroughput sequence data (2010); www.bioinformatics.babraham.ac.uk/projects/fastqc.
103. RStudio Team, RStudio: Integrated development for R. RStudio, Inc., Boston, MA (2015); www.rstudio.com/.
104. A. Basic, S. Blomqvist, A. Carlen, G. Dahlén, Estimation of bacterial hydrogen sulfide production in vitro. *J. Oral Microbiol.* **7**, 28166 (2015).
105. D. A. Lamprecht, P. M. Finin, M. A. Rahman, B. M. Cummin, S. L. Russell, S. R. Jonnal, J. H. Adamson, A. J. C. S. Steyn, Turning the respiratory flexibility of *Mycobacterium tuberculosis* against itself. *Nat. Commun.* **7**, 12393 (2016).
106. S. Mishra, P. Shukla, A. Bhaskar, K. Anand, P. Baloni, R. K. Jha, A. Mohan, R. S. Rajmani, V. Nagaraja, N. Chandra, A. Singh, Efficacy of b-lactam/b-lactamase inhibitor combination is linked to WhiB4-mediated changes in redox physiology of *Mycobacterium tuberculosis*. *eLife* **6**, e25624 (2017).
107. C. L. Hendon-Dunn, K. S. Doris, S. R. Thomas, J. C. Allnutt, A. A. N. Marriott, K. A. Hatch, R. J. Watson, G. Bottley, P. D. Marsh, S. C. Taylor, J. Bacon, A flow cytometry method for rapidly assessing *Mycobacterium tuberculosis* responses to antibiotics with different modes of action. *Antimicrob. Agents Chemother.* **60**, 3869–3883 (2016).
108. M. Jungblut, K. Oeltze, I. Zehnter, D. Hasselmann, A. Bosio, Standardized preparation of single-cell suspensions from mouse lung tissue using the gentleMACS Dissociator. *J. Vis. Exp.* **29**, 1266 (2009).
109. S. Chakarav, H. Y. Lim, L. Tan, S. Y. Lim, P. See, J. Lum, X.-M. Zhang, S. Foo, S. Nakamizo, K. Duan, W. T. Kong, R. Gentek, A. Balachander, D. Carbajo, C. Blierot, B. Malleret, J. K. C. Tam, S. Baig, M. Shabeer, S.-E. S. Toh, A. Schlitzer, A. Larbi, T. Marichal, B. Malissen, J. Chen, M. Poidinger, K. Kabashima, M. Bajenoff, L. G. Ng, V. Angeli, F. Ginhoux, Two distinct interstitial macrophage populations coexist across tissues in specific subcellular niches. *Science* **363**, eaau0964 (2019).
110. J. Grosset, C. Truffot-Pernot, C. Lacroix, B. Ji, Antagonism between isoniazid and the combination pyrazinamide-rifampin against tuberculosis infection in mice. *Antimicrob. Agents Chemother.* **36**, 548–551 (1992).
111. N. K. Dutta, M. L. Pinn, P. C. Karakousis, Reduced emergence of isoniazid resistance with concurrent use of thioridazine against acute murine tuberculosis. *Antimicrob. Agents Chemother.* **58**, 4048–4053 (2014).
112. R. B. Abramovitch, K. H. Rohde, F.-F. Hsu, D. G. Russell, *apraABC*: A *Mycobacterium tuberculosis* complex-specific locus that modulates pH-driven adaptation to the macrophage phagosome. *Mol. Microbiol.* **80**, 678–694 (2011).

Acknowledgments: We are grateful to C. Grundner at the Seattle Children's Research Institute for critical reading of the manuscript and valuable input. We acknowledge W. R. Jacobs Jr. at the Albert Einstein College of Medicine for the *Mtb mshA* mutant and D. J. V. Beste at the University of Surrey for providing the zeocin-marked vector pANEE001. C. N. Naveen at the Foundation of Neglected Disease Research (FNDR), India is acknowledged for supporting pharmacokinetic and drug-drug interaction studies in mice. We thank S. Nayak for valuable discussions about the key findings of the study and designing of schematics and models. We acknowledge the CIDR BSL-3 facility, Indian Institute of Science (IISc) for carrying out experiments with *Mtb* and A. Pandit and the NGS facility, NCBS for RNA-seq. The *mshA* mutant of *Mtb* was obtained from W. R. Jacobs Jr. under a material transfer agreement (MTA) between the Albert Einstein College of Medicine of Yeshiva University and the International Centre for Genetic Engineering and Biotechnology. **Funding:** This work was supported by Wellcome Trust–DBT India Alliance grant IAS/16/2/502700 (to A.S.); in part, by Department of Biotechnology (DBT) grants BT/PR11911/BRB/10/1327/2014 and BT/PR13522/COE/34/27/2015 (to A.S.); and by the DBT-IISc Partnership Program (22-0905-0006-05-987436). A.S. is a senior fellow of Wellcome Trust–DBT India Alliance. A.S.N.S. is supported by the Wellcome Trust–DBT India Alliance Grant IA/16/2/5-2711. R.M. is supported by the IISc, Bengaluru. S.K. and

M. Mehta are national postdoctoral fellows supported by the Department of Science and Technology (DST), India. N.M. is supported by the National Centre for Biological Sciences—Tata Institute of Fundamental Research (NCBS-TIFR), Bengaluru. P.B. is supported by a fellowship provided by the Council of Scientific and Industrial Research (CSIR), India. **Author contributions:** R.M. and A.S. conceptualized the research and prepared the manuscript. R.M. and S.K. performed the experiments and analyzed data. N.M. and A.S.N.S. conducted the RNA-seq analysis. P.B., M. Mehta, and M. Munshi constructed the knockout and complemented strains and conducted the HIV- TB coinfection and H₂S measurement assays. V.A. performed the flow sorting. V.K.A. and R.K.S. conducted the pharmacokinetic drug-drug interaction studies. R.S.R. conducted animal experiments. **Competing interests:** The authors declare that they have no competing interests. **Data and materials availability:** All data associated with this study are present in the paper or the Supplementary Materials. RNA-seq data generated and analyzed in this study have been uploaded to the NCBI Gene Expression Omnibus under accession number GSE123267.

Submitted 15 January 2019
Resubmitted 26 June 2019
Accepted 25 October 2019
Published 13 November 2019
10.1126/scitranslmed.aaw6635

Citation: R. Mishra, S. Kohli, N. Malhotra, P. Bandyopadhyay, M. Mehta, M. Munshi, V. Adiga, V. K. Ahuja, R. K. Shandil, R. S. Rajmani, A. S. N. Seshasayee, A. Singh, Targeting redox heterogeneity to counteract drug tolerance in replicating *Mycobacterium tuberculosis*. *Sci. Transl. Med.* **11**, eaaw6635 (2019).

Targeting redox heterogeneity to counteract drug tolerance in replicating *Mycobacterium tuberculosis*

Richa Mishra, Sakshi Kohli, Nitish Malhotra, Parijat Bandyopadhyay, Mansi Mehta, MohamedHusen Munshi, Vasista Adiga, Vijay Kamal Ahuja, Radha K. Shandil, Raju S. Rajmani, Aswin Sai Narain Seshasayee and Amit Singh

Sci Transl Med 11, eaaw6635.

DOI: 10.1126/scitranslmed.aaw6635

Antibiotic redox-based redux

Phagosomal pH and redox heterogeneity in *Mycobacterium tuberculosis* (*Mtb*) can promote tolerance of the bacterium to antibiotics. Mishra *et al.* found that the approved antimalarial drug chloroquine inhibited this acidification and resulted in altered redox metabolism and improved susceptibility of *Mtb* to first-line antituberculosis drugs, particularly isoniazid, in infected macrophages in vitro. Coadministration of chloroquine improved isoniazid treatment outcomes in both mouse and guinea pig models of *Mtb* infection. This work suggests the repurposing of chloroquine to potentiate and possibly shorten antibiotic treatment of tuberculosis.

ARTICLE TOOLS

<http://stm.sciencemag.org/content/11/518/eaaw6635>

SUPPLEMENTARY MATERIALS

<http://stm.sciencemag.org/content/suppl/2019/11/11/11.518.eaaw6635.DC1>

RELATED CONTENT

<http://stm.sciencemag.org/content/scitransmed/11/483/eaau6267.full>
<http://stm.sciencemag.org/content/scitransmed/10/435/eaai7786.full>
<http://stm.sciencemag.org/content/scitransmed/10/438/eaal1803.full>

<http://science.sciencemag.org/content/sci/367/6482/1147.full>

REFERENCES

This article cites 110 articles, 48 of which you can access for free

<http://stm.sciencemag.org/content/11/518/eaaw6635#BIBL>

PERMISSIONS

<http://www.sciencemag.org/help/reprints-and-permissions>

Use of this article is subject to the [Terms of Service](#)

Science Translational Medicine (ISSN 1946-6242) is published by the American Association for the Advancement of Science, 1200 New York Avenue NW, Washington, DC 20005. The title *Science Translational Medicine* is a registered trademark of AAAS.

Copyright © 2019 The Authors, some rights reserved; exclusive licensee American Association for the Advancement of Science. No claim to original U.S. Government Works

MICROBIOLOGY

S-Adenosylmethionine–responsive cystathionine b-synthase modulates sulfur metabolism and redox balance in *Mycobacterium tuberculosis*

Parijat Bandyopadhyay^{1,2†}, Ishika Pramanick^{3†}, Rupam Biswas³, Sabarinath PS⁴, Sreesa Sreedharan⁴, Shalini Singh^{1,2}, Raju S. Rajmani², Sunil Laxman⁴, Somnath Dutta^{3*}, Amit Singh^{1,2*}

Methionine and cysteine metabolisms are important for the survival and pathogenesis of *Mycobacterium tuberculosis* (*Mtb*). The transsulfuration pathway converts methionine to cysteine and represents an important link between antioxidant and methylation metabolism in diverse organisms. Using a combination of biochemistry and cryo– electron microscopy, we characterized the first enzyme of the transsulfuration pathway, cystathionine b-synthase (*Mtb*Cbs) in *Mtb*. We demonstrated that *Mtb*Cbs is a heme-less, pyridoxal-5'-phosphate–containing enzyme, alloster-ically activated by S-adenosylmethionine (SAM). The atomic model of *Mtb*Cbs in its native and SAM-bound confor-mations revealed a unique mode of SAM-dependent allosteric activation. Further, SAM stabilized *Mtb*Cbs by sterically occluding proteasomal degradation, which was crucial for supporting methionine and redox metabolism in *Mtb*. Genetic deficiency of *Mtb*Cbs reduced *Mtb* survival upon homocysteine overload in vitro, inside macro-phages, and in mice coinfectd with HIV. Thus, the *Mtb*Cbs-SAM axis constitutes an important mechanism of coordinating sulfur metabolism in *Mtb*.

INTRODUCTION

Mycobacterium tuberculosis (*Mtb*) multiplies, establishes infection, and maintains a state of chronic persistence within the human host (1). Moreover, *Mtb* can reinstate growth after long-term persistence, enabling transmission to a new host and perpetuation of infection (2). Studies indicate that the flexibility of metabolic functions limits *Mtb*'s dependence on host metabolites and facilitates survival in the face of host immunity and drug pressures (3, 4). *Mtb* carries out de novo biosynthesis of all essential cofactors and amino acids (5). Strains auxotrophic for amino acids are among the most attenuated in vivo (6–8) and have showed remarkable vaccine potential (9–11). Therefore, molecular dissection of *Mtb*'s metabolic flexibility is im-perative to understand the basis of its success as a human pathogen.

In this context, the metabolism of sulfur (S)–containing amino acids cysteine (Cys) and methionine (Met) is markedly important in *Mtb*'s pathophysiology. Cys functions as a central regulator of redox homeostasis by synthesizing the major mycobacterial anti-oxidant buffer, mycothiol (12). In addition, Cys-derived S is mobilized to generate (Fe-S) clusters (13, 14), sulfolipids (SL-1) (15), and hydrogen sulfide (H₂S) (16), crucial for respiration and persistence of *Mtb*, and to tolerate antibiotics (17–20). Similarly, Met, via the active methyl cycle (AMC), generates the ubiquitous methyl donor, S-adenosylmethionine (SAM), which is essential for the biosynthesis of mycolic acids, menaquinone, and biotin (21–23). Abrogation of Met biosynthesis in *Mtb* diminishes SAM levels, inhibits methyla-tion and one-carbon metabolism, and leads to hyperattenuation in mice (7).

In higher eukaryotes such as humans, the metabolism of these two sulfur-containing amino acids is linked to cater to cellular anti-oxidant and methylation demands (24). Met is an essential amino acid and is acquired from the diet, which, in turn, is converted to Cys via the reverse transsulfuration (RTS) pathway. The first and rate-limiting enzyme of the pathway, cystathionine b-synthase (CBS; E.C: 4.2.1.22), a pyridoxal-5 - phosphate (PLP) containing heme protein, condenses serine (Ser) and homocysteine (Hcys), an inter-mediate of the AMC, to form cystathionine (Cysth). Cysth is subse-quently cleaved by cystathionine (Cysth) g-lyase (CGS; E.C: 4.4.1.1) to yield Cys, which is a precursor of the major cellular antioxidant, glutathione (25). Hcys functions as a branch-point metabolite that can either enter the RTS pathway to form Cys during Met suffi-ciency or get remethylated to form Met and SAM via AMC upon Met defi-ciency. Hcys partitioning is dependent on CBS and the cel-lular abundance of its allosteric activator SAM (26). Therefore, CBS and SAM in tandem adjust the balance between conserving Met via AMC or committing it to generate antioxidants by RTS to achieve coordinated changes in methylation status or redox potential of the cell, respectively (27). In addition, the RTS pathway is also the principal source of the gasotransmitter H₂S, which has emerged as a major gaseous cellular signaling molecule with cytoprotective effects (28).

In contrast to mammals, the biosyntheses of Cys and Met are un-linked and occur de novo in *Mtb* using sulfide (S²⁻) as the S source derived from the reductive sulfate assimilation pathway (29). Genetic and pharmacological studies have implicated the reductive S metabo-lism in redox homeostasis, persistence, and pathogenesis of *Mtb* (12, 18, 30). Contrary to the reductive arm of S metabolism, the role of RTS pathway in the physiology and pathogenesis of *Mtb* has remained poorly characterized. Therefore, the mechanistic dissection of the functional role of the RTS pathway of *Mtb* is important. Of interest to us is the underlying mechanism(s) that metabolically links RTS pathway with the AMC for maintaining cellular homeostasis in *Mtb*.

In this study, we have characterized the first enzyme of the RTS pathway of *Mtb*, CBS (*Mtb*Cbs) using a range of biochemical, structural

¹Department of Microbiology and Cell Biology, Indian Institute of Science, Bangalore, Karnataka 560012, India. ²Centre for Infectious Disease Research, Indian Institute of Science, Bangalore, Karnataka 560012, India. ³Molecular Biophysics Unit, Indian Institute of Science, Bangalore, Karnataka 560012, India. ⁴Institute for Stem Cell Science and Regenerative Medicine, Bangalore, Karnataka 560065, India. *Corresponding author. Email: asingh@iisc.ac.in (A.S.); somnath@iisc.ac.in

(S.D.) †These authors contributed equally to this work.

[cryo-electron microscopy (cryo-EM)], and genetic approaches. We uncovered a regulatory mechanism by which *Mtb*Cbs is allosterically activated by SAM. A reduction in SAM levels led to destabilization of *Mtb*Cbs posttranslationally, which promoted metabolic switching of the Cys biosynthetic RTS pathway to the Met biosynthetic forward transsulfuration (FTS) pathway. Inhibition of this switching per-turbed redox homeostasis and compromised *Mtb*'s survival. Further, genetic disruption of *Mtb*Cbs perturbed survival of *Mtb* in response to Hcys overload in vitro. We showed that under a clinically relevant pathological condition with increased Hcys levels i.e., HIV– tuberculosis (TB) coinfection, *Mtb*Cbs is crucial for the survival of *Mtb*. Our findings establish *Mtb*Cbs as a novel regulatory node in the sulfur metabolism of *Mtb*.

RESULTS

***Mtb*Cbs contains PLP and is allosterically activated by SAM** The *Mtb* H37Rv genome encodes a putative CBS (Rv1077, *Mtb*Cbs) (<https://mycobrowser.epfl.ch/>) belonging to the type II-fold PLP-containing protein family. In contrast to reported bacterial CBSs (31), Pfam (protein family database) analysis revealed the presence of the SAM binding Bateman module in *Mtb*Cbs. Purified *Mtb*Cbs eluted as a tetramer based on size exclusion chromatography (SEC) and SEC–multiangle light scattering (SEC-MALS) (fig. S1, A to C). The purified *Mtb*Cbs was yellow in color and exhibited an ultraviolet-visible (UV-VIS) absorption peak at 412 nm, which is characteristic

of the protonated internal aldimine form of PLP. The peak at 412 nm was abrogated when the PLP-coordinating active site lysine (K44) was mutated to alanine (K44A) (fig. S1D). *Mtb*Cbs did not exhibit heme-associated Soret peak in the UV-VIS spectrum, and the pyridine hemochromagen assay further confirmed that the protein is heme-less (fig. S1, E to G).

The CBS enzyme from diverse organisms uses multiple substrates to generate Cysth, lanthionine (Lnth), Ser, and H₂S (table S1) (32). Using acid-ninhydrin assay, we found that *Mtb*Cbs generated Cysth from Ser + Hcys, but not from O-acetylserine + Hcys as substrates (fig. S1H) (33). Further, lead-acetate assay confirmed that *Mtb*Cbs generates H₂S using Cys or Hcys + Cys but not from Hcys alone (fig. S1I). In addition, using liquid chromatography–tandem mass spectrometry (LC-MS/MS), we confirmed that *Mtb*Cbs produces Lnth from Cys (fig. S2A). Further, *Mtb*Cbs produces Cysth from Ser + Hcys and Cys + Hcys (fig. S2, B to D). However, unlike human CBS (hCBS), it does not generate Ser from Cys. We calculated the steady-state kinetic parameters of the *Mtb*Cbs H₂S-generating reactions (fig. S3, A to C, and table S2), which revealed the kinetic preference for the condensation of Hcys + Cys over two molecules of Cys.

Because *Mtb*Cbs harbors the SAM binding Bateman module, we next tested whether SAM allosterically regulates *Mtb*Cbs. We found that SAM, in a concentration-dependent manner, enhanced the H₂S-producing activity of *Mtb*Cbs by two- to fourfold (Fig. 1A), similar to what has been observed in hCBS (34). Under steady-state conditions, SAM increased the V_{max} of both the Lnth- and Cysth- generating

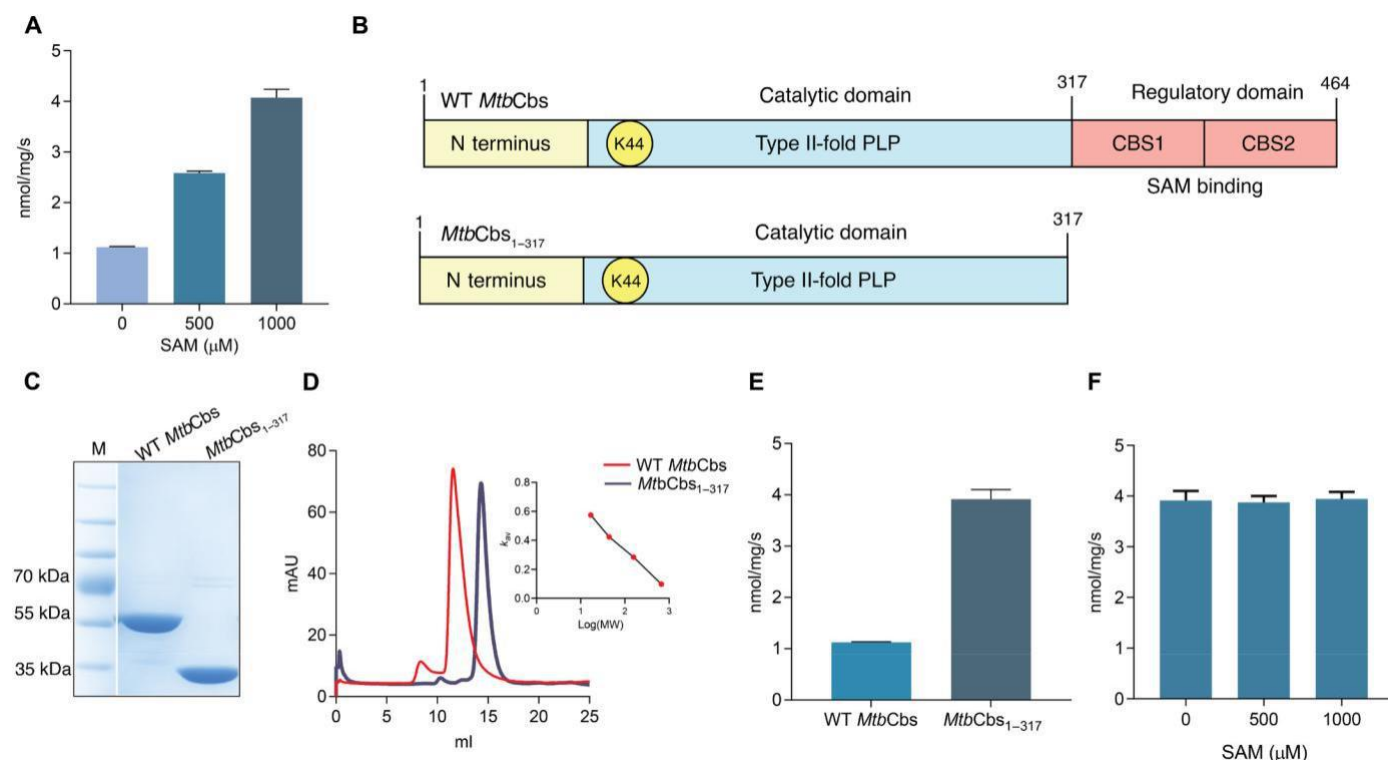


Fig. 1. *Mtb*Cbs is allosterically activated by SAM. (A) Specific activity of H₂S production by *Mtb*Cbs in the presence of the indicated amounts of SAM and 20 mM Cys as substrate. (B) Schematic diagram of the modular arrangement of WT *Mtb*Cbs and *Mtb*Cbs₁₋₃₁₇ with C-terminal 147–amino acid deletion. (C) SDS–polyacrylamide gel electrophoresis (PAGE) gel of purified *Mtb*Cbs and *Mtb*Cbs₁₋₃₁₇. For representation, the marker lane (M) was inserted with the protein lanes. (D) SEC profile of Ni-NTA–purified *Mtb*Cbs and *Mtb*Cbs₁₋₃₁₇. mAU, milli-arbitrary units; MW, molecular weight. (E) Specific activities of H₂S production by *Mtb*Cbs and *Mtb*Cbs₁₋₃₁₇ showing increased basal activity of *Mtb*Cbs₁₋₃₁₇. (F) *Mtb*Cbs₁₋₃₁₇ was not activated further in the presence of increasing concentrations of SAM.

reactions, with moderate change in the k_m of Cys, while that of Hcys remained unchanged (fig. S3, D to F, and table S2). We also purified a *MtbCbs* mutant lacking the Bateman module (*MtbCbs*_{1–317}) (Fig. 1, B and C), which eluted as a dimer (M_r 65 kDa) (Fig. 1D), exhibiting significantly higher basal specific activity than wild-type (WT) *MtbCbs* (Fig. 1E), and was nonresponsive to SAM (Fig. 1F). Under steady-state conditions, the kinetic parameters of H₂S generation by *MtbCbs* 1–317 were similar to that of WT *MtbCbs* in the presence of SAM (fig. S3, G to I, and table S2), confirming that the deletion of the SAM binding domain constitutively activated *MtbCbs*. To the best of our knowledge, this is the first report of a bacterial CBS-exhibiting SAM-dependent activation and oligomerization via its SAM binding Bateman module.

Structure of full-length WT native *MtbCbs*

Because *MtbCbs* was tetrameric and responsive to SAM, we next investigated the structural aspects of its assembly to understand the mechanism of SAM-mediated activation. Single-particle cryo-EM was used to analyze the conformation of the native tetrameric *MtbCbs*. Initially, native *MtbCbs* was observed by room-temperature negative staining transmission electron microscopy (TEM) to identify the overall shape and stability of the complex. Negative staining TEM micrographs and reference-free two-dimensional (2D) class averages revealed a rectangular-shaped tetrameric architecture of native *MtbCbs* (fig. S4A). The same sample was used to perform cryo-EM imaging (fig. S4B), and the atomic-resolution 3D reconstruction of the *MtbCbs* homotetramer was resolved at 3.6 Å, with the core domain resolved at 3.1 Å (Fig. 2A and figs. S4, C to E, and S5A). The rectangular-shaped 3D structure of the tetrameric *MtbCbs* contains an N-terminal catalytic core region (7 to 296 residues), C-terminal Bateman module (329 to 464 residues), and a connecting linker between the catalytic core and the Bateman module (297 to 328 residues) (Fig. 2, A and B). The stable catalytic core of one monomer is firmly associated with the catalytic core of another monomer in

a head-to-head fashion mainly through hydrophobic interactions (M1 and M2; M3 and M4), with a total dimeric surface area of 1882 Å² (Fig. 2C and fig. S5B). The Bateman module is composed of two CBS motifs, CBS1 (T329–E397) and CBS2 (A403–E459), existing in tandem repeats (Fig. 2D). Similar kind of tandem repeats have previously been reported in hCBS (35). The Bateman module is positioned outmost from the catalytic core region and is connected to the core domain by a 32–amino acid linker (²⁹⁷GGRGYMSKIFNDAWMS–SYGFLRSRLDGSTEQS³²⁸) (Fig. 2E). According to our structural analysis, the C-terminal Bateman module of one dimeric *MtbCbs* engages through hydrophobic interactions, salt bridges and H-bonding with another Bateman module of a dimer, in an antiparallel head-to-tail arrangement, resulting in the tetrameric conformation (M1 and M3; M2 and M4) (Fig. 2F and fig. S5B). The tetramer interface has a total surface area of 1779 Å². The overall structure of the N-terminal catalytic core domain of *MtbCbs* is quite similar to that of hCBS and *Drosophila* CBS (fig. S6, A and B) (36, 37). Similarly, the Bateman module is quite identical to hCBS (fig. S6A) (36). However, a significant difference is observed in the connecting linker and the position of the Bateman module with respect to its corresponding catalytic core domain. In hCBS, the Bateman module is juxtapositioned with the catalytic core, with the Bateman module of the M1 monomer leaning toward the catalytic core domain of M2 monomer (fig. S6A). Unlike other CBS enzymes, significantly in *MtbCbs*, the Bateman module is shifted toward the periphery of the

homotetramer through the movement of the connecting linker (fig. S6C). The connecting linker helps in the movement of Bateman module, which facilitates the tetrameric assembly of *MtbCbs* (Fig. 2F). The density of the connecting linker is well ordered and stable in our cryo-EM structure, which suggests the absence of any disordered amino acid residues (Fig. 2E).

The *MtbCbs* catalytic core domain is composed of 10 helices (a1, a4, a6, a8, a10, a11, a12, a14, a16, and a17) and eight b strands (b2, b3, b5, b7, b9, b13, b15, and b18) (fig. S7A). The helices (a1, a6, a8, a12, a16, and a19) of the core domain of one monomer strongly interact with the helices (a1, a6, a8, a12, a16, and a19) of the adjacent monomer to form a stable dimer (fig. S7, B to D). Furthermore, the tetramer interface is stabilized by the interaction of four helices (a20, a23, a26, and a32) present at the Bateman module of two antiparallelly placed monomers (fig. S8A). On the basis of the permissible bond length distance study, we predicted five key amino acid residues, E388, R450, I357, L454, and S393, to be responsible for tetramerization (fig. S8B). To validate this, we performed site-directed mutagenesis of these residues (E388A, R450A, I357A, L454A, and S393R) and analyzed the oligomeric status using SEC (fig. S8C). SEC profile revealed increased propensity of *MtbCbs* mutants (E388A, R450A, I357A, L454A, and S393R) to remain in the dimeric state. These mutations at the Bateman module along with its complete deletion (*MtbCbs*_{1–317}) confirmed our speculation of the oligomerization mechanism, which implicates Bateman module in the dimer to tetramer conversion of *MtbCbs* (Fig. 2F and fig. S8C). A major peak shift was observed in the SEC profile of the I357A mutant (fig. S8C). Further, negative staining reference-free 2D classifications of I357A showed the presence of a mixture of dimeric and tetrameric species (fig. S8D). Because the tetramerization state of *MtbCbs* also affects its basal activity and SAM responsiveness, specific activities of all the mutants were measured in the presence of SAM using Cys as a substrate. The basal specific activity of I357A (2.16 ± 0.11 nmol/mg per second) was twofold higher than that of WT *MtbCbs* (1.03 ± 0.15 nmol/mg per second) with no further SAM-mediated activation (fig. S8, E and F). Whereas for E388A and R450A mutants, the activity was severely compromised, the other two mutants, S393R and L454A, showed moderate activity with subtle change in the rate with increasing concentration of SAM (fig. S8, E and F).

Conformational changes of *MtbCbs* in the presence of SAM and serine

Similar approaches were implemented to unravel the conformational changes of *MtbCbs* in the presence of SAM, and the 3D structure was determined at a resolution of 3.56 Å, with the core domain re-solved at 2.8 Å (Fig. 3, A and B, and fig. S9). SAM-treated *MtbCbs* retained its rectangular shaped tetrameric assembly similar to native *MtbCbs* (fig. S9, A and B). However, some significant differences between these two structures were observed with substantial conformational changes occurring at the Bateman module of SAM-treated *MtbCbs* and at the opening of the substrate channel. Because the EM density of SAM was missing in the CBS domain at the root mean square deviation (RMSD) value of 6s, we predicted the SAM binding position at a low RMSD value of 3s and pinpointed the probable SAM binding amino acid residues (fig. S10, A and B). Previous studies with hCBS demonstrated the role of F443, Q445, D538, and T535 amino acid residues in SAM binding (fig. S10C) (36). Upon superimposition of the Bateman modules of hCBS and *MtbCbs* (fig. S10D), we predicted E390, S411, D432, and W433 as the key

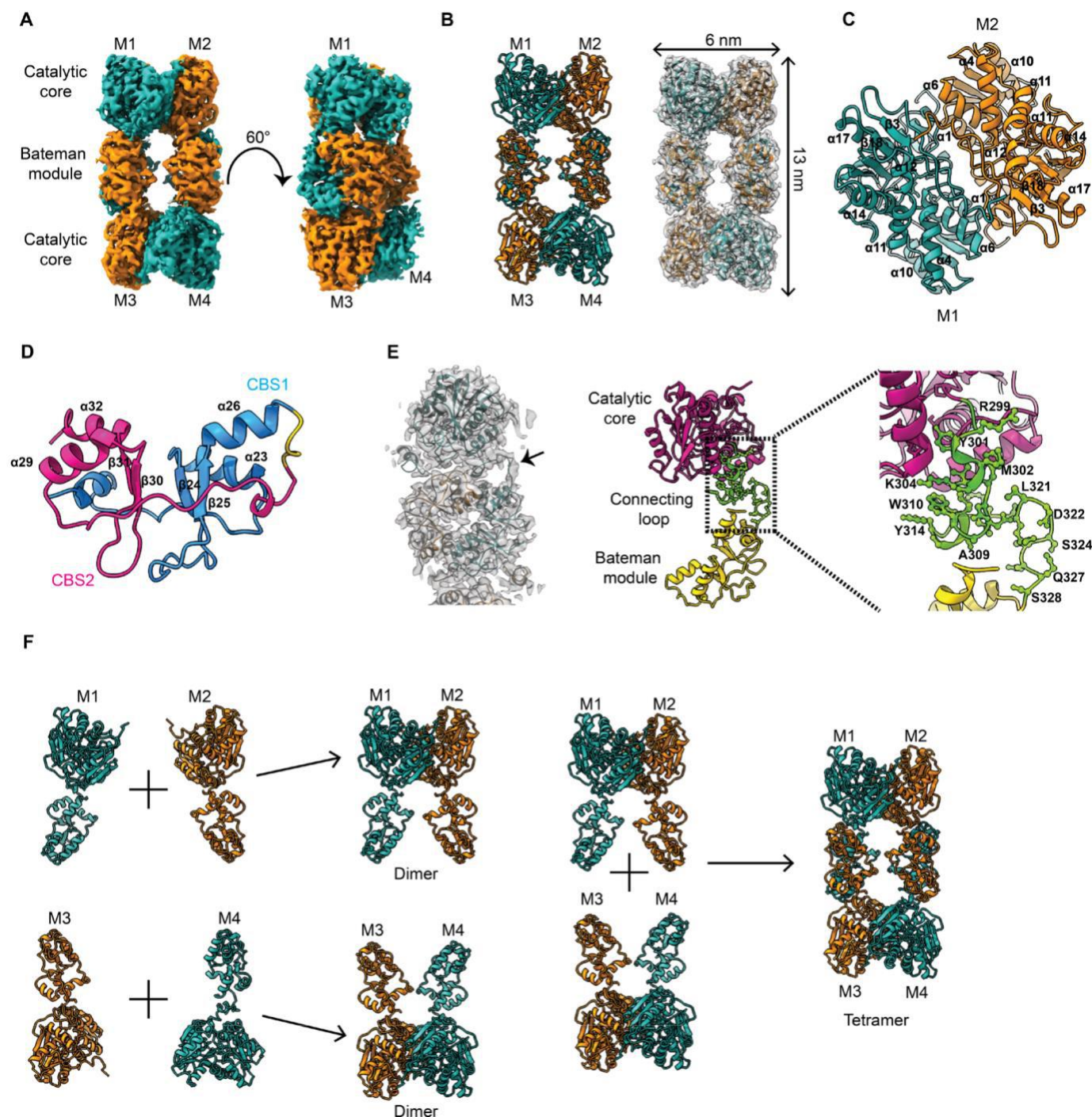


Fig. 2. Cryo-EM 3D reconstruction and atomic model building of native *MtbCbs*. (A) Solid representation of cryo-EM 3D model of native *MtbCbs*. Arrangement of four monomers of *MtbCbs* is shown in two different colors, green and orange, where the diagonally opposite monomers have the same color. Arrangement of catalytic core and Bateman module is marked. Bateman modules from two monomers interact antiparallely to form a tetrameric *MtbCbs*. Four different monomers are marked M1 to M4. (B) Atomic model of tetrameric *MtbCbs* in the left panel. Arrangement of four monomers of *MtbCbs* is shown in two different colors, green and orange, where diagonally opposite monomers are shown in two different colors. Four different monomers are marked M1 to M4. Transparent representation of *MtbCbs* fitted with the atomic model in the right panel. The length of *MtbCbs* is 13 nm, whereas breadth is 6 nm. (C) Enlarged view of catalytic core region. The helices and β strands are marked. (D) Enlarged view of the Bateman module of *MtbCbs*, which contains two tandemly repeated CBS motifs (CBS1 and CBS2), colored in blue and pink, respectively. The helices and β strands are marked. (E) The connecting loop between catalytic core and Bateman module is shown with black arrowhead. Middle panel shows the atomic model of a monomer of *MtbCbs*, where the catalytic core is colored in purple, the Bateman module is colored in yellow, and the connecting loop is colored in green. The right panel showed the enlarged view of connecting loop. The amino acid residues present in the loop region are G297–S328. (F) Proposed mechanism for oligomerization of *MtbCbs*. M1 and M2 monomeric subunits interact with each other to form dimer, whereas M3 and M4 monomeric subunits interact with each other to form another dimer unit. Two dimeric *MtbCbs* units interact to form a tetramer.

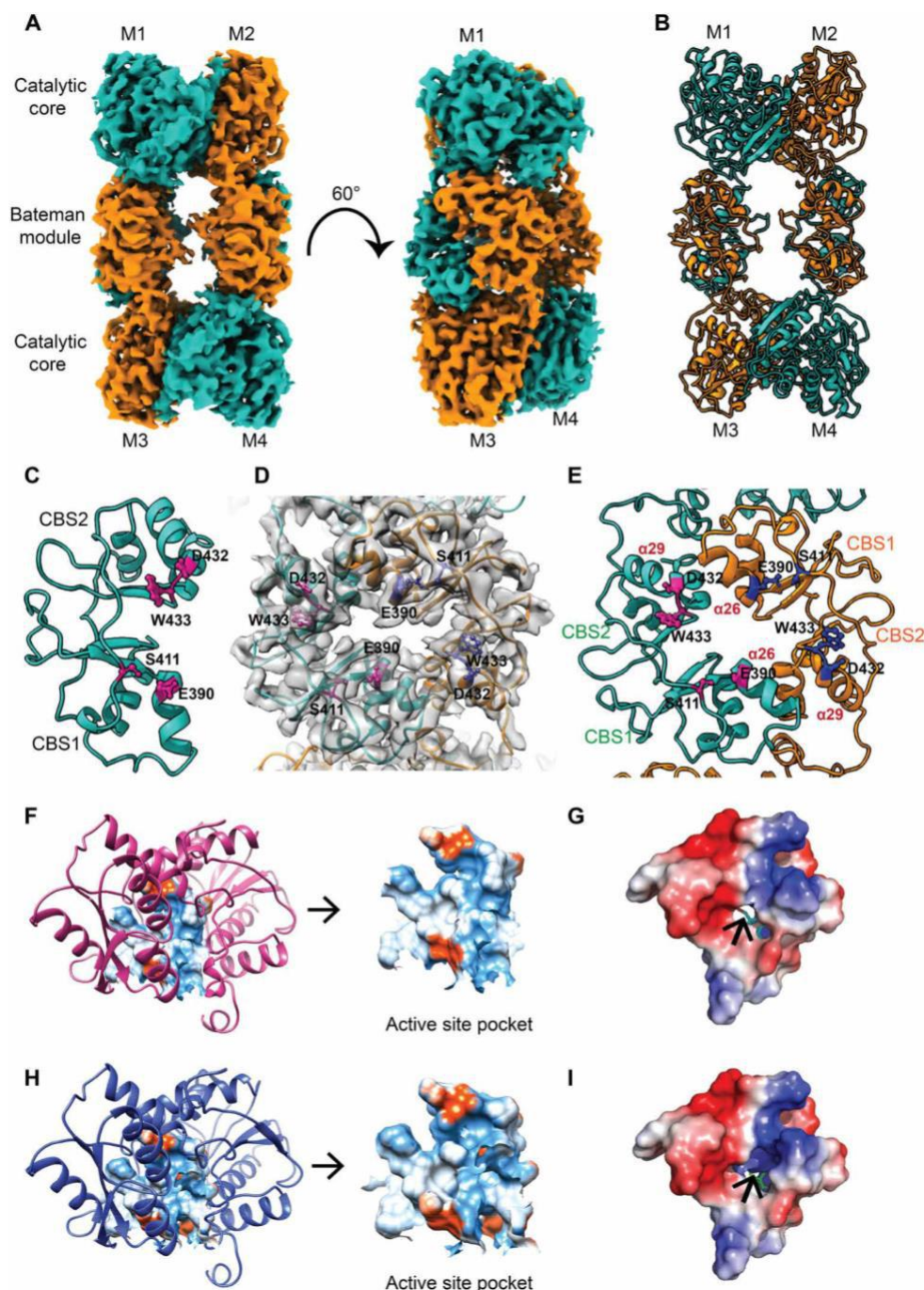


Fig. 3. Cryo-EM reconstruction and atomic model building of *MtbCbs* in the presence of allosteric activator SAM. (A) Solid representation of cryo-EM 3D model of *MtbCbs* in the presence of SAM. Arrangement of four monomers is shown in two different colors, green and orange, where the diagonally opposite monomers have the same color. Arrangement of catalytic core and Bateman module is marked, which indicates similar structural arrangement like native *MtbCbs*. (B) Atomic model of tetrameric *MtbCbs* in the presence of SAM. Four monomers in the atomic model are shown in two different colors, green and orange, where the diagonally opposite monomers have the same color. (C) Identification of key residues (W433, E390, S411, and D432) in *MtbCbs* responsible for SAM binding. (D) Enlarged transparent representation fitted with atomic model of the *MtbCbs* Bateman module. Two different monomeric chains are colored in green and orange. (E) Atomic model of the Bateman module marked with SAM binding amino acid residues in magenta and blue colors in each chain, respectively. (F) Determination of substrate groove pocket and position of the pocket in native *MtbCbs*. The pocket property is marked with the electrostatic potential value. Red color signifies negative potential, white near neutral, and blue positive potential. (G) Electrostatic potential calculated for active site of native *MtbCbs*. Substrate channel opening is shown with a black arrow. (H) Determination of substrate groove pocket and position of the pocket in SAM-treated *MtbCbs*. Electrostatic potential values indicate the surface changes of the amino acids present in the pocket. Red color signifies negative potential, to white near neutral, and to blue for positive potential. The redistribution of surface charges changes after SAM treatment due to the rearrangement of amino acids of SAM binding loop. (I) Electrostatic potential calculated for active site of SAM-treated *MtbCbs*. Substrate channel opening increases because of allosteric activation of the enzyme (marked with a black arrow).

amino acid residues involved in SAM interaction in *Mtb*Cbs (Fig. 3, C and D). Among these, W433 forms stabilizing stacking interactions with the purine ring of SAM. To validate this, site-directed mutagenesis of these amino acid residues (E390A, S411A, D432N, and W433F) was performed (Fig. 3E). All the mutants retained their tetrameric oligomeric organization but showed significant decrease in SAM-dependent activation, with W433F mutant being the most severely affected (fig. S10E). To rule out the possibility that the decrease in SAM-dependent activation of W433F resulted from enzyme instability, we performed fluorescence thermal shift assay of WT *Mtb*Cbs and W433F. We did not observe any shift in the thermal profile and in the melting transition temperature (T_m) of WT *Mtb*Cbs ($57.3^\circ \pm 0.592^\circ\text{C}$) and W433F ($58.06^\circ \pm 0.55^\circ\text{C}$), thus indicating that the W433F mutation does not influence enzyme stability (fig. S11A). We further performed microscale thermophoresis assay to ascertain the effect of W433F mutation on SAM binding affinity. The WT *Mtb*Cbs displayed a binding affinity (K_d) of ~ 128 mM, which was reduced to ~ 300 mM in W433F (fig. S11, B and C). This can be attributed to the disruption of stacking interaction between SAM and W433F. As expected, *Mtb*Cbs_{1–317}, which lacks the C-terminal SAM binding domain, did not display any SAM binding (fig. S11D). Together, these findings identified the amino acid residues involved in SAM binding and SAM-dependent activation.

After SAM treatment, significant changes were observed in the substrate channel of the active site K44. In all the CBS orthologs, the active site invariable lysine is highly conserved. In native *Mtb*Cbs, the active site K44 is buried inside the core region by a flexible loop (G40, G41, S42, S43, D45, and R46), making K44 relatively inaccessible to the substrates. After SAM incubation, the active site K44 gets exposed because of the displacement of the amino acids near the active site region and the substrate channel expands (Fig. 3, F to I). Upon allosteric activation by SAM, this rearrangement of the amino acids occurs to accommodate the higher influx of the substrates toward the active site. These observations revealed the structural basis of SAM-mediated allosteric activation of *Mtb*Cbs.

The active site lysine, K44, is located inside the catalytic core domain on helix α_4 and forms a Schiff base interaction with PLP (Fig. 4, A to C). PLP is involved in the interaction with other amino acids (S42, N74, G181, G183, T182, T185, and S269). Our 3D structure shows that S269, G181, G183, T182, and T185 are involved in hydrogen bonding (Fig. 4D).

As the substrate channel expands after SAM treatment, our next target was to observe the changes after SAM and substrate Ser incubation. 3D structure of *Mtb*Cbs retains its tetrameric arrangement after SAM + Ser incubation, and the 3D reconstruction was resolved at a resolution of 4.25 Å (figs. S12 and S13). In the absence of Ser, a stable continuous density is present in the cryo-EM map between K44 and PLP at an RMSD value of 6s. This indicates the formation of internal aldimine at the active site (Fig. 4E). However, substrate-treated cryo-EM map demonstrated that the interaction between K44 and PLP is disrupted after Ser treatment, followed by the formation of external aldimine/aminoacrylate at the active site, which indicates association of Ser with PLP (Fig. 4, F and G), in agreement with previous reports (34, 38), which is strongly supported by our structural studies.

SAM stabilizes *Mtb*Cbs by occluding proteasomal degradation

SAM is known to confer stability to hCBS in addition to allosteric activation (27). To investigate whether SAM stabilizes *Mtb*Cbs

in vitro, we performed the pulse proteolysis assay (39) using thermolysin under denaturing conditions. In presence of 500 mM SAM, the G_m value (urea concentration required to unfold half of *Mtb*Cbs) increased from 3.7 ± 0.3 to 4.92 ± 0.55 M. The global stability of *Mtb*Cbs, $\Delta G^\circ_{\text{unf}}$, increased from 21.2 ± 0.2 to 30.34 ± 0.91 kcal/mol (fig. S14 and table S4). Hence, binding of SAM provides significant stabilization to *Mtb*Cbs. We also performed the pulse proteolysis assay of the SAM unresponsive E390A, D432A, D432N, and W433F mutants and found that the presence of SAM did not confer protection from thermolysin-mediated proteolysis (fig. S15 and table S4).

After establishing that SAM stabilizes *Mtb*Cbs in vitro, we were interested to understand how intracellular SAM abundance regulates its stability in vivo. In *Mtb*, SAM is synthesized by the enzyme SAM synthetase (MetK; Rv1392). A purine analog, azathioprine (AZA) is a well-established inhibitor of *Mtb* MetK (40). We confirmed that treatment with 1 mM AZA resulted in depletion of SAM in a time-dependent manner (Fig. 5A). Concomitantly, cellular *Mtb*Cbs protein levels also reduced ($P = 0.0035$) (Fig. 5, B and C) without affecting the *cbs* transcript (fig. S16A). Exogenous supplementation with 1 mM SAM for additional 3 hours rescued AZA-mediated down-regulation of *Mtb*Cbs (Fig. 5, D and E) and restored intracellular SAM levels (fig. S16B). We genetically expressed the E390A, S411A, D432A, and W433F mutants in the *Mtb* strain lacking WT *Mtb*Cbs (*MtbDcbs*) and found that SAM failed to rescue the down-regulation of these proteins upon AZA treatment (fig. S17, A to H). Furthermore, we also expressed *Mtb*Cbs_{1–317} in *MtbDcbs* (*Mtbcbs*_{1–317}) and showed that deletion of the Bateman domain rendered it insensitive to AZA-mediated down-regulation (Fig. 5, F and G). This indicated the existence of a regulatory motif in the C terminus of *Mtb*Cbs that is crucial for SAM-dependent stabilization of *Mtb*Cbs.

Recently, *Mtb*Cbs was reported to have a pupylation site at lysine-428 (K428), which likely facilitates prokaryotic ubiquitin-like protein (Pup)-mediated proteasomal degradation of mycobacterial proteins (41). Because K428 lies in the SAM binding cleft of the Bateman module, we proposed an “occlusion by occupation model” to explain SAM-dependent degradation of *Mtb*Cbs. Under SAM sufficiency, SAM binding likely precludes protein degradation by sterically hindering the access of K428 for pupylation. Under SAM limitation, the exposed K428 of *Mtb*Cbs is pupylated and targeted for proteasomal degradation. Consistent with this, expression of a pupylation-deficient K428A mutant in *MtbDcbs* (*MtbcbsK428A*) prevented its degradation upon AZA treatment (Fig. 5, H and I). Together, we show that *Mtb*Cbs is sensitive to intracellular SAM and is likely targeted for proteasomal degradation during SAM limitation.

*Mtb*Cbs down-regulation reroutes transsulfuration toward SAM replenishment

We next interrogated the effect of SAM-dependent allosteric regulation of *Mtb*Cbs on AMC and RTS pathway of *Mtb*. We measured the abundance of the RTS pathway and AMC intermediates upon AZA-mediated SAM depletion by targeted metabolomics. Treatment of *Mtb* with 1 mM AZA for 6 to 12 hours led to a reduction in SAM ($P < 0.0001$) and Met ($P < 0.0001$) levels at 6 hours after treatment with AZA (Fig. 6, A to C). In comparison to 6 hours, 12 hours of AZA treatment showed signs of recovery in the levels of SAM ($P < 0.0001$), Met ($P < 0.0001$), and S-adenosylhomocysteine (SAH) ($P < 0.0001$) (Fig. 6, A to C). Aspartate (Asp), which is the main precursor of Met biosynthesis, also showed significant ($P < 0.0001$) increase at 12 hours after treatment with AZA (Fig. 6D). These

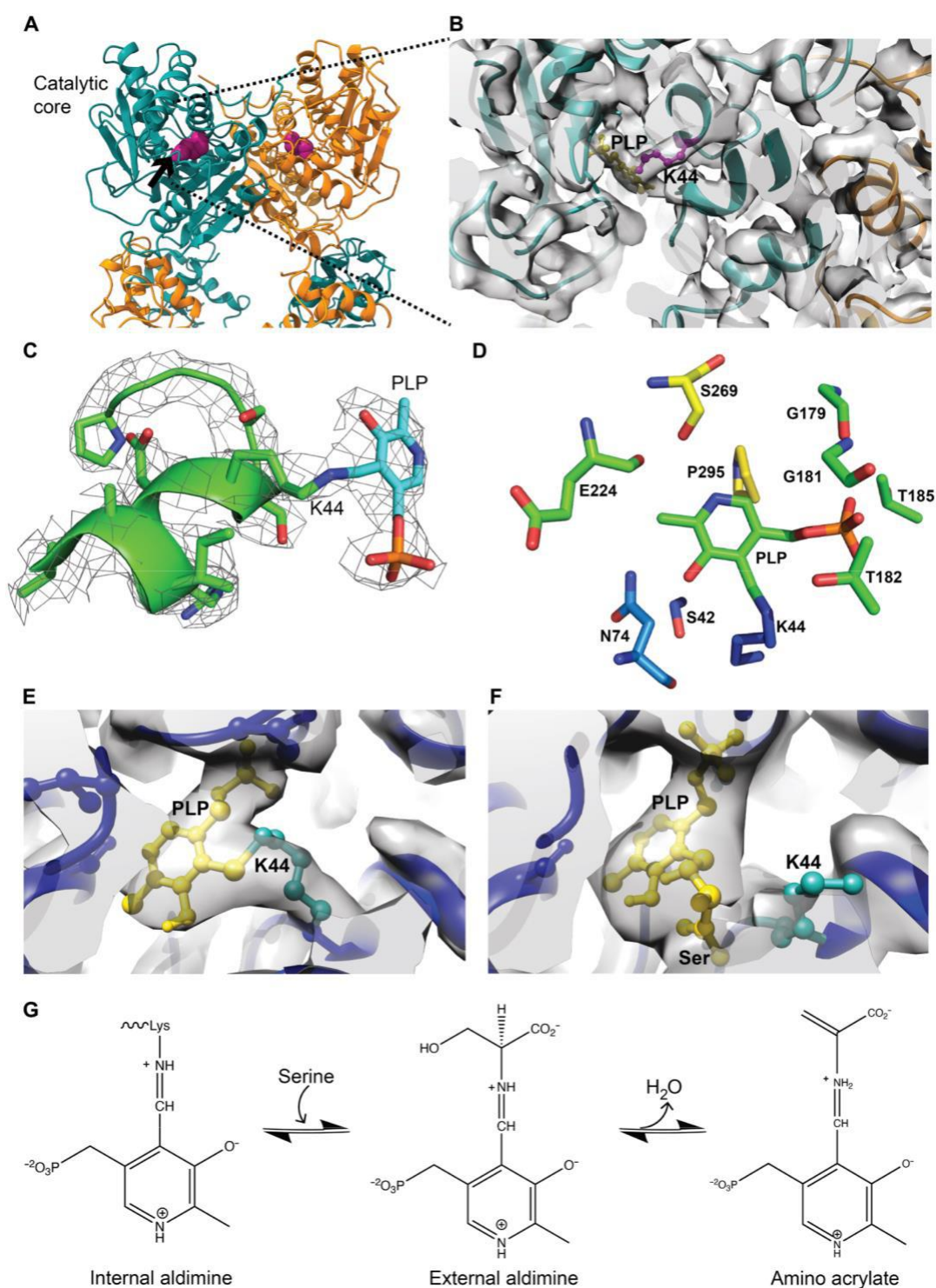


Fig. 4. Active site of *MtbCbs* and conformational changes after SAM and serine treatment. (A) Position of active site K44 in the catalytic core region. (B) Zoomed-in view of the active site indicates the presence of PLP. (C) A stable continuous density is present between K44 and PLP (fitted at an RMSD value of 6s). (D) Interaction of different amino acids and PLP at the active site groove. (E) A continuous density between K44 and PLP indicates the formation of internal aldimine at the active site in the SAM-treated *MtbCbs* model (fitted at an RMSD value of 6s). (F) The release of K44 and PLP interaction and the disappearance of continuous density between K44 and PLP indicate the formation of external aldimine/aminoacrylate in the presence of serine (fitted at an RMSD value of 6s). (G) Serine binding converts protonated internal aldimine form to external aldimine and aminoacrylate intermediates.

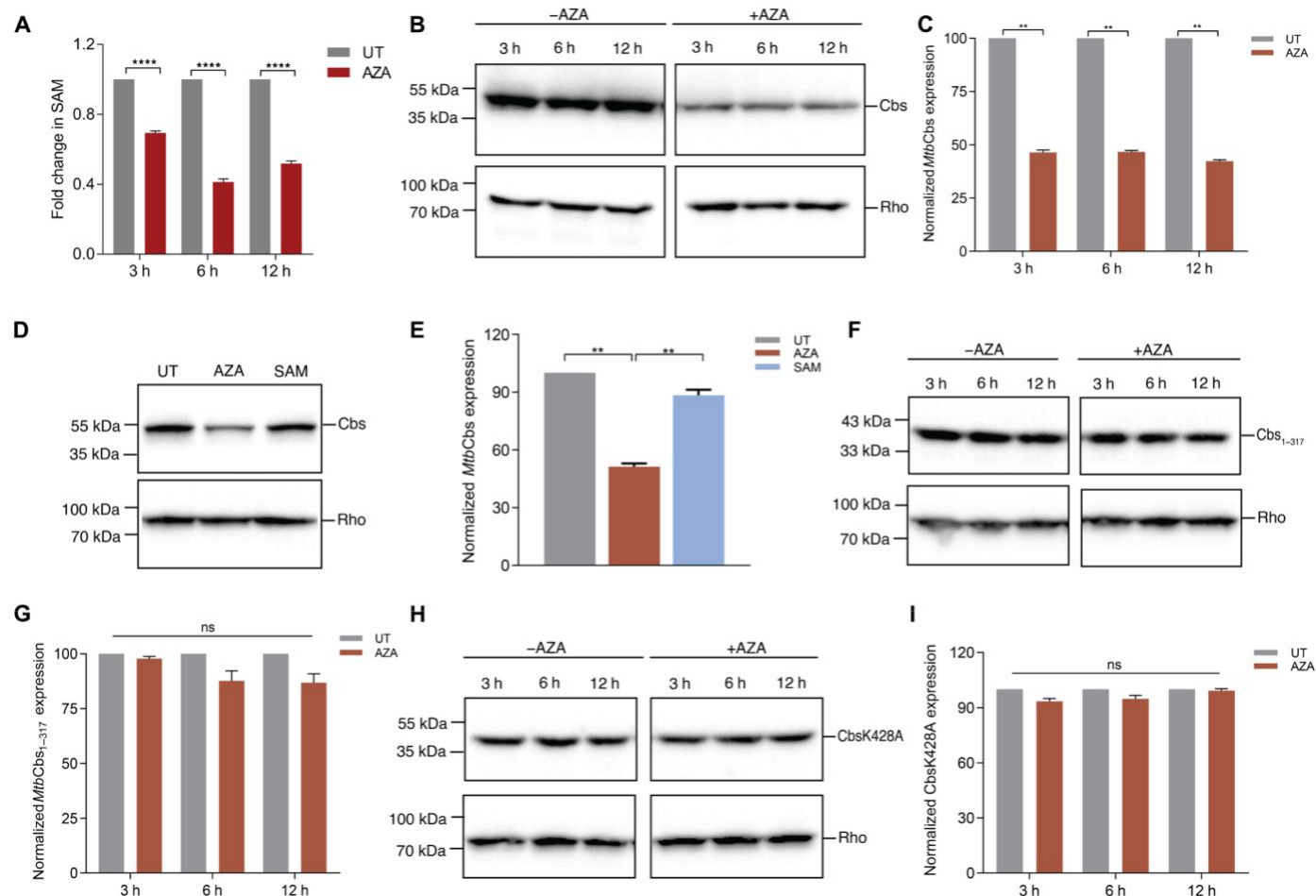


Fig. 5. SAM stabilizes *MtbCbs* in vivo by occluding proteasomal degradation. (A) Exponentially growing *Mtb* was treated with 1 mM AZA for the indicated time periods. **** $P < 0.0001$ by unpaired t test. Data represent means \pm SD of three independent biological replicates. (B) Immunoblotting of *MtbCbs* showing protein abundance upon treatment with 1 mM AZA for the indicated time periods and (C) the corresponding densitometry profile. *MtbCbs* expression was normalized to the expression of the internal control Rho. Data represent means \pm SD of two independent biological replicates. ** $P = 0.001$ by unpaired t test. (D) Immunoblotting of *MtbCbs* showing protein abundance upon treatment with 1 mM AZA for 3 hours, followed by addition of 1 mM SAM for additional 3 hours and (E) the corresponding densitometry profile. *MtbCbs* expression was normalized to the expression of the internal control Rho. Data represent means \pm SD of two independent biological replicates. ** $P = 0.0033$ by unpaired t test. (F) Immunoblotting of *MtbCbs*₁₋₃₁₇ showing protein abundance upon treatment with 1 mM AZA for the indicated time periods and (G) the corresponding densitometry profile. *MtbCbs*₁₋₃₁₇ expression was normalized to the expression of the internal control Rho. Data represent means \pm SD of two independent biological replicates. ns, not significant. (H) Immunoblotting of *MtbCbs*K428A showing protein abundance upon treatment with 1 mM AZA for the indicated time periods and (I) the corresponding densitometry profile. *MtbCbs*K428A expression was normalized to the expression of the internal control Rho. Data represent means \pm SD of two independent biological replicates. UT, untreated.

results suggested that *Mtb* likely responds to inhibition of SAM-*MtbCbs* axis by initially down-regulating Met biosynthesis, followed by a gradual recovery in the intracellular levels of AMC intermediates.

Down-regulation of *MtbCbs* is expected to reduce the intracellular levels of Cysth. However, contrary to our expectations, we observed significant increase in Cysth levels at 6 and 12 hours ($P < 0.0001$) after AZA treatment, respectively, as compared to untreated controls (Fig. 6E). Cysth is also an intermediate of the FTS pathway, which converts Cys to Met in bacteria such as *Escherichia coli* and *Salmonella typhimurium* (42). In the FTS pathway, Cysth g-synthase (CGS) condenses O-acetyl homoserine and Cys to form Cysth, which is then cleaved by Cysth b-lyase (CBL) to form Hcys for Met and SAM biosynthesis (Fig. 6F). Because we observed increased Cysth abundance upon SAM depletion, one likely possibility is that *Mtb* activates the FTS pathway of Met biosynthesis. *Mtb* encodes a

bifunctional enzyme, MetB (Rv1079), which has both CGS and Cysth g-lyase (CGL) activities (43) and therefore could generate Cysth to fuel Met biosynthesis and maintain viability in response to AZA. To test this, we treated *Mtb* with AZA for 3 hours alone or followed by exogenous supplementation with 1 mM SAM for an additional 3 hours. We found that Cysth levels increased only in the presence of AZA ($P < 0.0001$), while exogenous SAM addition reversed it to the level of untreated control (fig. S18).

We also measured the survival of *Mtb* upon treatment with the MetB inhibitor, propargylglycine (PAG; 500 mM) in combination with 1 mM AZA. While 1 mM AZA reduced *Mtb*'s survival by 40% ($P < 0.0001$), PAG alone was ineffective against *Mtb*. However, cotreatment with AZA and PAG led to 90% decrease ($P < 0.0001$) in *Mtb*'s survival as compared to the untreated control (Fig. 6G). Disruption of Met biosynthesis kills *Mtb* by inducing oxidative stress (7).

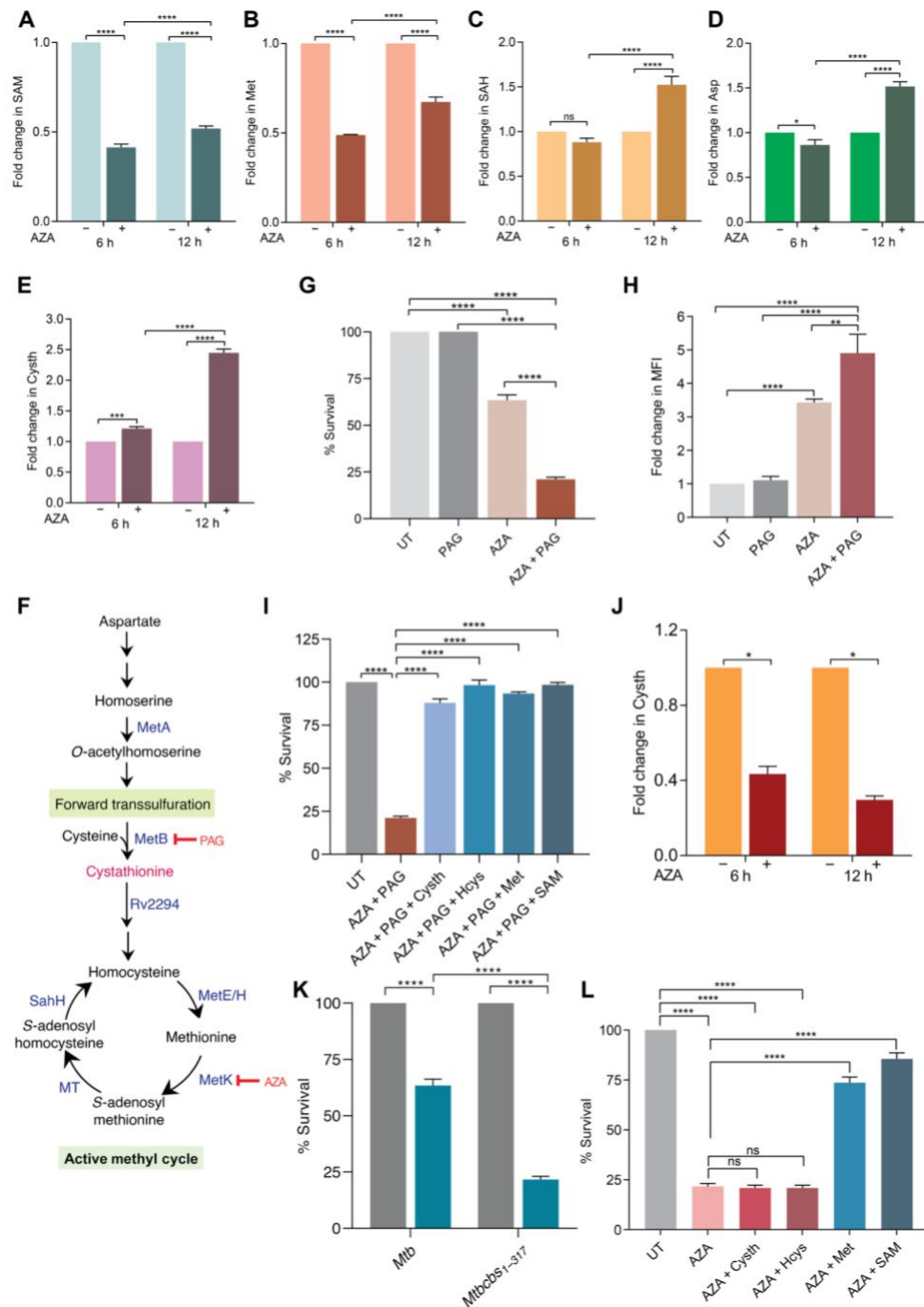


Fig. 6. SAM depletion signals resetting of the transsulfuration pathway in *Mtb*. (A to E) Fold change in abundance of RTS and AMC intermediates upon treatment with 1 mM AZA for the indicated time periods. Data represent means \pm SD of three independent biological replicates. * $P = 0.0114$, *** $P = 0.0005$, and **** $P < 0.0001$ by two-way analysis of variance (ANOVA) with Tukey's multiple comparison test. (F) Schematic showing the FTS pathway of methionine biosynthesis. MetA, homoserine O-acetyltransferase; MetB, bifunctional Cysth g-synthase/b-lyase; Rv2294, probable Cysth b-lyase; MetE, 5-methyltetrahydropteroyltryglutamate-homocysteine methyltransferase; MetH, 5-methyltetrahydrofolate-homocysteine methyltransferase; MetK, SAM synthetase; SahH, S-adenosylhomocysteine hydrolase. (G) Exponentially growing *Mtb* was treated with 1 mM AZA alone or in combination with 500 mM PAG for 24 hours. (H) ROS was detected (at 12 hours after treatment) by staining with CellROX DeepRed and analyzed by flow cytometry with $I_{\text{excitation}} = 644$ nm and $I_{\text{emission}} = 665$ nm. MFI, mean fluorescence intensity. (I) Rescue of the survival defect caused by cotreatment with AZA + PAG. Hcys, Cysth, Met, and SAM were added 6 hours after treatment with AZA + PAG at a final concentration of 1 mM each. (J) Fold change in Cysth abundance of *MtbCbs1-317* upon treatment with 1 mM AZA for 6 and 12 hours. (K) Exponentially growing *MtbCbs1-317* strain was treated with 1 mM AZA for 24 hours. (L) Rescue of the survival defect caused by AZA treatment in *MtbCbs1-317* strain. Hcys, Cysth, Met, and SAM were added 6 hours after treatment with AZA + PAG at a final concentration of 1 mM each. For all survival experiments, percent survival was calculated by colony-forming unit (CFU) enumeration on 7H11-ADS plates. (G to L) Data represent means \pm SD of three independent biological replicates. * $P = 0.0116$, ** $P = 0.0012$, **** $P < 0.0001$ by one-way ANOVA with Tukey's multiple comparison test.

Consistent with this, reactive oxygen species (ROS) levels were induced to 3.5-fold ($P < 0.0001$) upon treatment with AZA, which further increased to 5.0-fold ($P = 0.012$) in response to AZA + PAG combination (Fig. 6H). Exogenous supplementation with Cysth, Hcys, or Met rescued the growth defect and improved the survival of *Mtb* in response to AZA + PAG combination (Fig. 6I). Both the transcript and protein levels of MetB remained unchanged upon AZA treatment (fig. S19, A to C), suggesting that *Mtb* MetB is able to functionally switch from CGL to CGS upon aberration in *Mtb*Cbs-SAM axis. We propose that under SAM-sufficient condition, *Mtb*Cbs is stabilized and converts Hcys to Cysth. This kinetically constrains MetB to function as a CGL to generate Cys from Cysth via the RTS pathway. However, upon SAM depletion and concomitant destabilization of *Mtb*Cbs, MetB exerts its CGS activity to generate Cysth via the FTS pathway for replenishment of Met and SAM. These findings indicate that the induction of the FTS pathway via CGS activity of MetB is likely to be dependent on the concomitant depletion of both SAM and *Mtb*Cbs. Consistent with this, the CBS-deficient strain of *Mtb* (*MtbDcbs*) did not show any increase in Cysth levels upon AZA treatment (fig. S20), reiterating that *Mtb*Cbs down-regulation in response to SAM depletion is prerequisite for activating FTS pathway. To further assess this, we examined the effect of AZA treatment on *Mtbcbs*_{1–317}. Because it constitutively expresses CBS activity in a SAM-independent manner, MetB would be coerced to function as a CGL rather than a CGS even under SAM-deficient conditions. Consistent with this, Cysth levels did not increase in AZA-treated *Mtbcbs*_{1–317} (Fig. 6J). Furthermore, AZA-treated *Mtbcbs*_{1–317} showed a significant growth defect as compared to WT *Mtb*, indicating the inability of the strain to sustain CGS activity of MetB for maintaining essential AMC intermediate pools (Fig. 6K). In agreement with this, exogenous supplementation of Met or SAM, but not Hcys or Cysth, restored the survival of *Mtbcbs*_{1–317} in response to AZA (Fig. 6L). In summary, *Mtb*Cbs-SAM axis constitutes a novel regulatory node in the Cys-Met metabolism and proffers functional significance to the reversibility of the transsulfuration pathway in *Mtb*.

Antifolate drugs destabilize *Mtb*Cbs to affect survival in *Mtb*

Antifolate antibiotics such as *para*-amino salicylic acid (PAS) and sulfamethoxazole (SMX) have been reported to deplete critical AMC intermediates, including SAM, in *Mtb* (44). On the basis of this, we next checked the effect of antibiotics PAS and SMX on *Mtb*Cbs stability. We treated WT *Mtb* with 1, 5, and 10 MIC (minimum inhibitory concentration) of PAS and SMX for 12 hours. MIC was determined as described previously (20). We found that PAS and SMX treatment led to *Mtb*Cbs down-regulation, which was maximum at 10 MIC of both the antibiotics (fig. S21, A and B). As expected, the *Mtb*Cbs levels in SAM-unresponsive *Mtbcbs*_{1–317} and pupylation-resistant *MtbcbsK428A* remained unchanged (fig. S21, C to F). Further, we examined the sensitivity of WT *Mtb*, *MtbDcbs*, *Mtbcbs-comp*, *Mtbcbs*_{1–317}, and *MtbcbsK428A* toward PAS and SMX. We found that *Mtbcbs*_{1–317} showed a two- and fourfold decrease in MIC₉₀ of PAS and SMX, respectively, as compared to *MtbDcbs* and *Mtbcbs-comp* (fig. S22, A to C). In addition, MIC₉₀ of PAS and SMX was found to be twofold lower in *MtbcbsK428A* as compared to WT, *MtbDcbs*, and *Mtbcbs-comp* (fig. S22, A to C). These findings support our observations that under SAM-depleted condition, survival of *Mtb* is dependent on Cbs down-regulation and activation of the FTS pathway. Thus, the Cbs-SAM axis plays an important role in *Mtb*'s survival against antifolate antibiotics.

*Mtb*Cbs confers protection from Hcys toxicity and affects survival of *Mtb* during HIV-TB coinfection

Having shown the importance of SAM in regulating *Mtb*Cbs functionality, we next examined the metabolic consequences of complete loss of CBS activity in *Mtb*. Loss of *Mtb*Cbs did not lead to Cys auxotrophy, indicating that the RTS pathway is a minor Cys biosynthetic pathway in *Mtb* (fig. S23). It is widely known that defects in hCBS leads to excess Hcys, which adversely affects cellular health by inducing oxidative stress, leaching of essential metals (e.g., copper), dysregulation of protein activity (*N*-homocysteinylation), and accumulation of its precursor, SAH (45). On this basis, we first investigated the effect of *Mtb*Cbs deletion on AMC metabolites as described for WT *Mtb*. While we were not able to detect Hcys, *MtbDcbs* displayed increased abundance of AMC intermediates Met ($P = 0.0005$) and SAH ($P = 0.0005$) and decreased SAM/SAH ratio ($P = 0.0009$) (fig. S24, A to C). This suggests that in the absence of *Mtb*Cbs, *Mtb* likely mitigates potential Hcys accumulation by increasing the biogenesis of AMC intermediates. We next investigated the response of *MtbDcbs* to excess Hcys and found that the survival of *MtbDcbs* was significantly lower than WT *Mtb* upon exogenous addition of Hcys (Fig. 7A). These results indicate that *Mtb* pre-dominantly requires Cbs to maintain bacterial viability in response to Hcys overload. *MtbDcbs* did not exhibit any phenotype in response to various stress conditions including ROS, reactive nitrogen species (RNS), acidic pH (fig. S25, A to D) and antibiotics in vitro (table S5).

Higher circulating Hcys levels are uniformly associated with HIV-infected patients (46). We reasoned that *Mtb*Cbs could contribute to survival of *Mtb* during HIV-TB coinfection. We examined this idea by monitoring the survival of *MtbDcbs* in U1 monocytic cell line model of HIV-TB coinfection (20) and in the lungs of HIV-transgenic (HIV-Tg) mice. U1 cells are generated from U937 monocytes wherein two copies of HIV-1 genome are inserted, and viral multiplication can be easily induced by phorbol 12-myristate 13-acetate (PMA) (47). We first confirmed that the treatment with PMA (5 ng/ml) led to an increase in Hcys level in U1 but not in U937 cells (Fig. 7B). We subsequently infected PMA-treated U1 and U937 (uninfected HIV-1 control) with WT *Mtb*, *MtbDcbs*, and *Mtbcbs-comp* and measured survival over time, as described previously (20). In U937 cells, *MtbDcbs* showed marginally greater survival than WT *Mtb* and *Mtbcbs-comp* in U1 cells at 12 and 24 hours postinfection (p.i.). In contrast, survival of *MtbDcbs* was ~2.5-fold lower ($P = 0.0002$) in comparison to WT *Mtb* and the *Mtbcbs-comp* at 12 and 24 hours p.i. (Fig. 7, C and D). Last, we exploited the HIV-Tg mouse model (NL4-3D gag/pol), which expresses HIV-1 accessory proteins and recapitulates metabolic, redox, and pathological complications (e.g., cardiomyopathy, congenital cataracts, nephropathy, skin lesions, and severe wasting) induced by the virus in humans (48). Littermate mice of C57/BL6J strain were used as nontransgenic mice in this study. Similar to PMA-treated U1 cells, higher levels of Hcys levels were detected in the lungs of the (HIV-Tg) mice but not the WT mice ($P = 0.0451$; Fig. 7E). Next, we implanted ~100 bacilli of WT *Mtb*, *MtbDcbs*, and *Mtbcbs-comp* in the lungs via the aerosol route and measured survival at 4 weeks p.i. The survival of *MtbDcbs* was similar to WT *Mtb* and *Mtbcbs-comp* in the lungs of C57/BL6J strain. In contrast, the lung bacillary burden of *MtbDcbs* showed two- to threefold lower ($P < 0.0001$) survival in the HIV-Tg mice as compared to WT *Mtb* and *Mtbcbs-comp* (Fig. 7F). These results suggest that *Mtb*Cbs is important to promote *Mtb* survival in response to Hcys excess encountered by *Mtb* during HIV-TB coinfection.

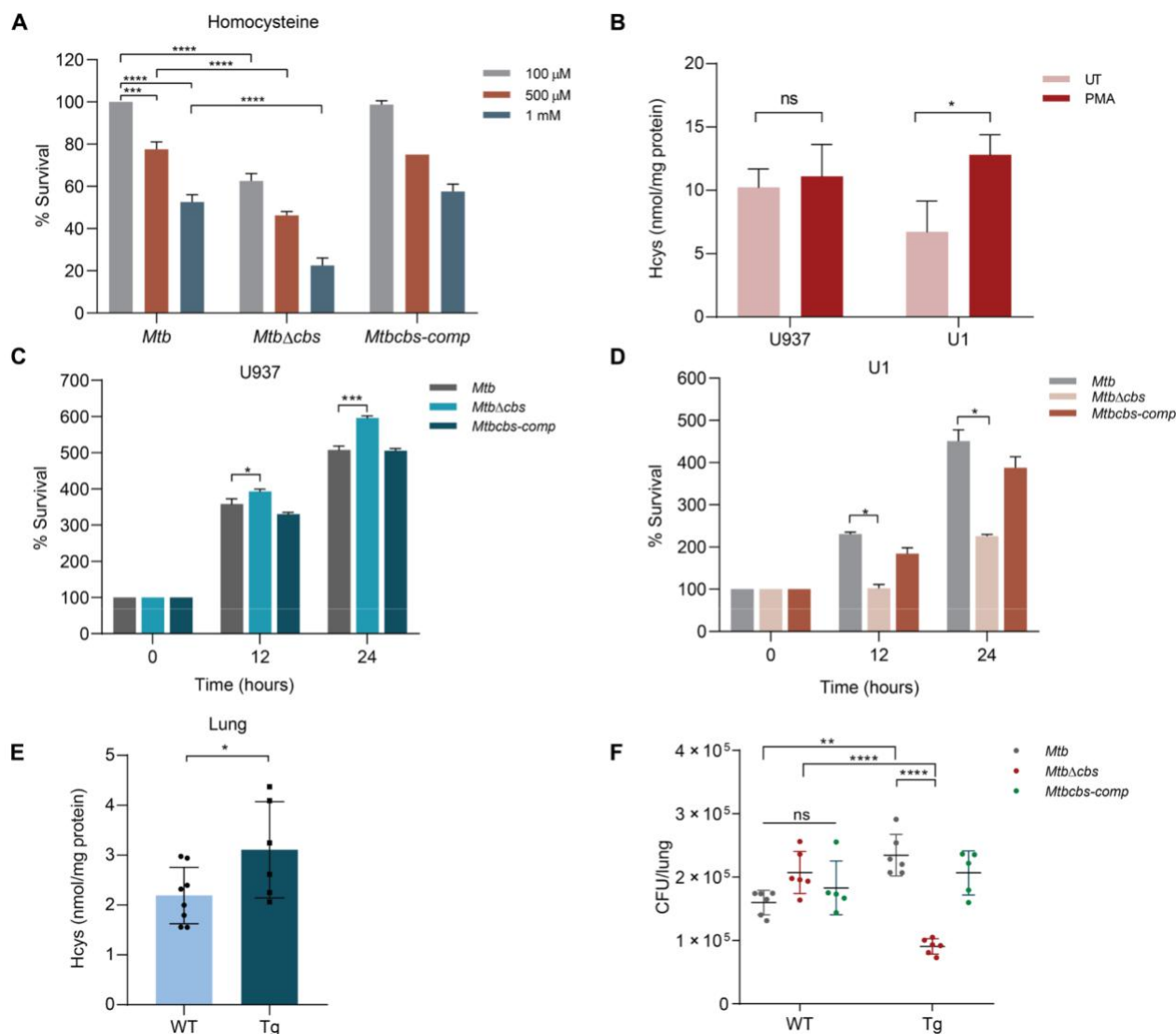


Fig. 7. *MtbCbs* is crucial for survival under conditions of Hcys excess. (A) Exponentially growing *Mtb*, *Mtb Δ cbs*, and *Mtbcbs-comp* were treated with the indicated amounts of Hcys for 24 hours, and percent survival was calculated by CFU enumeration. Data represent two independent biological experiments. *** $P = 0.0004$ and **** $P < 0.0001$ by two-way ANOVA with Tukey's multiple comparison test. (B) Hcys was measured in PMA activated U937 and U1 cells. Data represent three independent biological experiments. * $P = 0.0221$ by unpaired t test. Survival of *Mtb*, *Mtb Δ cbs*, and *Mtbcbs-comp* in PMA-activated (C) U937 and (D) U1 cell lines. Data represent two independent biological experiments. * $P = 0.0137$ by unpaired t test; *** $P = 0.0002$. (E) Estimation of Hcys in *Salmonella* lipopolysaccharide-treated WT ($n = 8$) and HIV-Tg ($n = 6$) mice. * $P = 0.0451$ by unpaired t test. (F) Survival of *Mtb*, *Mtb Δ cbs*, and *Mtbcbs-comp* in WT and HIV-Tg mice. WT ($n = 6$ for *Mtb*, *Mtb Δ cbs* each and $n = 5$ for *Mtbcbs-comp*) and HIV-Tg ($n = 6$ for *Mtb*, *Mtb Δ cbs* each and $n = 5$ for *Mtbcbs-comp*) were infected with 100 CFUs of each strain via the aerosol route. ** $P = 0.0024$ and **** $P < 0.0001$ by two-way ANOVA with Tukey's multiple comparison test.

DISCUSSION

Studies have shown that de novo Cys and Met biosynthetic pathways are indispensable for *Mtb*'s survival and pathogenesis. In addition, *Mtb* was also reported to possess a poorly characterized RTS pathway, which represents the sole source of Cys and the antioxidant glutathione in many eukaryotes. Here, we report that the first enzyme of the RTS pathway of *Mtb*, i.e., *MtbCbs*, is allosterically activated and stabilized by SAM and regulates Met metabolism in *Mtb*. Our study exemplifies how *Mtb* exploits the *MtbCbs*-SAM axis as a metabolic sensor to rapidly respond to perturbations of Met metabolism. Furthermore, *MtbCbs* ensures bacterial survival against the

toxic effects of excess Hcys encountered in vitro, inside macrophages, and in mice infected with HIV.

MtbCbs displays remarkable similarity to hCBS in terms of enzyme kinetics and SAM-dependent allosteric regulation but resembles its prokaryotic counterparts in being heme-less. Because heme-moiety of hCBS is exceptionally sensitive to ROS and RNS (49), the presence of a heme-less CBS in *Mtb* suggests an elegant evolutionary strategy to maintain RTS functionality despite the oxidatively and nitrosatively hostile environment it faces inside the phagocytes (50). In contrast to prokaryotic CBS and akin to hCBS, *MtbCbs* displays tetrameric assembly and SAM-dependent oligomerization.

*Mtb*Cbs demonstrates significant substrate promiscuity and in addition to its primary product CystH also yields Lnth and H₂S. While the calculated kinetic parameters shed light on the preference of substrate utilization, how these parallel reactions are regulated and the exact cellular conditions in which they become physiologically relevant remains unclear. Furthermore, *Mycobacterium smegmatis* mutants defective in meso-diamino pimelate biosynthesis were found to incorporate Lnth into the peptidoglycan (PG), which affected β -lactam susceptibility. Future experiments are needed to understand the contribution of *Mtb*Cbs in regulating the composition of *Mtb*'s PG and response to cell wall-targeting stresses (51).

Because the intrinsic instability of the tetrameric hCBS, its full-length structure remained uncharacterized. Although models of the structural mechanism of SAM-mediated allosteric activation of CBS exist and have yielded insightful information, they have relied heavily on the mutants of the full-length enzyme. The structures of hCBS and yeast CBS could only be resolved in the stable mutant dimeric forms of the native tetrameric enzymes [Protein Data Bank (PDB): 4COO, 4L3V, 1JBQ, 4PCU, and 6C4P] (35–38, 52). In this study, we resolved the full-length structure of *Mtb*Cbs in its native, activated, and substrate-bound conformations. We propose that the oligomerization of *Mtb*Cbs requires initial association of the monomers via their core domains to create dimers, which subsequently associate via their respective Bateman modules to yield the tetrameric assembly. The 3D structure indicates that the dimerization and tetramerization interfaces are stabilized predominantly by hydrophobic interactions.

The 3D structure of SAM-treated *Mtb*Cbs enabled us to understand the mechanism of SAM-dependent allosteric activation. Previous reports on hCBS showed that in the absence of SAM, the Bateman module blocks the access to catalytic site while in the presence of SAM, it shifts markedly to expose the catalytic site leading to allosteric activation (36). In contrast, native *Mtb*Cbs tetramer did not show any changes in the Bateman module in the presence or absence of SAM. We speculate that the likely reason behind the free movement of Bateman module in the dimeric hCBS is its considerable flexibility, which permits greater freedom of movement of the Bateman modules as compared to the more rigid tetrameric *Mtb*Cbs. Our data demonstrate that SAM binding was accompanied by rearrangement of amino acids leading to redistribution of the surface charges in the Bateman module. Furthermore, the active site lysine (K44), which remained buried inside the catalytic core, became more exposed because of the flexible loop's displacement at the substrate channel, which increased its accessibility. These structural rearrangements upon SAM binding led to enhanced influx of the substrate molecules resulting in enzyme activation. We identified the key amino acid residues responsible for SAM interaction at the Bateman module and confirmed their essentiality in activating *Mtb*Cbs by site directed mutagenesis. Furthermore, we were able to capture the formation of the external aldimine/aminoacrylate in presence of the substrate Ser at the enzyme's active site. However, our study cannot distinguish between these two intermediates (external aldimine and aminoacrylate) from this resolution structure.

In addition to the structural changes, our data suggest that SAM binding also stabilizes *Mtb*Cbs. We found that depletion of cellular SAM destabilizes *Mtb*Cbs by promoting its pupylation and subsequent degradation by the proteasomal machinery. Pupylation appears to be a protective mycobacterial response upon depletion of AMC metabolites as *Mtb* mutants defective in it were specifically sensitive

to folate inhibitors which affect Met metabolism (53). Consistent with this, we observed reduced survival of the pupylation resistant *MtbcbsK428* as compared to WT *Mtb*, *MtbDcbs*, and *Mtbcbs-comp* in response to PAS and SMX.

Under normal growing SAM-sufficient conditions, deletion of *Mtb*Cbs led to significant depletion of CystH, indicating that it functions as the housekeeping CystH synthase in *Mtb* (fig. S26). Under SAM-deficient conditions, destabilization of *Mtb*Cbs leads to repression of the RTS pathway and allows MetB to function as a CGS via the FTS pathway to replenish the AMC. However, the FTS pathway is not the canonical Met biosynthetic pathway in *Mtb* as deletion of MetB does not lead to Met auxotrophy (fig. S27). Consistent with this, the de novo MetA-dependent pathway appears to be the major route to generate AMC intermediates (7).

A distinctive feature of *Mtb*Cbs-SAM regulatory node is its exclusively metabolic and posttranslational nature, which bypasses the need for extensive transcription rewiring. The induction of the FTS pathway affords two advantages—first, because it is metabolically regulated, it can respond faster to a sudden drop in SAM. Second, the rapid conversion of *O*-acetylhomoserine to CystH and not Hcys ensures a unidirectional flow toward Met biosynthesis without interference from any residual activity of *Mtb*Cbs. MetC, an enzyme of the de novo biosynthetic pathway is predicted to be under the control of a SAM-dependent riboswitch (54). The expression of *metC* increases in Met starvation (7). However, derepression of *metC* and its subsequent increased translation, to lastly up-regulate Met biosynthesis, would constitute a multistep process as opposed to the simple metabolic switching exhibited by MetB. Our study does not preclude the importance of the MetC-dependent methionine biosynthesis, and it is likely that the SAM-riboswitch up-regulation of MetC may take over from the ad hoc FTS pathway under conditions of extended nutritional deprivation such as those encountered in granulomas. However, in the Wayne model of gradual oxygen depletion, *Mtb*Cbs is up-regulated under the microaerophilic conditions [nonreplicative stage 1 (NRP1)] stage, whereas Rv2294 a putative CBL involved in the FTS pathway is induced in hypoxia (NRP2) stage (55). It is therefore possible that the RTS to FTS switching might occur as an adaptive measure when *Mtb* transits into dormancy in response to a gradient of oxygen depletion.

Our metabolite data also revealed the failure of AZA to deplete SAM in *MtbDcbs* (fig. S28) to the extent observed in WT and complemented strains. The SAM/SAH ratio, an indicator of cellular methyl potential, was lower in *MtbDcbs* as compared to WT due to increased SAH abundance in *MtbDcbs*. SAH is a potent inhibitor of methyltransferases (56). It is possible that inhibition of SAM-dependent methyltransferases by SAH would have decreased the demand for SAM in *MtbDcbs* and consequently upon AZA treatment, the overall cellular SAM abundance remained unchanged.

In addition to Cys biosynthesis, CBS is the principal regulator of Hcys metabolism in mammals and prevents its cytotoxic accumulation (57). In *M. smegmatis*, exogenous Hcys has been found to disrupt biofilm formation (58). Our data indicate that while steady-state Hcys levels were not perturbed upon *Mtb*Cbs deletion, it is crucial for metabolizing surplus Hcys. Hcys acquisition using L-cystine uptake protein transporter (TcyP) has been found to support *Staphylococcus aureus* survival in murine heart and liver (59). Using a cell line and transgenic animal pathophysiological model of Hcys excess, i.e., HIV-TB coinfection, we highlighted the importance of *Mtb*Cbs in bacterial survival under this condition. This metabolic cross-talk between

the transsulfuration pathways of the host and the pathogen adds another layer of complexity in the pathophysiology and prognosis of TB disease.

MATERIALS AND METHODS

All chemicals were of analytical grade and purchased from Sigma-Aldrich (St. Louis, MO, USA), unless otherwise specified. All enzymes were purchased from New England Biolabs (Ipswich, MA, USA).

Bacterial strains and growth conditions

All *Mtb* strains were cultured in BBL Middlebrook 7H9 broth or BBL Middlebrook 7H11 agar (Becton, Dickinson and Company, Franklin Lakes, NJ, USA) at 37°C, supplemented with 10% ADS (albumin, dextrose, and sodium chloride), or 10% OADC (oleic acid, albumin, dextrose, sodium chloride, and catalase). *E. coli* DH5a and BL21 (DE3) were cultured in Luria Bertani broth or agar (HiMedia Laboratories, Mumbai, India). Kanamycin was used at a final concentration of 50 and 25 mg/ml for *E. coli* and *Mtb*, respectively. Hygro-mycin was used at a final concentration of 150 and 50 mg/ml for *E. coli* and *Mtb*, respectively.

Purification of recombinant WT *Mtb*Cbs and mutant proteins *cbs* (Rv1077) was amplified using Q5 High Fidelity polymerase from the genomic DNA of *Mtb* H37Rv using specific forward and reverse primers appended with Nco I and Hind III restriction sites, respectively, and cloned into pET28a expression vector (Novagen) for generating a C-terminal 6 His-tagged construct. For protein purification, cells were grown till an optical density at 600 nm (OD₆₀₀) of 0.6 and induced with 0.5 mM isopropyl-β-D-thiogalactopyranoside at 18°C for 24 hours. The cells were subsequently harvested by centrifugation at 5000 rpm for 10 min at 4°C. The bacterial pellets were resuspended in lysis buffer [50 mM tris-HCl (pH 8.0), 150 mM NaCl, 5% glycerol, 10 mM imidazole, 5 mM β-mercaptoethanol, 50 mM PLP, and 2 mM phenylmethylsulfonyl fluoride] and lysed by sonication on ice. The lysate was clarified by centrifugation at 13,000 rpm for 45 min at 4°C. Equilibrated Ni-nitrilotriacetic acid (NTA) beads (QIAGEN, Hilden, Germany) were added to the supernatant and kept for binding for 3 hours on a rotating platform at 4°C. The beads were then loaded onto a polypropylene gravity column (QIAGEN, Hilden, Germany) and washed with five-column volumes of equilibration buffer containing 50 mM tris-HCl (pH 8), 300 mM NaCl,

20 mM imidazole, 5% glycerol, and 0.5 mM β-mercaptoethanol. Protein was eluted using increasing concentration of imidazole. The elutes were pooled and dialyzed against two 1.5 liters of buffer volumes, containing 100 mM tris-HCl (pH 8), 150 mM NaCl, 20 mM PLP, 5% glycerol, and 0.5 mM β-mercaptoethanol. They were further concentrated using solid polyethylene glycol 20,000, aliquoted, flash-frozen, and stored at 80°C.

For negative staining and cryo-EM structural study, the Ni-NTA purified protein was loaded to Superdex 200 Increase 10/300 GL column (GE Healthcare Life Sciences, Piscataway, NJ, USA) for SEC [equilibrated with 50 mM tris (pH 8.0) and 150 mM NaCl], and the fractions were collected at a rate of 0.3 ml/min. The same protocol was followed for *Mtb*Cbs protein (~25 mM) incubated with 1 mM SAM (Sigma-Aldrich) and together 1 mM SAM (Sigma-Aldrich) and 10 mM L-serine (Sigma-Aldrich). Standard curve for calculation of molecular weight was made using protein standards of known molecular weight (Bio-Rad gel filtration standard).

Size exclusion chromatography–multiangle light scattering

The oligomeric state of *Mtb*Cbs protein was determined by SEC-MALS. Suprose-6 increase 10/300 GL (GE Healthcare Life Sciences, Piscataway, NJ, USA) analytical gel filtration column equilibrated with 50 mM tris (pH 8.0) (HiMedia Laboratories, Mumbai, India), 150 mM NaCl (Sisco Research Laboratories, India) with in-line UV (Shimadzu), MALS (mini-DAWN TREOS, Wyatt Technology Corp.) and refractive index detectors (WATERS24614). A total of 0.5 mg/ml (100 μl) of protein was injected. UV, MALS, and refractive index data were collected and analyzed using ASTRA software (Wyatt Technology, Santa Barbara, CA, USA).

Detection of CystH and Lnth

CystH production from serine and Hcys in presence and absence of SAM was detected colorimetrically using the acid-ninhydrin method as described in (60). The reaction mixture contained 50 mM tris-HCl buffer (pH 8), 20 mg of purified enzyme, 20 mM serine or O-acetylserine, and 10 mM L-Hcys in a total volume of 200 μl. After 20 min of incubation at 37°C, the reaction was stopped by adding 50 μl of 100% ice-cold trichloroacetic acid. The precipitated protein was removed by centrifugation at 13,000 rpm for 15 min. A total of 100 μl of supernatant was mixed with 1 ml of acid ninhydrin reagent (1 g of ninhydrin in 100 ml of concentrated acetic acid and 1/3 volume of phosphoric acid) and boiled for 5 min, followed by immediate cooling on ice for 2 min and subsequently held at room temperature for 30 min for color development. The absorbance was measured at 455 nm.

The production of CystH and Lnth was further confirmed by LC–electrospray ionization (ESI) MS/MS. One milliliter of reaction mixture contained 20 mg of purified *Mtb*Cbs in Hepes buffer (pH 8), 20 mM L-cysteine (for Lnth formation), 20 mM L-cysteine or 20 mM serine, and 10 mM L-Hcys (for CystH formation). The reaction was carried out for 15 min at 37°C and stopped by adding 50 μl of 100% ice-cold trichloroacetic acid. The precipitated protein was removed by centrifugation at 14,000 rpm for 15 min, and the supernatants were flash-frozen and stored at 80°C till analysis. Aliquots were injected into an Dionex 3000 Ultimate LC (Sunnyvale, CA, USA) equipped with C₁₈ column using gradients of mobile phases A (0.1% formic acid in water) and B (0.1% formic acid in acetonitrile). The flow rate maintained at 1 ml/min. A 30-min prerun was done for each sample with initial gradient conditions was done to equilibrate the column. Bruker Impact HD QTOF (high resolution hybrid quadrupole-time-of-flight) mass spectrometer (Billerica, MA, USA) equipped with an ESI source (negative ionization) was used in this LC-MS experiment. Data were analyzed using Bruker DataAnalysis (version 4.1 build 362.7). The identities of the thioether species were verified by MS/MS data using the online software CFM-ID 3.0 (Competitive Fragmentation Modeling for Metabolite Identification) (<https://cfmid.wishartlab.com/>).

Site-directed mutagenesis

Single primer method of site-directed mutagenesis was used to create point mutants of *Mtb*Cbs. pET28a-*cbs* was amplified in two separate reactions carrying with either the forward or reverse mutagenic primer. Briefly, after the initial denaturation step at 94°C for 2 min, polymerase chain reaction (PCR) was conducted for 30 cycles with denaturation at 94°C for 40 s, primer annealing at 55°C for 40 s, and DNA synthesis at 72°C for 7 min, followed by final extension at 72°C for 10 min. The reaction products were then mixed, heated to 95°C, and cooled slowly

to room temperature, to promote annealing and subsequently digested with Dpn I. The digested products were transformed into *E. coli* DH5a ultracompetent cells. Plasmids were isolated from single colonies using the QIAprep Spin Miniprep Kit (QIAGEN, Hilden, Germany) and sequenced for identification of positive mutants.

Generation of *Mtb cbs* knockout and complemented strains One-kilobase upstream and downstream regions of the genomic locus of *cbs* (Rv1077) were amplified using Q5 High-Fidelity polymerase and cloned at 5 and 3 ends, respectively, of the *loxP-hyg-gfp-loxP* cassette in the mycobacterial *sacB*-based suicide vector pML523 (a gift from M. Niederweis at the University of Alabama at Birmingham). The complete construct of the flanking sequences and the *hyg-gfp* cassette was subsequently amplified and cloned into the pRSF-duet vector (Clontech Laboratories, Mountain View, CA, USA) digested with Hpa I. The pRSF-*cbs* plasmid was pretreated with UV light and electroporated into WT *Mtb* H37Rv for allelic exchange. Positive clones ($\text{Hyg}^R\text{-Kan}^S\text{-GFP}^+$) were screened by genomic DNA PCR. Disruption of *cbs* was confirmed by reverse transcription quantitative PCR (RT-qPCR) and Western blotting. To unmark *MtbDcbs*, the pCre-ZEO-SacB plasmid (a gift from A. K. Pandey, Translational Health Science and Technology Institute, Haryana, India) was electroporated into *MtbDcbs* to allow for the loss of the *loxP-hyg-gfp-loxP* cassette from the genome. The resulting unmarked strains were confirmed by the loss of green fluorescent protein (GFP) fluorescence and antibiotic selection.

For creation of the complemented strain, *cbs* was amplified with its native promoter from *Mtb* genome and cloned in the integrative shuttle plasmid pCV125 (Medimmune, Gaithersburg, MD, USA) and electroporated into the unmarked *MtbDcbs* strain. *MtbDcbs* was also complemented with the mutagenic variants of WT *cbs*, which were unresponsive to allosteric activation by SAM. For this, the gene carrying the respective deletion or point mutation was cloned into the integrative pMV761 vector under *hsp60* promoter.

UV-VIS spectroscopy

Absorbance measurements for PLP detection were carried out in a BioMate 3S UV-VIS spectrophotometer (Thermo Fisher Scientific, Waltham, MA, USA) in quartz cuvettes using purified proteins (~1 mg/ml).

Pyridine hemochromagen assay

Pyridine hemochromagen assay was performed according to (61). Briefly, purified *MtbCbs* was treated with 0.2 M NaOH, 40% (v/v) pyridine, 500 mM potassium ferricyanide in a 1-ml quartz cuvette, and the spectra were recorded in BioMate 3S UV-VIS spectrophotometer (Thermo Fisher Scientific, Waltham, MA, USA) in quartz cuvettes. Subsequently, 0.5 M sodium dithionite in 0.5 M NaOH was added, and the spectra were recorded again. For clarity, only the reduced spectra were plotted.

Steady-state enzyme kinetics

The steady kinetic parameters of *MtbCbs* were determined by a continuous spectrophotometric lead acetate assay (32). Briefly, the reaction mixture comprised of 20 mg of the purified enzyme in Hepes buffer (pH 8), 0.4 mM lead acetate, Cys (0 to 50 mM), Hcys (0 to 8 mM), and 500 mM SAM as indicated. H_2S production from Cys and Hcys was estimated at 390 nm using $\epsilon = 5500 \text{ M}^{-1}$ for lead sulfide formation. Absorbance measurements were carried out in Versa-Max microplate reader (Molecular Devices, San Jose, CA, USA) in a 96-well plate with a reaction volume not exceeding 200 μl . To compute

the kinetic parameters, velocity data were fitted to either the standard Michaelis-Menten or bisubstrate kinetics equations.

Microscale thermophoresis

SAM binding to purified native and mutated *MtbCbs* was evaluated using microscale thermophoresis experiment (Nanotemper Technologies, Munich, Germany), that measures binding affinity of SAM. For this assay, the final protein concentration used was 100 nM. The protein was labeled with 100 nM red tris-NTA dye (Nanotemper Technologies, Munich, Germany) in the C terminus of the His-tag. Monolith NT.115 capillaries (Nanotemper Technologies, Munich, Germany) were used in each experiment. In the binding assay, the protein concentration for both native and mutated was kept constant. Both proteins were incubated with 16 twofold serial dilutions of the ligand SAM. The ligand was solubilized in a protein-containing buffer [50 mM Hepes (pH 7.4), 150 mM NaCl, and 3% glycerol]. The starting concentration for the ligand SAM was 500 mM for all the cases.

Fluorescence thermal shift assay

Fluorescence thermal shift assay was performed using 10 mg of purified protein and SYPRO orange dye (Bio-Rad, Hercules, CA, USA) using the fluorescence resonance energy transfer channel of the CFX96 RT-PCR System (Bio-Rad, Hercules, CA, USA).

Negative staining sample

preparation and visualization by TEM

SEC-purified native *MtbCbs* in the presence of SAM, SAM + serine, and the I357A mutant was visualized by negative staining electron microscopy (EM) to analyze homogeneity and particle distribution. All the samples were prepared by conventional negative staining methods. A carbon-coated copper grid (EM grid, 300 mesh; TedPella) was glow-discharged for 30 s at 20 mA. The purified protein was dialyzed without glycerol buffer for negative staining analysis [(50 mM tris (pH 8.0) (HiMedia Laboratories, Mumbai, India) and 150 mM NaCl (Sisco Research Laboratories)]. A total of 3.5 μl of the sample (0.1 mg/ml) was added to the glow-discharged (GloQube glow discharge system, Quorum) carbon-coated copper grid for 30 s. The extra sample was blotted out. Negative staining was performed using 1% uranyl acetate (98% uranyl acetate; ACS Reagent, Polysciences Inc. Warrington, PA, USA) solution for 20 s. The grid was air-dried. The negatively stained sample for native *MtbCbs*, SAM-treated *MtbCbs*, and I357A mutant were visualized at room temperature using Tecnai T12 electron microscope equipped with a LaB₆ filament operated at 120 kV, and images were recorded using a side-mounted Olympus VELITA (2000 2000) charge-coupled device camera at a magnification of 220,000 (2.54 Å per pixel). One hundred forty images were collected for native *MtbCbs*, 215 images were collected for SAM-treated *MtbCbs*, and 55 images were collected for I357A mutant manually for image processing. SAM + serine-treated *MtbCbs* was visualized at room temperature using Talos L120C transmission electron microscope (Thermo Fisher Scientific) equipped with Ceta (4000 4000) camera. Images were recorded at a magnification of

92,000 (1.52 Å per pixel). Around 40 images were collected for *MtbCbs* treated with SAM + serine.

Negative staining data processing and calculation of reference-free 2D classification

The evaluation of micrographs was done with EMAN 2.1 (62). A total of 12,541 particles for *MtbCbs* and 15,120 particles for SAM-treated

*Mtb*Cbs were manually picked using EMAN 2.1. The total number of particles were extracted separately for *Mtb* Cbs and *Mtb*Cbs treated with SAM using e2boxer.py in EMAN2.1 software package. Initially, e2refine2d.py was used to perform the 2D reference-free class averaging without any masking to visualize the structural integrity of *Mtb*Cbs. However, same dataset for both the samples (*Mtb* Cbs and SAM-treated *Mtb*Cbs) were subjected to reference-free 2D classification using RELION 2.1. In the first round of 2D classification, *Mtb*Cbs and SAM-treated *Mtb*Cbs dataset were split into 250 and 300 classes, respectively. The classes having the best signal-to-noise ratio were selected for the second round of 2D classification. A total of 8189 particles for *Mtb*Cbs and 10,738 particles for SAM-treated *Mtb*Cbs were selected for the second round of 2D classification. In the second round of 2D classification, *Mtb*Cbs and SAM-treated *Mtb*Cbs dataset were split into 150 and 200 classes, respectively. Last, 69 best classes with 6875 particles and 89 best classes with 9726 particles from *Mtb*Cbs and SAM-treated *Mtb*Cbs were selected for further 2D classification. The cleaned datasets of the samples were used for reference-free 2D classification, and reference-free 2D class averages of different particle projections were calculated using simple_prime2D of SIMPLE 2.1 software (63) with a mask diameter of 100 pixels at 2.54 Å per pixel.

For SAM + serine-treated *Mtb*Cbs, around 5000 were manually picked using EMAN 2.1. The total number of particles were extracted using e2boxer.py in EMAN2.1 software package. Initially, e2refine2d.py was used to perform the 2D reference-free class averaging without any masking to visualize the structural integrity of substrate-treated CBS protein. However, the same dataset was subjected to reference-free 2D classification using RELION 2.1. Several rounds of 2D classification were performed to clean the dataset. The cleaned dataset of the samples was used for further processing, and reference-free 2D class averages of different particle projections were calculated using simple_prime2D of SIMPLE 2.1 software at 1.52 Å per pixel.

For I357A mutant, around 4530 particles were manually picked using EMAN 2.1 and extracted using e2boxer.py in EMAN 2.1. Several rounds of 2D classification were performed using RELION 2.1 to clean the dataset. The cleanest dataset of samples was used for reference-free 2D classification of different particle projections and conformations using simple_prime2D of SIMPLE 2.1 software at 2.54 Å per pixel.

Cryo-EM sample preparation

R 1.2/1.3 (QUANTIFOIL) (Electron Microscopy Sciences) 300-mesh copper grids were glow-discharged for 90 s at 20 mA using Quorum GlowCube before sample preparation. The purified protein was dialyzed without glycerol buffer for negative staining analysis [50 mM tris (pH 8.0) (HiMedia Laboratories, Mumbai, India) and 150 mM NaCl (Sisco Research Laboratories)]. Three microliters of freshly prepared *Mtb*Cbs, *Mtb*Cbs treated with SAM, and *Mtb*Cbs treated with SAM + serine were added to the glow-discharged grids, incubated for 10 s, followed by blotting of 6.5 s at 100% humidity. The sample-containing grids were quickly plunged into liquid ethane using an FEI Vitrobot IV plunger (Thermo Fisher Scientific).

Cryo-EM data acquisition using 200-kV Talos Arctica and preliminary data processing for native *Mtb*Cbs and SAM-treated *Mtb*Cbs

The cryo-EM data collection was initially performed in 200-kV cryo-TEM (64) to achieve our targets and observe the structural

integrity of *Mtb*Cbs and *Mtb*Cbs with SAM at cryogenic temperature. Briefly, a small dataset (~300) was collected using 200-kV Talos Arctica cryo-EM (Thermo Fisher Scientific) equipped with K2 direct electron detector (Gatan Inc.) using Latitude-S automatic data acquisition tools. The data acquisition was performed at 42,200 magnification and a calibrated pixel size of 1.17 Å at specimen level. Total electron dose of about $40 \text{ e} / \text{Å}^2$ at the defocus range of 0.75 to 2.25 mm (table S3). Last, around 10,000 particles were selected for 2D classification, and 2D class averages indicate that *Mtb*Cbs with and without allosteric activators is organized as a tetramer.

Cryo-EM data acquisition using 300-kV Titan Krios and data processing for native *Mtb*Cbs and SAM-treated *Mtb*Cbs

For high-resolution cryo-EM structural characterization, cryo-EM data acquisition was performed using Thermo Scientific Titan Krios Transmission Electron Microscope operated at 300 kV equipped with a Falcon direct electron detector (Thermo Fisher Scientific). Images were collected automatically using Thermo Scientific EPU software at a pixel size of 1.07 Å at specimen level. Total electron dose was about $30 \text{ e} / \text{Å}^2$ at a defocus range of 2.2 to 3.9 mm. Data were recorded in a movie file for a total of 25 frames. A total of 1349 micrographs were collected for *Mtb*Cbs, and 1286 micrographs were collected for *Mtb*Cbs treated with SAM for further data processing (table S3).

Primarily, data processing was performed using RELION 3.0 (65). Initially, beam-induced motion correction was performed for each movie file using MotionCorr2 software (66). The micrographs having poor signal-to-noise ratio were discarded after screening in cisTEM software package (67), and the best micrographs were considered for further data processing. Contrast transfer function (CTF) was estimated using CTFFIND 4.1.13 (68). Initially, around 8000 particles were picked manually, and reference-free 2D classification was calculated using RELION 3.0 for both *Mtb*Cbs and *Mtb*Cbs-treated with SAM datasets. Best 2D class averages were selected as template for automated particle picking for both the datasets. After automatically particle picking, 980,992 particles were picked for native *Mtb*Cbs, and 803,322 particles were picked for *Mtb*Cbs treated with SAM. Automatically picked particles were extracted with a box size of 240 pixels, calibrated pixel size of 1.07 Å for both the datasets. After particle sorting, 961,170 particles were selected for native *Mtb*Cbs, and 787,020 particles were selected for SAM-treated *Mtb*Cbs. Several rounds of 2D classification were run subsequently to clean both the datasets. Around 12,000 particles were selected with best signal-to-noise ratio to generate an ab initio model. Extracted particles from the best 2D class averages were used to calculate the 3D classification using the previously determined ab initio structure as reference. However, the ab initio model was low-pass-filtered to 30 Å, to use as an initial 3D model for 3D classification.

For native *Mtb*Cbs, after three rounds of 2D classifications, 605,966 particles were selected for 3D classification. 3D classification was performed with C2 symmetry, and 605,966 particles dataset divided in 10 classes. From 3D classification result, class 4 (178,599 particles) was observed as a tetramer and well resolved. 3D autorefinement was carried out for class 4 using soft mask in RELION 3.0. Followed by 3D autorefinement, per-particle defocus refinement with beam tilt correction was done. Corrected particles were subjected for Bayesian polishing. Polished particles were subjected for another round of 3D refinement. A 3D autorefined map of native *Mtb*Cbs was sharpened using RELION 3.0 (table S3).

For SAM-treated *Mtb*Cbs, after three rounds of 2D classifications, 485,258 particles were selected for 3D classification. 3D classification was performed with C2 symmetry, and 485,258 particles were divided in eight classes. From 3D classification, result shows that class 6 (146,444 particles) was observed as a tetramer and well resolved. 3D autorefinement was carried out for class 6 using soft mask in RELION 3.0. The consensus particles set was selected for CTF refinement to correct the per-particle defocus values and beam tilt correction. Corrected particles were subjected for Bayesian polishing. Polished particles were subjected for another round of 3D refinement. 3D autorefined map of SAM-treated *Mtb*Cbs was sharpened using RELION 3.0 (table S3). The structural differences between native *Mtb*Cbs and SAM-treated *Mtb*Cbs were performed after super-imposing both the cryo-EM density maps in UCSF Chimera (69) and UCSF ChimeraX (70, 71).

Cryo-EM data acquisition using 200-kV Talos Arctica and data processing for SAM + serine-treated *Mtb*Cbs

The cryo-EM data collection for SAM + serine-treated *Mtb*Cbs was performed using 200-kV Talos Arctica cryo-TEM (Thermo Fisher Scientific) to achieve our targets and observe the structural changes of *Mtb*Cbs in the presence of SAM + serine at cryogenic temperature. A dataset of 1666 micrographs was collected in a movie file of 20 frames using 200-kV Talos Arctica cryo-EM (Thermo Fisher Scientific) equipped with a K2 direct electron detector (Gatan Inc.) using Latitude-S automatic data acquisition tools. The data acquisition was performed at 42,200 magnification, a calibrated pixel size of 1.17 Å at specimen level, and a total electron dose of about 40 e⁻/Å² at the defocus range of 0.75 to 2.25 μm.

Primarily, data processing was performed using RELION 3.1 (65). Initially, beam-induced motion correction was performed for each movie file using MotionCor2 software. The micrographs having a poor signal-to-noise ratio were discarded after screening in cisTEM software package (67), and the best micrographs were considered for further data processing. The CTF was estimated using CTFFIND 4.1.13 (68). Initially, around 8000 particles were picked manually and reference-free 2D classification was calculated using RELION 3.1. Best 2D class averages were selected as template for automated particle picking. After automatically particle picking, 786,924 particles were picked. Automatically picked particles were extracted with a box size of 240 pixels and calibrated pixel size of 1.17 Å. Several rounds of 2D classification were run subsequently to clean the dataset. Around 12,000 particles were selected with the best signal-to-noise ratio to generate the ab initio model. Extracted particles from the best 2D class averages were used to calculate the 3D classification using the ab initio structure.

For *Mtb*Cbs in the presence of SAM + Ser, after three rounds of 2D classifications, 643,806 particles were selected for 3D classification. The 3D classification was performed with C2 symmetry, and the 643,806 particles dataset was divided into four classes. From the 3D classification result, class 4 (172,994 particles) was observed as a tetramer and well resolved. 3D autorefinement was carried out for class 4 using a soft mask in RELION 3.1. Followed by 3D auto-refinement, per-particle defocus refinement was performed with beam tilt correction, anisotropic magnification correction, and per micrograph astigmatism fitting. Corrected particles were subjected for Bayesian polishing. Polished particles were subjected for another round of 3D refinement. 3D autorefined map of *Mtb* Cbs in the presence of substrate was sharpened using RELION 3.1 (table S3). The structural differences after substrate treatment were observed

after superimposing both the cryo-EM density maps in UCSF Chimera and UCSF ChimeraX.

Fourier shell correlation calculation and local resolution estimation

All structures were visualized using UCSF Chimera and UCSF ChimeraX. Fourier shell correlation was estimated for all the maps at 0.143. Local resolution estimation was done for all the maps using unfiltered auto-refined maps with ResMap (72).

Homology modeling

Because of the unavailability of full-length *Mtb*Cbs structure, we performed homology modeling using SWISS-MODEL (73) to predict a probable model for *Mtb*Cbs. The homology model generated for catalytic core region and Bateman module separately. The homology model was fitted into the catalytic core region and Bateman module in cryo-EM map of *Mtb*Cbs. All the model fittings were performed into the respective cryo-EM density maps using UCSF Chimera and UCSF ChimeraX.

Atomic model building and validation

Initially, cryo-EM maps were docked with predicted homology model in catalytic core and Bateman module separately (generated in SWISS-MODEL). The docking was done using phenix:dock_in_map program in PHENIX (74). The docked model was refined using phenix:real_space_refine program in PHENIX. The refined model and cryo-EM maps were imported in Coot (75) and manually fitted and corrected. The model was subsequently rebuilt manually in the missing area of homology model using Coot. This process was done iteratively, and after each round fitting in Coot, the model was refined iteratively using phenix:real_space_refine program in PHENIX. The final models were analyzed using MolProbity in PHENIX. The models were validated using phenix:validation_tool in PHENIX.

Initially, the PLP was fitted manually at the active site for both the maps using Coot. Later, refinement was carried out for the model with PLP using phenix:real_space_refine program. The SAM density was not visible for SAM-treated *Mtb*Cbs cryo-EM model at an RMSD value of 6s. SAM was docked in the possible orientation of the protein at an RMSD value of 3s to understand SAM interaction (table S3).

Analysis of atomic models

Atomic models and cryo-EM maps were visualized and analyzed using UCSF Chimera, UCSF ChimeraX, and PyMOL (76). EMRinger score (77) for each map was calculated using PHENIX.

Identification of responsible amino acid residues for SAM interaction

hCBS Bateman module (PDB: 4PCU) and *Mtb*Cbs Bateman module were superimposed using PyMOL. The predicted amino acids responsible for SAM interaction in *Mtb*Cbs were determined and marked.

Identification of amino acid residues at the dimer and tetramer interface

Initially, the amino acid residues present at the dimer and tetramer interface was calculated using PDBSum (78). The distance between two amino acid residues were calculated in UCSF Chimera and confirmed the selected amino acids for site directed mutagenesis.

Determination of active site pocket for native *Mtb*Cbs and SAM-treated *Mtb*Cbs

The active site pocket for both the models was calculated using CASTp 3.0 software (79). The pocket was visualized in UCSF Chimera.

Pulse proteolysis assay

Pulse proteolysis was performed as described in with some modifications (39). Purified *Mtb*Cbs (0.5 mg/ml) was equilibrated overnight in a chilled water bath maintained at 4°C. The assay buffer comprised 20 mM tris-HCl (pH 8), urea (1 to 7 M), and 10 mM CaCl₂. Thermolysin from *Geobacillus stearothermophilus* (0.1 mg/ml) (Sigma-Aldrich, St. Louis, MO, USA) was used for digestion. *Mtb*Cbs was incubated with 500 mM SAM at 37°C for 15 min before urea equilibration to carry out pulse proteolysis in the presence of SAM. Proteolytic pulse was given for exactly 1 min and was subsequently quenched in 20 mM EDTA. Samples were resolved on 12% SDS–polyacrylamide gel electrophoresis (PAGE) gel and visualized by Colloidal Coomassie staining. Band intensities were quantified using ImageJ. C_m (midpoint of the urea-induced unfolding transition) was determined by plotting f_{fold} (band intensity of intact protein at a given concentration of urea divided by band intensity of intact protein in the absence of urea) and fitting it to a sigmoidal model. The global stability of the protein ($\Delta G^{\circ}_{\text{unf}}$) was calculated by multiplying the C_m by the m value (denaturant dependence of $\Delta G^{\circ}_{\text{unf}}$). The m value of *Mtb*Cbs was estimated as described by multiplying the number of amino acid residues by 0.013.

RT-qPCR analysis

One microgram of total cellular RNA was purified (80) and then treated with Turbo deoxyribonuclease (Invitrogen, Carlsbad, CA, USA). From this, 200 ng of RNA was used for cDNA synthesis using the iScript Select cDNA Synthesis Kit. A 1 iQ SYBR Green Supermix cocktail was used for the RT-qPCR reaction with gene specific primers in the CFX96 RT-PCR System (Bio-Rad, Hercules, CA, USA). For gene expression analysis, 16S ribosomal RNA was used as internal normalization control in all cases.

Cell lysis and Western blotting

Mtb cell lysis was performed by four rounds of bead beating (40 s) in FastPrep-24 Classic bead beating grinder (MP Biomedicals, Irvine CA, USA) using glass beads in a total volume of 1 ml of lysis buffer with intermittent chilling on ice. The lysis buffer comprised 50 mM tris-HCl, 150 mM NaCl, 5% glycerol, 0.5 mM b-mercaptoethanol, and 1 cOmplete EDTA-free protease inhibitor cocktail (Roche, Basel, Switzerland). For Western blotting, 50 mg of total cell lysate was resolved on a 12% SDS-PAGE gel and transferred to immuno-blot polyvinylidene difluoride membrane in a Mini Trans-blot Cell (Bio-Rad, Hercules, CA, USA) at a constant current of 350 mA. Cbs was detected using Cbs antisera (anti-rabbit; 1:10,000) and anti-rabbit immunoglobulin G horseradish-linked antibody (1:10,000; Cell Signaling Technology, Danvers, MA, USA). Rho (gift from V. Nagaraja, Department of Microbiology and Cell Biology, Indian Institute of Science) was used as internal control (anti-rabbit; 1:10,000). The blots were developed using Clarity Max ECL Western blotting sub-strate in a GelDoc XR+ Gel Documentation system. Densitometry was performed by plotting band intensities quantified using ImageJ (<https://imagej.nih.gov/ij/download.html>).

Metabolite extraction and analysis

Metabolite extraction for the targeted analysis of RTS pathway and AMC intermediates was carried out as outlined in (81). Briefly, exponentially growing *Mtb* cultures ($\text{OD}_{600} = 0.6$) were treated with AZA for the indicated time period or left untreated. The cells were quenched with four volumes of 60% methanol, maintained at 45°C for 5 min in a dry ice–methanol bath, and centrifuged at 5000 rpm

for 5 min. The pellet was resuspended in 750 ml of 60% methanol, maintained at 45°C, and centrifuged at 5000 rpm for 5 min. Subsequently, the pellet was resuspended in 1 ml of 75% ethanol, incubated at 80°C for 3 min exactly, and kept on ice immediately for 5 min, followed by centrifugation at 13,000 rpm for 15 min. The final supernatant was lyophilized and stored at 80°C till further analysis.

Survival assays

Exponentially growing cultures were diluted in 7H9-ADS to an OD_{600} of 0.1 and treated with the indicated concentrations of drugs for 24 hours at 37°C with constant shaking. Cells were plated on 7H11-ADS plates and incubated at 37°C for 3 weeks. Susceptibility was expressed as percentage survival of the strains in comparison to untreated controls.

Animal experimentation

WT and heterozygous HIV-Tg mice Tg26 (C57BL/6 background) containing HIV proviral DNA with mutated 3-kb region of *gag* and *pol* genes were used. HIV-Tg26 was backcrossed with C57BL/6 for eight generations to create a more stable HIV-Tg26 (FVB/N) line by R. L. Sutcliffe (Veterans Affairs Medical Center, Emory University, Atlanta, GA). The breeding colony was maintained in the BSL3 Animal Facility at CIDR, IISc, according to the Institutional Animal Ethical Committee (IBSC No. IBSC/IISc/AS/25/2019) guidelines. Genotyping was performed at 4 weeks of age by tail vein PCR. Six- to eight-week-old transgenic mice were used for the experiment. WT littermates were used as controls.

For the chronic model of infection, mice aged 6 to 8 weeks were infected by the aerosol route with 100 bacilli using a Madison chamber aerosol generation chamber and housed for 4 weeks for infection progression. At the indicated time points, mice were euthanized, and the lungs and spleen were harvested for analysis of bacterial burden and histopathology. Lung and spleen samples were homogenized in sterile 2 ml of phosphate-buffered saline (PBS), serially diluted, and plated on 7H11-OADC plates containing BBL MGIT PANTA anti-biotic cocktail (Becton, Dickinson and Company, Franklin Lakes, NJ, USA) for colony-forming unit (CFU) enumeration.

Homocysteine quantification

Homocysteine was quantified in cell lines and animal lungs using the Euro Diagnostics homocysteine assay kit (Chennai, India) according to the manufacturer's protocol.

Ethics statement

This study was carried out in strict accordance with the guidelines provided by the Committee for the Purpose of Control and Supervision on Experiments on Animals (CPCSEA), Government of India. The protocol of animal experiment was approved by animal ethical committee on the Ethics of Animal Experiments, IISc, Bangalore, India (approval number: CAF/Ethics/544/2017). All humane efforts were made to minimize the suffering.

Detection of ROS production by *Mtb*

ROS generation was detected using the fluorescent dye CellROX Deep Red reagent (Invitrogen, Carlsbad, CA, USA). Briefly, CellROX Deep Red was added to 500 ml of treated or untreated samples at a final concentration of 2.5 mM and incubated at 37°C with constant shaking. Subsequently, cells were pelleted and washed twice with 1 PBS and resuspended in 150 ml of PBS, and in all cases 10,000 events were

analyzed with flow cytometry with $\lambda_{\text{Ex}} = 644 \text{ nm}$ and $\lambda_{\text{Em}} = 665 \text{ nm}$ in BD FACSaria flow cytometer (BD Biosciences, San Jose, CA, USA). Fold change in median fluorescence intensities with respect to un-treated controls were plotted.

Statistical analysis

All statistical analyses were performed using GraphPad Prism version 8.0 (GraphPad Software, San Diego, CA, USA). All data indicated are means \pm SD. Data were first tested for normality by Shapiro-Wilk's test, followed with requisite parametric statistical test.

Data fitting

All custom data fittings were obtained by nonlinear regression using OriginPro 2021 (OriginLab, Northampton, MA, USA).

SUPPLEMENTARY MATERIALS

Supplementary material for this article is available at

<https://science.org/doi/10.1126/sciadv.abo0097>

[View/request a protocol for this paper from Bio-protocol.](#)

REFERENCES AND NOTES

- K. H. zu Bentrup, D. G. Russell, Mycobacterial persistence: Adaptation to a changing environment. *Trends Microbiol.* **9**, 597–605 (2001).
- M. Gengenbacher, S. H. E. Kaufmann, *Mycobacterium tuberculosis*: Success through dormancy. *FEMS Microbiol. Rev.* **36**, 514–532 (2012).
- D. F. Warner, *Mycobacterium tuberculosis* metabolism. *Cold Spring Harb. Perspect. Med.* **5**, a021121 (2014).
- S. Ehrt, D. Schnappinger, K. Y. Rhee, Metabolic principles of persistence and pathogenicity in *Mycobacterium tuberculosis*. *Nat. Rev. Microbiol.* **16**, 496–507 (2018).
- S. T. Cole, R. Brosch, J. Parkhill, T. Garnier, C. Churcher, D. Harris, S. V. Gordon, K. Eiglmeier, S. Gas, C. E. Barry III, F. Tekaia, K. Badcock, D. Basham, D. Brown, T. Chillingworth, R. Connor, R. Davies, K. Devlin, T. Feltwell, S. Gentles, N. Hamlin, S. Holroyd, T. Hornsby, K. Jagels, A. Krogh, J. McLean, S. Moule, L. Murphy, K. Oliver, J. Osborne, M. A. Quail, M. A. Rajandream, J. Rogers, S. Rutter, K. Seeger, J. Skelton, R. Squares, J. E. Sulston, K. Taylor, S. Whitehead, B. G. Barrell, Deciphering the biology of *Mycobacterium tuberculosis* from the complete genome sequence. *Nature* **393**, 537–544 (1998).
- S. Tiwari, A. J. van Tonder, C. Vilchèze, V. Mendes, S. E. Thomas, A. Malek, B. Chen, M. Chen, J. Kim, T. L. Blundell, J. Parkhill, B. Weinrick, M. Berney, W. R. Jacobs, Arginine-deprivation-induced oxidative damage sterilizes *Mycobacterium tuberculosis*. *Proc. Natl. Acad. Sci. U.S.A.* **115**, 9779–9784 (2018).
- M. Berney, L. Berney-Meyer, K. W. Wong, B. Chen, M. Chen, J. Kim, J. Wang, D. Harris, J. Parkhill, J. Chan, F. Wang, W. R. Jacobs, Essential roles of methionine and S-adenosylmethionine in the autarkic lifestyle of *Mycobacterium tuberculosis*. *Proc. Natl. Acad. Sci. U.S.A.* **112**, 10008–10013 (2015).
- E. J. Hasenoehl, D. Rae Sajord, L. Berney-Meyer, S. Johnson, J. A. M. Tufariello, T. Fuhrer, G. M. Cook, W. R. Jacobs, M. Berney, Derailing the aspartate pathway of *Mycobacterium tuberculosis* to eradicate persistent infection. *Nat. Commun.* **10**, 4215 (2019).
- M. S. Pavelka, B. Chen, C. L. Kelley, F. M. Collins, W. R. Jacobs, Vaccine efficacy of a lysine auxotroph of *Mycobacterium tuberculosis*. *Infect. Immun.* **71**, 4190–4192 (2003).
- M. H. Larsen, K. Biermann, B. Chen, T. Hsu, V. K. Sambandamurthy, A. A. Lackner, P. P. Aye, P. Didier, D. Huang, L. Shao, H. Wei, N. L. Letvin, R. Frothingham, B. F. Haynes, Z. W. Chen, W. R. Jacobs, Efficacy and safety of live attenuated persistent and rapidly cleared *Mycobacterium tuberculosis* vaccine candidates in non-human primates. *Vaccine* **27**, 4709–4717 (2009).
- S. L. Sampson, K. G. Mansfield, A. Carville, D. M. Magee, T. Quitugua, E. W. Howerth, B. R. Bloom, M. K. Hondalus, Extended safety and efficacy studies of a live attenuated double leucine and pantothenate auxotroph of *Mycobacterium tuberculosis* as a vaccine candidate. *Vaccine* **29**, 4839–4847 (2011).
- N. A. Buchmeier, G. L. Newton, T. Koledin, R. C. Fahey, Association of mycothiol with protection of *Mycobacterium tuberculosis* from toxic oxidants and antibiotics. *Mol. Microbiol.* **47**, 1723–1732 (2003).
- G. Huet, M. Daffé, I. Saves, Identification of the *Mycobacterium tuberculosis* *SUF* machinery as the exclusive mycobacterial system of [Fe-S] cluster assembly: Evidence for its implication in the pathogen's survival. *J. Bacteriol.* **187**, 6137–6146 (2005).
- J. Rybníček, F. Pojer, J. Marienhagen, G. S. Kolly, J. M. Chen, E. van Gumpel, P. Hartmann, S. T. Cole, The cysteine desulfurase *IscS* of *Mycobacterium tuberculosis* is involved in iron-sulfur cluster biogenesis and oxidative stress defence. *Biochem. J.* **459**, 467–478 (2014).
- J. C. Seeliger, C. M. Holsclaw, M. W. Schelle, Z. Botyanszki, S. A. Gilmore, S. E. Tully, M. Niederweis, B. F. Cravatt, J. A. Leary, C. R. Bertozzi, Elucidation and chemical modulation of sulfolipid-1 biosynthesis in *Mycobacterium tuberculosis*. *J. Biol. Chem.* **287**, 7990–8000 (2012).
- V. K. Pal, P. Bandyopadhyay, A. Singh, Hydrogen sulfide in physiology and pathogenesis of bacteria and viruses. *IUBMB Life* **70**, 393–410 (2018).
- M. I. Voskuil, K. C. Visconti, G. K. Schoolnik, *Mycobacterium tuberculosis* gene expression during adaptation to stationary phase and low-oxygen dormancy. *Tuberculosis (Edinb.)* **84**, 218–227 (2004).
- D. Schnappinger, S. Ehrt, M. I. Voskuil, Y. Liu, J. A. Mangan, I. M. Monahan, G. Dolganov, B. Efron, P. D. Butcher, C. Nathan, G. K. Schoolnik, Transcriptional adaptation of *Mycobacterium tuberculosis* within macrophages: Insights into the phagosomal environment. *J. Exp. Med.* **198**, 693–704 (2003).
- R. Pinto, Q. X. Tang, W. J. Britton, T. S. Leyh, J. A. Triccas, The *Mycobacterium tuberculosis* *cysD* and *cysNC* genes form a stress-induced operon that encodes a tri-functional sulfate-activating complex. *Microbiology (Reading)*. **150**, 1681–1686 (2004).
- R. Mishra, S. Kohli, N. Malhotra, P. Bandyopadhyay, M. Mehta, M. H. Munshi, V. Adiga, V. K. Ahuja, R. K. Shandil, R. S. Rajmani, A. S. N. Seshasayee, A. Singh, Targeting redox heterogeneity to counteract drug tolerance in replicating *Mycobacterium tuberculosis*. *Sci. Transl. Med.* **11**, eaaw6635 (2019).
- W. Salaemae, G. W. Booker, S. W. Polyak, The role of biotin in bacterial physiology and virulence: A novel antibiotic target for *Mycobacterium tuberculosis*. *Microbiol. Spectr.* **4**, 10.1128/MICROBIOLSPEC.VMBF-0008-2015 (2016).
- R. K. Dhiman, S. Mahapatra, R. A. Slayden, M. E. Boyne, A. Lenaerts, J. C. Hinshaw, S. K. Angala, D. Chatterjee, K. Biswas, P. Narayanasamy, M. Kurosu, D. C. Crick, Menquinone synthesis is critical for maintaining mycobacterial viability during exponential growth and recovery from non-replicating persistence. *Mol. Microbiol.* **72**, 85–97 (2009).
- D. Barkan, D. Hedhli, H. G. Yan, K. Huygen, M. S. Glickman, *Mycobacterium tuberculosis* lacking all mycolic acid cyclopropanation is viable but highly attenuated and hyperinflammatory in mice. *Infect. Immun.* **80**, 1958–1968 (2012).
- J. D. Finkelstein, J. J. Martin, Methionine metabolism in mammals. Distribution of homocysteine between competing pathways. *J. Biol. Chem.* **259**, 9508–9513 (1984).
- O. Kabil, R. Banerjee, Enzymology of H₂S biogenesis, decay and signaling. *Antioxid. Redox Signal.* **20**, 770–782 (2014).
- J. D. Finkelstein, Pathways and regulation of homocysteine metabolism in mammals. *Semin. Thromb. Hemost.* **26**, 219–226 (2000).
- A. Prudova, Z. Bauman, A. Braun, V. Vitvitsky, S. C. Lu, R. Banerjee, S-Adenosylmethionine stabilizes cystathionine b-synthase and modulates redox capacity. *Proc. Natl. Acad. Sci. U.S.A.* **103**, 6489–6494 (2006).
- B. L. Predmore, D. J. Lefer, G. Gojon, Hydrogen sulfide in biochemistry and medicine. *Antioxid. Redox Signal.* **17**, 119–140 (2012).
- M. W. Schelle, C. R. Bertozzi, Sulfate metabolism in mycobacteria. *ChemBiochem* **7**, 1516–1524 (2006).
- P. Fontán, V. Aris, S. Ghanny, P. Soteropoulos, I. Smith, Global transcriptional profile of *Mycobacterium tuberculosis* during THP-1 human macrophage infection. *Infect. Immun.* **76**, 717–725 (2008).
- S. Devi, K. F. Tarique, M. F. Ali, S. A. Abdul Rehman, S. Gourinath, Identification and characterization of *Helicobacter pylori* O-acetylserine-dependent cystathionine b-synthase, a distinct member of the PLP-II family. *Mol. Microbiol.* **112**, 718–739 (2019).
- S. Singh, D. Padovani, R. A. Leslie, T. Chiku, R. Banerjee, Relative contributions of cystathionine b-synthase and g-cystathionase to H₂S biogenesis via alternative trans-sulfuration reactions. *J. Biol. Chem.* **284**, 22457–22466 (2009).
- S. Devi, S. A. Abdul Rehman, K. F. Tarique, S. Gourinath, Structural characterization and functional analysis of cystathionine b-synthase: An enzyme involved in the reverse transsulfuration pathway of *Bacillus anthracis*. *FEBS J.* **284**, 3862–3880 (2017).
- S. Taoka, L. Widjaja, R. Banerjee, Assignment of enzymatic functions to specific regions of the PLP-dependent heme protein cystathionine b-synthase. *Biochemistry* **38**, 13155–13161 (1999).
- J. Ereño-Orbea, T. Majtan, I. Oyenarte, J. P. Kraus, L. A. Martínez-Cruza, Structural basis of regulation and oligomerization of human cystathionine b-synthase, the central enzyme of transsulfuration. *Proc. Natl. Acad. Sci. U.S.A.* **110**, E3790–E3799 (2013).
- J. Ereño-Orbea, T. Majtan, I. Oyenarte, J. P. Kraus, L. A. Martínez-Cruz, Structural insight into the molecular mechanism of allosteric activation of human cystathionine b-synthase by S-adenosylmethionine. *Proc. Natl. Acad. Sci. U.S.A.* **111**, E3845–E3852 (2014).
- M. Koutmos, O. Kabil, J. L. Smith, R. Banerjee, Structural basis for substrate activation and regulation by cystathionine b-synthase (CBS) domains in cystathionine (b)-synthase. *Proc. Natl. Acad. Sci. U.S.A.* **107**, 20958–20963 (2010).

38. Y. Tu, C. A. Kreinbring, M. Hill, C. Liu, G. A. Petsko, C. D. McCune, D. B. Berkowitz, D. Liu, D. Ringe, Crystal structures of cystathionine b-synthase from *Saccharomyces cerevisiae*: One enzymatic step at a time. *Biochemistry* **57**, 3134–3145 (2018).
39. C. Park, S. Marqusee, Quantitative determination of protein stability and ligand binding by pulse proteolysis. *Curr. Protoc. Protein Sci.* 10.1002/0471140864.PS2011S46 (2006).
40. B. J. Berger, M. H. Knodel, Characterisation of methionine adenosyltransferase from *Mycobacterium smegmatis* and *M. tuberculosis*. *BMC Microbiol.* **3**, 1–13 (2003).
41. R. A. Festa, F. McAllister, M. J. Pearce, J. Mintseris, K. E. Burns, S. P. Gygi, K. H. Darwin, Prokaryotic ubiquitin-like protein (Pup) proteome of *Mycobacterium tuberculosis* [corrected]. *PLOS ONE* **5**, e8589 (2010).
42. M. P. Ferla, W. M. Patrick, Bacterial methionine biosynthesis. *Microbiology (Reading)* **160**, 1571–1584 (2014).
43. P. R. Wheeler, N. G. Coldham, L. Keating, S. V. Gordon, E. E. Wooff, T. Parish, R. G. Hewinson, Functional demonstration of reverse transsulfuration in the *Mycobacterium tuberculosis* complex reveals that methionine is the preferred sulfur source for pathogenic mycobacteria. *J. Biol. Chem.* **280**, 8069–8078 (2005).
44. S. Chakraborty, T. Gruber, C. E. Barry, H. I. Boshoff, K. Y. Rhee, Para-aminosalicylic acid acts as an alternative substrate of folate metabolism in *Mycobacterium tuberculosis*. *Science* **339**, 88–91 (2013).
45. J. Perla-Kaján, T. Twardowski, H. Jakubowski, Mechanisms of homocysteine toxicity in humans. *Amino Acids* **32**, 561–572 (2007).
46. R. Deminice, T. C. V. Silva, V. H. F. de Oliveira, Elevated homocysteine levels in human immunodeficiency virus-infected patients under antiretroviral therapy: A meta-analysis. *World J. Virol.* **4**, 147–155 (2015).
47. E. Cassol, M. Alfano, P. Biswas, G. Poli, Monocyte-derived macrophages and myeloid cell lines as targets of HIV-1 replication and persistence. *J. Leukoc. Biol.* **80**, 1018–1030 (2006).
48. B. A. Jacob, K. M. Porter, S. C. Elms, P. Y. Cheng, D. P. Jones, R. L. Sutliff, HIV-1-induced pulmonary oxidative and nitrosative stress: Exacerbated response to endotoxin administration in HIV-1 transgenic mouse model. *Am. J. Physiol. Lung Cell. Mol. Physiol.* **291**, L811–L8119 (2006).
49. S. Taoka, S. Ohja, X. Shan, W. D. Kruger, R. Banerjee, Evidence for heme-mediated redox regulation of human cystathionine b-synthase activity. *J. Biol. Chem.* **273**, 25179–25184 (1998).
50. S. Ehrh, D. Schnappinger, Mycobacterial survival strategies in the phagosome: Defence against host stresses. *Cell. Microbiol.* **11**, 1170–1178 (2009).
51. S. A. Consaul, L. F. Wright, S. Mahapatra, D. C. Crick, M. S. Pavelka, An unusual mutation results in the replacement of diaminopimelate with lanthionine in the peptidoglycan of a mutant strain of *Mycobacterium smegmatis*. *J. Bacteriol.* **187**, 1612–1620 (2005).
52. P. Giménez-Mascarell, T. Majtan, I. Oyenarte, J. Ereño-Orbea, J. Majtan, J. Klaudivy, J. P. Kraus, L. A. Martínez-Cruz, Crystal structure of cystathionine b-synthase from honeybee *Apis mellifera*. *J. Struct. Biol.* **202**, 82–93 (2018).
53. M. B. Guzzo, Q. Li, H. V. Nguyen, W. H. Boom, L. Nguyen, The pup-proteasome system protects mycobacteria from antimicrobial antifolates. *Antimicrob. Agents Chemother.* **65**, e01967-20 (2021).
54. Z. Weinberg, E. E. Regulski, M. C. Hammond, J. E. Barrick, Z. Yao, W. L. Ruzzo, R. R. Breaker, The aptamer core of SAM-IV riboswitches mimics the ligand-binding site of SAM-I riboswitches. *RNA* **14**, 822–828 (2008).
55. V. Gopinath, S. Raghunandan, R. L. Gomez, A. Surendran, R. Ramachandran, A. R. Pushparajan, S. Mundayoor, A. Jaleel, R. A. Kumar, Profiling the proteome of *Mycobacterium tuberculosis* during dormancy and reactivation. *Mol. Cell. Proteomics* **14**, 2160–2176 (2015).
56. M. A. Caudill, J. C. Wang, S. Melnyk, I. P. Pogribny, S. Jernigan, M. D. Collins, J. Santos-Guzman, M. E. Swendseid, E. A. Cogger, S. J. James, Intracellular S-adenosylhomocysteine concentrations predict global dna hypomethylation in tissues of methyl-deficient cystathionine b-synthase heterozygous mice. *J. Nutr.* **131**, 2811–2818 (2001).
57. K. H. Jhee, W. D. Kruger, The role of cystathionine b-synthase in homocysteine metabolism. *Antioxid. Redox Signal.* **7**, 813–822 (2005).
58. R. Virmani, Y. Hasija, Y. Singh, Effect of homocysteine on biofilm formation by mycobacteria. *Indian J. Microbiol.* **58**, 287–293 (2018).
59. J. M. Lensmire, J. P. Dodson, B. Y. Hsueh, M. R. Wischer, P. C. Deleka, J. C. Shook, E. N. Ottosen, P. J. Kies, J. Ravi, N. D. Hammer, The *Staphylococcus aureus* cystine transporters TcyABC and TcyP facilitate nutrient sulfur acquisition during infection. *Infect. Immun.* **88**, e00690-19 (2020).
60. S. Kashiwamata, D. M. Greenberg, Studies on cystathionine synthase of rat liver properties of the highly purified enzyme. *Properties of the highly purified enzyme. Biochim. Biophys. Acta.* **212**, 488–500 (1970).
61. I. Barr, F. Guo, Pyridine hemochromagen assay for determining the concentration of heme in purified protein solutions. *Bio Protoc.* **5**, e1594 (2015).
62. G. Tang, L. Peng, P. R. Baldwin, D. S. Mann, W. Jiang, I. Rees, S. J. Ludtke, EMAN2: An extensible image processing suite for electron microscopy. *J. Struct. Biol.* **157**, 38–46 (2007).
63. C. F. Reboul, M. Eager, D. Elmlund, H. Elmlund, Single-particle cryo-EM-Improved ab initio 3D reconstruction with SIMPLE/PRIME. *Protein Sci.* **27**, 51–61 (2018).
64. I. Pramanick, N. Sengupta, S. Mishra, S. Pandey, N. Girish, A. Das, S. Dutta, Conformational flexibility and structural variability of SARS-CoV2 S protein. *Structure* **29**, 1–12 (2021).
65. S. H. W. Scheres, RELION: Implementation of a Bayesian approach to cryo-EM structure determination. *J. Struct. Biol.* **180**, 519–530 (2012).
66. X. Li, P. Mooney, S. Zheng, C. R. Booth, M. B. Braumfeld, S. Gubbens, D. A. Agard, Y. Cheng, Electron counting and beam-induced motion correction enable near-atomic-resolution single-particle cryo-EM. *Nat. Methods* **10**, 584–590 (2013).
67. T. Grant, A. Rohou, N. Grigorieff, cisTEM, user-friendly software for single-particle image processing. *eLife* **7**, e35383 (2018).
68. A. Rohou, N. Grigorieff, CTFIND4: Fast and accurate defocus estimation from electron micrographs. *J. Struct. Biol.* **192**, 216–221 (2015).
69. E. F. Pettersen, T. D. Goddard, C. C. Huang, G. S. Couch, D. M. Greenblatt, E. C. Meng, T. E. Ferrin, UCSF Chimera - A visualization system for exploratory research and analysis. *J. Comput. Chem.* **25**, 1605–1612 (2004).
70. E. F. Pettersen, T. D. Goddard, C. C. Huang, E. C. Meng, G. S. Couch, T. I. Croll, J. H. Morris, T. E. Ferrin, UCSF ChimeraX: Structure visualization for researchers, educators, and developers. *Protein Sci.* **30**, 70–82 (2021).
71. T. D. Goddard, C. C. Huang, E. C. Meng, E. F. Pettersen, G. S. Couch, J. H. Morris, T. E. Ferrin, UCSF ChimeraX: Meeting modern challenges in visualization and analysis. *Protein Sci.* **27**, 14–25 (2018).
72. A. Kucukelbir, F. J. Sigworth, H. D. Tagare, Quantifying the local resolution of cryo-EM density maps. *Nat. Methods* **11**, 63–65 (2014).
73. A. Waterhouse, M. Bertoni, S. Bienert, G. Studer, G. Tauriello, R. Gumienny, F. T. Heer, T. A. P. de Beer, C. Rempfer, L. Bordoli, R. Lepore, T. Schwede, SWISS-MODEL: Homology modelling of protein structures and complexes. *Nucleic Acids Res.* **46**, W296–W303 (2018).
74. P. D. Adams, P. V. Afonine, G. Bunkóczi, V. B. Chen, I. W. Davis, N. Echols, J. J. Headd, L. W. Hung, G. J. Kapral, R. W. Grosse-Kunstleve, A. J. McCoy, N. W. Moriarty, R. Oeffner, R. J. Read, D. C. Richardson, J. S. Richardson, T. C. Terwilliger, P. H. Zwart, PHENIX: A comprehensive Python-based system for macromolecular structure solution. *Acta Crystallogr. D Biol. Crystallogr.* **66**, 213–221 (2010).
75. P. Emsley, B. Lohkamp, W. G. Scott, K. Cowtan, Features and development of Coot. *Acta Crystallogr. D Biol. Crystallogr.* **66**, 486–501 (2010).
76. Schrödinger LLC, The PyMOL Molecular Graphics System, Version 2.4.0. Schrödinger LLC, 2021. (<https://pymol.org/2/>).
77. B. A. Barad, N. Echols, R. Y. R. Wang, Y. Cheng, F. Dimaio, P. D. Adams, J. S. Fraser, EMRinger: Side chain-directed model and map validation for 3D cryo-electron microscopy. *Nat. Methods* **12**, 943–946 (2015).
78. R. A. Laskowski, PDBsum new things. *Nucleic Acids Res.* **37**, D355–D359 (2009).
79. W. Tian, C. Chen, X. Lei, J. Zhao, J. Liang, CASTp 3.0: Computed atlas of surface topography of proteins. *Nucleic Acids Res.* **46**, W363–W367 (2018).
80. M. Chawla, P. Parikh, A. Saxena, M. Munshi, M. Mehta, D. Mai, A. K. Srivastava, K. V. Narasimulu, K. E. Redding, N. Vashi, D. Kumar, A. J. C. Steyn, A. Singh, *Mycobacterium tuberculosis* WhiB4 regulates oxidative stress response to modulate survival and dissemination in vivo. *Mol. Microbiol.* **85**, 1148–1165 (2012).
81. A. Walvekar, Z. Rashida, H. Maddali, S. Laxman, A versatile LC-MS/MS approach for comprehensive, quantitative analysis of central metabolic pathways. *Wellcome Open Res.* **3**, 122 (2018).

Acknowledgments: We thank Dr. K. R. Vinothkumar and the National Cryo-EM Facility, NCBS Bangalore for the cryo-EM data collection of MtbCbs and MtbCbs+SAM. We also thank Mr. A. Kumar and the Advanced Centre for cryo-EM microscopy facility at IISc Bangalore for the cryo-EM data collection of SAM + serine-treated MtbCbs. **Funding:** This work was supported by the following: Wellcome Trust/DBT India Alliance Grants, IA/S/16/2/502700 (to A.S.) and in part by the Department of Biotechnology (DBT) grants (BT/PR13522/COE/34/27/2015, BT/ PR29098/Med/29/1324/2018, BT/HRD/NBA/39/07/2018-19, and BT/PR39308/ DRUG/134/86/2021), DBT-IISc Partnership Program (22-0905-0006-05-987-436), and DST-FIST grants (to A.S.). We acknowledge the financial support from the Ministry of Human Resource Development (MHRD) (grant number STARS-1/171), Science and Engineering Research Board (SERB) (grant number SB/S2/RJN-145/2015 and SERB-EMR/2016/000608), DBT (grant number BT/PR25580/BRB/10/1619/2017) (to S.D.). P.B. acknowledges the Council for Scientific and Industrial Research, Ministry of Human Resource Development, Government of India for financial support. I.P. was supported by the GATE Ph.D. fellowship. R.B. thanks DBT/Wellcome Trust India Alliance IA/E/19/1/504978 for manpower support. We acknowledge DBT-BUILDER Program (BT/INF/22/SP22844/2017) and DST-FIST (SR/FST/LSII-039/2015) for the Advanced Centre for Cryo-EM facility at IISc, Bangalore. The National Cryo-EM facility at NCBS Bangalore is supported by the Department of Biotechnology, Government of India grant DBT/PR12422/MED/31/287/2014. We thank DBT-IISc partnership program for the TEM facility at Biological Sciences Division, IISc Bangalore. We acknowledge the Central Mass Spectrometry Facility at

Biological Sciences Division, IISc Bangalore. **Author contributions:** Conceptualization: A.S., S.D., P.B., and I.P. Methodology: A.S., S.D., S.L., P.B., I.P., S.P., S.Sr., and S.Si. Investigation: A.S., S.D., S.L., P.B., I.P., R.B., S.P., S.Sr., S.Si., and R.S.R. Visualization: A.S., S.D., P.B., and I.P. Funding acquisition: A.S. and S.D. Project administration: A.S. and S.D. Supervision: A.S., S.D. and S.L. Writing—original draft: A.S., S.D., P.B., and I.P. Writing—review and editing: A.S., S.D., S.L., P.B., and I.P. **Competing interests:** The authors declare that they have no competing interests. **Data and materials availability:** Cryo-EM electron density maps of *Mtb*Cbs, SAM-treated *Mtb*Cbs, and SAM + serine-treated *Mtb*Cbs have been deposited in the Electron Microscopy Databank and PDB. Native *Mtb*Cbs: EMD-33331, PDB 7XNZ; SAM-treated *Mtb*Cbs: EMD-33348, PDB 7XOH; SAM + serine-treated *Mtb*Cbs: EMD-33363, PDB 7XOY. All data needed to evaluate the conclusions in the paper are present in the paper and/or the Supplementary Materials. Submitted 6 January 2022 Accepted 9 May 2022 Published 24 June 2022 10.1126/sciadv.abo0097

S-Adenosylmethionine–responsive cystathionine β -synthase modulates sulfur metabolism and redox balance in *Mycobacterium tuberculosis*

Parijat BandyopadhyayIshika PramanickRupam BiswasSabarinath PSSreesa SreedharanShalini SinghRaju S. RajmaniSunil LaxmanSomnath DuttaAmit Singh

Sci. Adv., 8 (25), eabo0097. • DOI: 10.1126/sciadv.abo0097

View the article online

<https://www.science.org/doi/10.1126/sciadv.abo0097>

Permissions

<https://www.science.org/help/reprints-and-permissions>

Use of this article is subject to the [Terms of service](#)

Science Advances (ISSN) is published by the American Association for the Advancement of Science. 1200 New York Avenue NW, Washington, DC 20005. The title *Science Advances* is a registered trademark of AAAS.

Copyright © 2022 The Authors, some rights reserved; exclusive licensee American Association for the Advancement of Science. No claim to original U.S. Government Works. Distributed under a Creative Commons Attribution License 4.0 (CC BY).